

Microscopic Calculations in Diffractive Deep Inelastic Scattering

Andrey V. Pronyaev

Dissertation submitted to the Faculty of the
Virginia Polytechnic Institute and State University
in partial fulfillment of the requirements for the degree of

Doctor of Philosophy

in

Physics

Tetsuro Mizutani, Chair

Lay Nam Chang

John Ficenec

Mark Pitt

Tatsu Takeuchi

April 14, 1999

Blacksburg, Virginia

Keywords: Physics, Phenomenology, Deep Inelastic Scattering, QCD

Copyright 1999, Andrey V. Pronyaev

Diffractive Deep Inelastic Scattering

Andrey V. Pronyaev

(ABSTRACT)

New fundamental observables are becoming accessible with the Leading Proton Spectrometers (LPS) of ZEUS and H1. This enables us to test more thoroughly the pQCD mechanism of diffractive Deep Inelastic Scattering (DIS). Calculations of the diffractive cross-section in the small Bjorken x limit have been performed. We have used the microscopic QCD formalism of diffractive DIS to find higher twist corrections to the transverse structure functions and predict the diffractive slope and azimuthal asymmetries. We establish duality correspondence between diffraction into low-mass continuum and vector meson production, and calculate the diffractive contribution to the spin structure functions.

This work received partial support from the US DOE grant DE-FG02-96ER40994.

Acknowledgments

I am very grateful to my scientific advisor Professor Tetsuro Mizutani for his guidance and kind support during my stay at Virginia Tech. I would like to acknowledge inspiring and fruitful collaboration with Dr. Nikolai N. Nikolaev and Dr. Bronislav G. Zakharov from whom I learned a lot and who helped me at different stages of my physics studies. I greatly appreciate all the help from graduate students' secretary Chris Thomas, members of my graduate committee and the rest of the faculty and staff in the Physics Department. I would like to express my profound gratitude towards my dear wife Olga and my family for their encouragement and interest in my thesis.

Contents

Abstract	ii
Acknowledgments	iii
List of Figures	vii
1 Introduction	1
2 Light-cone perturbation theory	12
2.1 Kinematics	13
2.2 Leptonic part	17
2.3 Hadronic part	20
2.4 Diffractive excitation of continuum	29

3	Cross-sections	36
3.1	Angular dependence	37
3.2	Helicity components	40
3.3	Higher twist in transverse cross-section	45
3.4	Hard scale	47
3.5	Sum rule	48
3.6	Low-mass excitation	50
3.7	Vector meson production in DDIS	53
3.8	Duality	56
3.9	Impact parameter representation	59
4	Numerical calculations	63
4.1	Structure functions	64
4.2	Azimuthal asymmetries and ratios	84
4.3	Diffractive slope	94
4.4	Gluon structure function interpolation	103

5	Nucleon wave function	108
5.1	Nucleon spin flip and conserve	109
5.2	Spin structure function of proton	118
6	Summary and outlook	123
A	Light-cone momenta and spinors	125
	Bibliography	126
	Vita	131
	Journal publications	132

List of Figures

Fig.(1)-1 a) DIS of electrons on protons $ep \rightarrow e'X$; **b)** Diffractive DDIS $ep \rightarrow e'p'X$ **10**

Fig.(1)-2 a) Elastic scattering of hadrons h_a and h_b with Pomeron exchange in t -channel; **b)** Diffraction of h_a on h_b ; **c)** Pomeron as double gluon ladder in QCD..... **11**

Fig.(2.1)-1 a) Virtual photon - proton collision frame for diffractive DIS; **b)** Azimuthal angles in the transverse plane; **c)** Interaction regions in $\gamma^*p \rightarrow p'X$ process and (anti)quark momenta. **16**

Fig.(2.3)-1 a) Sample Feynman diagram for forward Compton amplitude $\gamma_{\lambda}^*p \rightarrow \gamma_{\lambda'}^*p$ and helicities of particles; **b)** Sample Feynman diagram for amplitude $\gamma_{\lambda}^*p \rightarrow V_{\lambda'}^*p'$ and helicities of particles. **27**

Fig.(2.3)-2 Four Feynman diagrams with gluons attached to different quarks in $q\bar{q}$ pair excitation and transverse momenta of particles..... **28**

Fig.(4.1)-1÷12 Results of numerical calculations for structure functions $F_i^{D(4)}(\Delta = 0)$ and $F_i^{D(3)}$, $i = T, TT', L, LT$, shown as functions of β and Q^2 for $x_{\mathbf{P}} = 0.001$ **68**

Fig.(4.1)-13÷14 Comparison of twist-2, $F_T^{D(3)}$, and twist-4, $F_L^{D(3)}$ and $F_{\hat{T}}^{D(3)}$ structure functions, shown as functions of β and Q^2 for $x_{\mathbf{P}} = 0.001$	80
Fig.(4.1)-15 The Q^2 dependence of total diffractive structure function $F_2^{D(3)}$ and its decomposition to transverse (T) and longitudinal (L), twist-2 (T2) and twist-4 (T4) components from [8]. Dotted curves correspond to excitation of light flavors u,d and s. Solid circles - H1 experimental data [27] on $F_2^{D(3)}$ for a) $\beta = 0.65$ and b) $\beta = 0.9$	82
Fig.(4.1)-16 Predictions from [8] for the $x_{\mathbf{P}}$ dependence of diffractive structure functions $F_2^{D(3)}$ for $\beta = 0.65$, the top two rows, and $\beta = 0.95$, the bottom two rows, in comparison with H1 experimental data [27] for several values of Q^2	83
Fig.(4.2)-1 Predictions for ratios of longitudinal and transverse structure functions $R_{L/T}^{D(4)}(\Delta = 0)$ and $R_{L/T}^{D(3)}$ as functions of β for $x_{\mathbf{P}} = 0.001$ and $Q^2 = 100 GeV^2$	88
Fig.(4.2)-2÷3 Azimuthal asymmetries $A_{LT}^{D(3)}$ and $A_{TT'}^{D(3)}$ as functions of β for $x_{\mathbf{P}} = 0.001$ and $Q^2 = 100 GeV^2$	89
Fig.(4.2)-4 Analytical (anl) and numerical (num) predictions for the ratio $R_{LT/T}^{D(4)}$ of LT interference and transverse structure functions, as functions of β for $x_{\mathbf{P}} = 0.001$ and $Q^2 = 100 GeV^2$	91
Fig.(4.2)-5 Ratio $\rho_{L/T}^{D(4)}$ of direct numerical calculation of $R_{L/T}^{D(4)}(num)$ from L and T structure functions, and $R_{L/T}^{D(4)}(anl)$ from analytical evaluation, as functions of β for $x_{\mathbf{P}} = 0.001$ and $Q^2 = 100 GeV^2$	92
Fig.(4.2)-6 Analytical (anl) and numerical (num) predictions for the ratio $R_{L/TT'}^{D(4)}$ of lon-	

gitudinal and TT' interference structure functions, as functions of β for $x_{\mathbf{P}} = 0.001$ and $Q^2 = 100 \text{ GeV}^2$ **93**

Fig.(4.3)-1÷5 Results of numerical calculations for diffractive slopes $B_{f,i}(x_{\mathbf{P}}, \beta, Q^2)$ for flavors $f = u, d, s, c$ shown as functions of β for $x_{\mathbf{P}} = 0.001$ and $Q^2 = 100 \text{ GeV}^2$ **98**

Fig.(4.4)-1 Gluon structure function $G(x_{\mathbf{P}}, Q^2)$ in GRV [36], CTEQ [38] and MRSS [37] parameterizations in comparison with Born approximation result (with infrared cutoff at $\mu_G = 0.75 \text{ GeV}$) as functions of Q^2 for $x_{\mathbf{P}} = 0.001$ **106**

Fig.(4.4)-2 The average hardness scale $\langle \overline{Q}_{T,LT}^2 \rangle$ for light flavor contribution to transverse and LT interference structure functions. **107**

Fig.(5.1)-1 Sample Feynman diagrams for two-gluon nucleon vertex functions **a)** $V_{1f,c}$, with gluons attached to a single quark; **b)** $V_{2f,c}$, with gluons attached to different quarks.... **117**

Fig.(5.2)-1 Comparison of diffractive (D) spin structure function g_{LT}^D for $Q^2 = 5, 100 \text{ GeV}^2$ and non-diffractive Wandzura-Wilczek [42] (WW) spin structure function g_{LT}^{WW} **122**

Chapter 1

Introduction

Electron-hadron scattering has played an important role in our understanding of the basic structure of nature. This is because stable and point-like objects like the electron are ideal for probing the structure of hadrons. In Deep Inelastic Scattering (DIS) of electrons on protons $ep \rightarrow e'X$ (see Fig.(1)-1a), the electron probes the proton via the exchange of a highly virtual photon γ^* . The virtuality of the photon, its four-momentum squared $Q^2 = -q^2$, is much larger than the characteristic hadronic scale $\sim 1 \text{ GeV}^2$ and thus we resolve the proton structure at small distances $\sim 1/Q^2$. In 1967, experiments on DIS at SLAC discovered that for large Q^2 the cross-section does not fall down with Q^2 and is a function of unitless Bjorken variable x . This *scaling* phenomenon suggests that virtual photon interacts with the proton constituents: structureless spin 1/2 Dirac particles. Quantum Chromodynamics

(QCD) interprets these particles as quarks.

The process of Diffractive DIS (DDIS) of electrons on protons $ep \rightarrow e'p'X$ (see Fig.(1)-1b) has recently received renewed attention due to the commissioning of the Leading Proton Spectrometer (LPS) at HERA. *Diffractive* means that the proton stays intact, so the hadronic state X can be thought of as a result of the virtual photon γ^* diffracting off a proton p . The final state electron e' is detected and this allows one to fix the virtuality Q^2 and Bjorken x . The final state proton p' acquires a small transverse momentum squared $\Delta^2 \lesssim m_p^2$ with respect to its mass m_p . The longitudinal momentum of the proton also changes by a small fraction $x_{\mathbf{P}} \ll 1$ of its initial value, thus the recoiled proton is separated from the hadronic state X , which was created by γ^* diffraction, by a large pseudo-rapidity gap $\eta \approx \log(1/x_{\mathbf{P}})$.

The LPS gives the long-awaited access to both the magnitude and the orientation of the proton transverse momentum transfer Δ of this semi-inclusive process. The measurement of the Δ^2 -dependence of the cross-section component σ^D allows one to find the diffractive slope B^D , defined as coefficients in small Δ^2 decomposition $\sigma^D(\Delta^2) = \sigma^D(\Delta^2 = 0)\{1 - B^D\Delta^2\}$. The transverse orientation of the recoil proton with respect to some other direction defines the azimuthal angle ϕ , and corresponding asymmetry A^D can be found from cross-section ϕ -dependence $\sigma^D(\phi) = \sigma_0^D\{1 + A_i^D \cos \phi\}$. These new observables provide additional handles on the microscopic structure of the proton and allow us to test further the theoretical models of DDIS.

At small Bjorken x , we effectively probe the gluon density of the proton over the whole range of gluon momentum which is governed by the variety of scales in DDIS. In addition to the soft mass scale μ_G^2 , given by the characteristic range of gluon propagation in nucleon matter, and the hard scale Q^2 , in DDIS one gets an access to the intermediate scales coming from the final state analysis. Such scales as the mass m_f^2 of different quark flavors and the mass M^2 of the final diffractive state X allow one to probe in more details the semi-hard regime in different cross-section components.

Diffraction of hadrons and/or (virtual) photons is a phenomenon very appealing to physical intuition because it combines particle and wave-like aspects of high-energy scattering. A very simple physical picture for hadronic diffraction is based on the optical model developed a long time ago. The beam hadron at very high energy is described in quantum mechanics as a complicated superposition of virtual states. At short distances, QCD radiation causes fluctuations of its parton structure. Due to Lorentz contraction of this ultrarelativistic system, the Fock states are in fact eigenstates of the interaction. In the diffraction, the interaction with the target particle causes the attenuation of the beam particle Fock states. As a result the scattered state is different from the beam state and new exclusive and continuum states are *diffracted into existence*.

In this diffractive dissociation of the beam particle, the cross-section system center-of-mass energy \sqrt{s} dependence is similar to that of elastic scattering: $\sigma_{tot} = \sigma_0(s/s_0)^\epsilon + \sigma_1\sqrt{s_0/s}$, where $\epsilon \sim 0.1$ and σ_0 with σ_1 characterize the reaction. In the Regge language the term

$\sigma_0(s/s_0)^\epsilon$, which grows with the energy s , is coming from *Pomeron* exchange in the t -channel (see Fig.(1)-2a,b), and Pomeron is treated as the quasiparticle \mathbf{IP} with vacuum quantum numbers. Other intermediate particles with meson quantum numbers contribute to the term $\sigma_1\sqrt{s_0/s}$ which is suppressed at high energies. In perturbative QCD, the Pomeron is just a label for the intermediate two-gluon ladder (see Fig.(1)-2c). For a review on the Regge phenomenology in diffraction see [1]. The transferred momentum $t = -\Delta^2$ dependence of the diffractive cross-section is characterized by the diffractive slope B^D which depend strongly on the excitation energy of the beam particle. The target particle contribution to the diffractive slope is proportional to its transverse area.

The microscopic QCD picture of DIS and DDIS at small Bjorken x was developed in the early 90's by Mueller [2], and by Nikolaev and Zakharov [3]. In this picture, the $\gamma^*p \rightarrow Xp'$ process is described as a grazing, quasielastic scattering of the multiparton Fock states of the virtual photon by the proton. The DDIS is treated in the color-dipole model [4] in terms of diffraction of the quark-antiquark ($q\bar{q}$) light-cone Fock components of the virtual photon on the target proton. This interpretation of DDIS is possible since for small Bjorken $x \ll 1$, the virtual photon transforms into a $q\bar{q}$ pair at a large distance ahead of the proton, $\delta z \sim 1/m_p x \gg R_p$, compared to its size R_p . The color-dipole consists only of $q\bar{q}$ pair for the cases of low and intermediate continuum mass excitation $M^2 \lesssim Q^2$, and of vector meson production. More complicated Fock states with extra gluons and/or $q\bar{q}$ pairs contribute for large continuum masses $M^2 \gg Q^2$. The γ^*p center-of mass energy $s = Q^2/x$ is large for

$x \ll 1$, and the two-gluon exchange in the t -channel of the $\gamma^*p \rightarrow (q\bar{q})p'$ interaction gives the dominant contribution. In the equivalent parton language, which is commonly used in the standard DIS, this means that at small x the virtual photon probes the gluon structure of the proton by interaction with its daughter (sea) quarks.

The color dipole approach allows one to answer many important questions in DDIS such as

- what is the twist structure, or dependence of DDIS observables on the virtuality of the photon Q^2 (the power of $1/Q$ in DIS cross-sections is called *twist*),
- what are the relevant scales in this truly multi-scale problem,
- what is the flavor content of the DDIS observables,
- what happens to the partons' helicities and how are they related to the hadron and virtual photon polarizations,
- is DDIS a soft or a hard process, and to what extent is pQCD applicable?

The light-cone formalism provides this DDIS model with a natural framework as the trajectories of particles cluster close to the light-cone in high-energy processes. Combined with the infinite momentum frame, this formalism allows one to separate effectively large and small scale longitudinal and transverse momenta. There is also a great deal of simplification in the calculations because it is easier to estimate the contributions of different Feynman diagrams and safely neglect those that are small in the high energy limit.

In a series of papers [3]-[6] Nikolaev et al. used the color-dipole approach to calculate

the forward ($\Delta = 0$) leading twist transverse and longitudinal diffractive structure functions. This light-cone pQCD approach was extended by the author to the evaluation of the azimuthal angle and higher twist components of the diffractive structure functions, and to the calculation of diffractive slopes. The first calculations of the cross-sections integrated over the diffractive state mass M^2 with non-zero momentum transfer ($\Delta \neq 0$) were performed by the author and Zakharov in 1992 with the use of gluon structure functions in the Born approximation, and with an infrared cutoff imposed on the radius of the perturbative gluon propagation. In the past two years, modern parameterizations of the gluon structure functions were incorporated by the author into the calculations of semi-inclusive DDIS with nonzero momentum transfer $\Delta^2 \neq 0$ and fixed continuum mass M^2 . This dissertation is based on the results of a series of papers published by the author in [7]-[13] in collaboration with Nikolaev and others. Some of these results were presented by the author at the 6th International Workshop on Deep Inelastic Scattering and QCD (DIS'98).

While working on his Ph.D. at Virginia Tech, the author made the following contributions using the color-dipole approach in DDIS. The direct perturbative QCD evaluation was performed of higher-twist corrections to the diffractive structure functions which are dominant for low-mass continuum excitation, $M^2 \gtrsim 4m_f^2$. It was shown that the higher twist transverse structure function has the same twist and characteristic pQCD scale as the longitudinal component. Some nontrivial effects were found in the diffractive excitation of the continuum with $\Delta \neq 0$, such as a rapid variation of the diffractive slope with the mass of

the diffractive state M^2 . It was shown how different interaction regions with different sizes in impact parameter space contribute to the diffractive slopes of the cross-section components. Azimuthal asymmetries were calculated in the recoil proton and jet plane directions and a new procedure was developed to use longitudinal-transverse interference effects in order to extract a model-independent and abnormally large longitudinal/transverse cross-section ratio in DDIS. A method was proposed to use transverse-transverse interference to measure directly the higher-twist contribution to the transverse cross-section. Exclusive-inclusive duality between the diffractive production of vector mesons and low-mass continuum excitation was extended to the s-channel helicity non-conserving cross-sections with different azimuthal angle and polarization dependence. Important diffractive contributions to the spin structure functions were evaluated and shown to have a rapid rise toward small Bjorken x . Universal software was developed and utilized to calculate the DDIS observables with the use of modern gluon structure function parameterizations. Together with collaborators, the author completed an analysis of multi-scale regimes in DDIS and of the applicability of pQCD.

The present thesis is organized as follows. In Chapter 2 we introduce kinematical variables of DDIS for two cases: continuum excitation in which the final hadronic state X is the result of the $q\bar{q}$ pair hadronization (thus *semi*-inclusive since only the recoil proton is detected in the final state), and vector meson production in which X is the vector meson V only (thus *exclusive*). Then, we use light-cone perturbation theory to calculate the leptonic and hadronic contributions to the total DDIS cross-section. We calculate the helicity

amplitudes of quark-antiquark excitation of the virtual photon. The interaction of the $q\bar{q}$ pair with the proton is mediated at small- x by colorless two-gluon exchange. We show how gluons with different momenta contribute to the gluon structure functions.

In Chapter 3 we calculate the DDIS cross-sections for continuum excitation and show the leading twist contributions for different polarization and azimuthal angle components. For each case we analyze the emerging pQCD scales which give dominant contributions. For the case of transverse polarization, we evaluate and discuss the higher-twist components. Next, we calculate average hard scales in our problem and establish an important sum-rule for the M^2 -integrated components of the diffractive cross-section. We proceed with calculations of low-mass continuum excitation, and diffractive vector meson production dual to it. We find that exclusive-inclusive duality correspondence holds for all polarization and azimuthal angle components. We conclude Chapter 3 by a physically intuitive impact parameter representation of the M^2 -integrated cross-sections and the amplitudes of vector meson production.

In Chapter 4 we convert the cross-sections into conventional proton structure functions and diffractive slopes, and perform numerical calculations which we compare with approximate analytical results. Then, we analyze the ratios of the structure function components, which to some extent are independent of the gluon structure function. This allows us to use azimuthal asymmetries to separate the transverse and longitudinal components, and the higher twist contributions to the total structure functions. Next, we evaluate the diffractive

slopes of the different components and discuss the existing gluon structure function parameterizations and their extrapolation to the infrared region. We conclude Chapter 4 with the analysis of the hardness of the characteristic scales and the general validity of our pQCD approach.

In Chapter 5 we apply the light-cone formalism to the proton sector of the interaction, calculating a relativistic wave function of the nucleon and using it to find the spin-flip and spin-conserving vertex functions. Finally, we use the above results to evaluate the diffractive contribution to the conventional spin structure function of the proton.

In the last Chapter 6 we summarize all these results and give a perspective of future calculations. The figures are shown at the end of each section and labeled correspondingly.

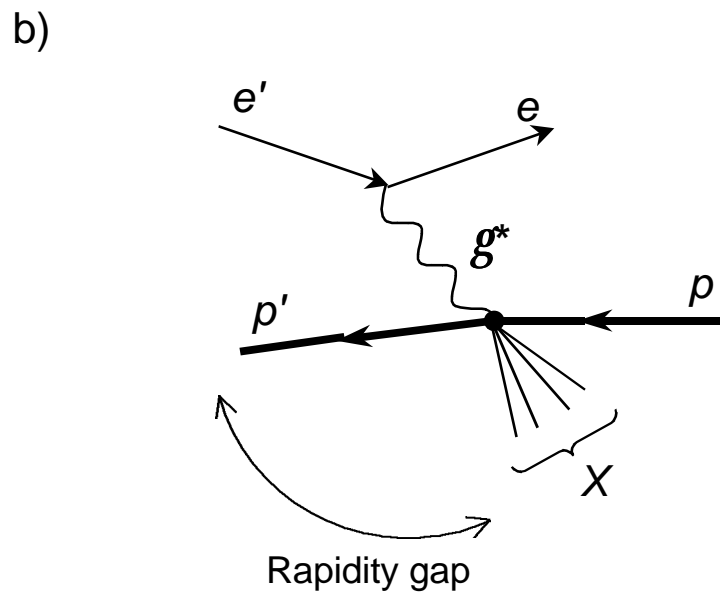
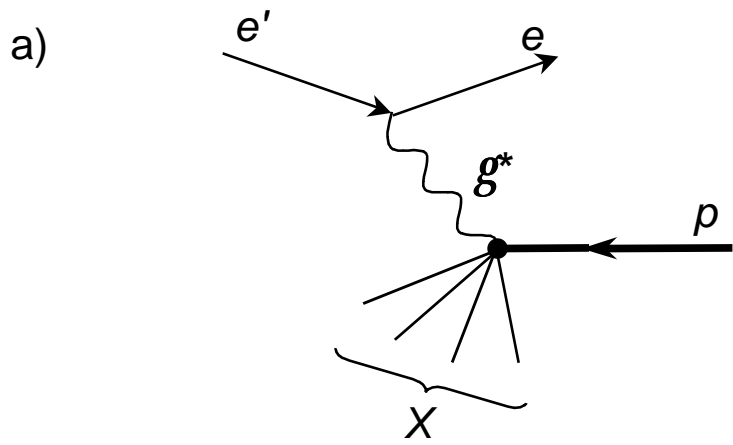


Fig.(1)-1

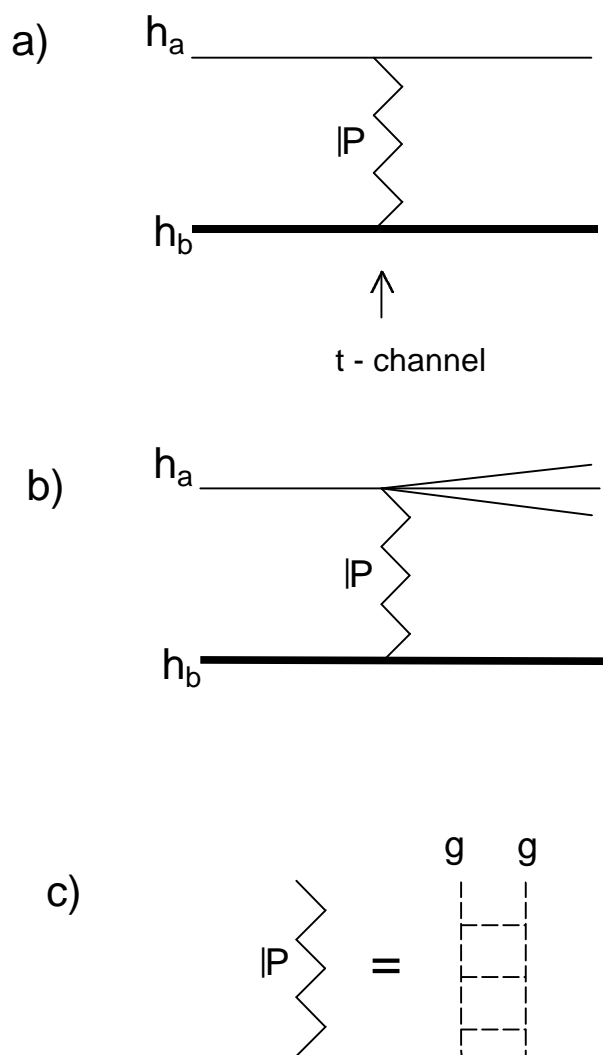


Fig.(1)-2

Chapter 2

Light-cone perturbation theory

In this chapter we introduce the light-cone perturbative QCD technique in the color dipole approach to DDIS following Refs. [3]-[6]. The color dipole calculations in the zero-momentum transfer limit $\Delta = 0$ were performed by Nikolaev et al. in Refs. [5] and [6]. The longitudinal-transverse and transverse-transverse interference components of the diffractive continuum excitation cross-sections and the helicity amplitudes in the color dipole model at nonzero momentum transfer $\Delta \neq 0$ were obtained by the author and reported in Ref. [9]. We show here all the details of the calculations and analyze the contributions from different parts of the Feynman diagrams. All steps have very clear physical interpretations which is the main advantage of old-fashioned perturbation theory applied in the infinite momentum light-cone frame.

2.1 Kinematics

In diffractive DIS the experimentally observed process is the scattering of a lepton off a proton

$$lp \rightarrow l'p'X$$

with the detection of the recoil proton. It is thus semi-inclusive whereas standard DIS is fully inclusive in the hadronic sector and the recoil proton is not detected: $lp \rightarrow l'X$. The underlying subprocess in DDIS is the diffractive excitation of the virtual photon $\gamma^*p \rightarrow Xp'$, where one-photon exchange dominates due to the smallness of the electroweak coupling (fine structure constant) $\alpha_{em} \approx 1/137$. The diagram for DDIS of an electron on a proton is shown in Fig.(2.1)-1a, p_e and p'_e are the momenta of the initial and final (recoiled) electron, p and p' - momenta of the initial and final (recoiled) proton, and q_M is the total momentum of the diffractive state X . Momentum conservation states:

$$p_e + p = p'_e + p' + q_M, \quad (2.1)$$

and we define the momentum transferred from the electron, equal to the virtual photon momentum, as

$$q = p_e - p'_e. \quad (2.2)$$

We will neglect the mass of the electron, compared to all other masses in our problem, so

$$p_e^2 = p'^2_e = 0. \quad (2.3)$$

The proton mass m_p constrains the momenta:

$$p^2 = p'^2 = m_p^2. \quad (2.4)$$

We also introduce standard DDIS masses: the invariant mass M of the diffractive state X ,

$$q_M^2 = M^2, \quad (2.5)$$

the virtuality of the photon Q ,

$$q^2 = -Q^2, \quad (2.6)$$

the γ^*p center of mass energy squared s ,

$$(q + p)^2 = s, \quad (2.7)$$

and the ep center of mass energy squared S ,

$$(p_e + p)^2 = S. \quad (2.8)$$

Standard DIS unitless ratios are: the Bjorken scaling variable

$$x = \frac{Q^2}{Q^2 + s}, \quad (2.9)$$

defined here in the limit of $Q^2 \gg m_p^2$, which in the parton model (see [14] for a quick review)

is the fraction of target nucleon's momentum carried by the struck quark, and the inelasticity

$$y = \frac{Q^2}{Sx}, \quad (2.10)$$

which is the fraction of the electron's energy carried away by the virtual photon.

In DDIS we have two additional variables:

$$\beta = \frac{Q^2}{Q^2 + M^2}, \quad (2.11)$$

and the counterpart of the leptonic variable y , usually denoted as

$$x_{\mathbf{P}} = \frac{x}{\beta}, \quad (2.12)$$

which is the fraction of the proton's energy (longitudinal momentum) taken away. We neglected the small momentum transfer

$$t = (p - p')^2 = -\Delta^2, \quad (2.13)$$

compared to Q^2 in (2.11). We will perform calculations in the following limits of kinematical variables:

$$x, x_{\mathbf{P}}, y \ll 1 \quad (2.14)$$

and

$$\Delta^2 \ll m_p^2 \ll Q^2 \ll s. \quad (2.15)$$

We discuss the physical meaning of these approximations in more detail below.

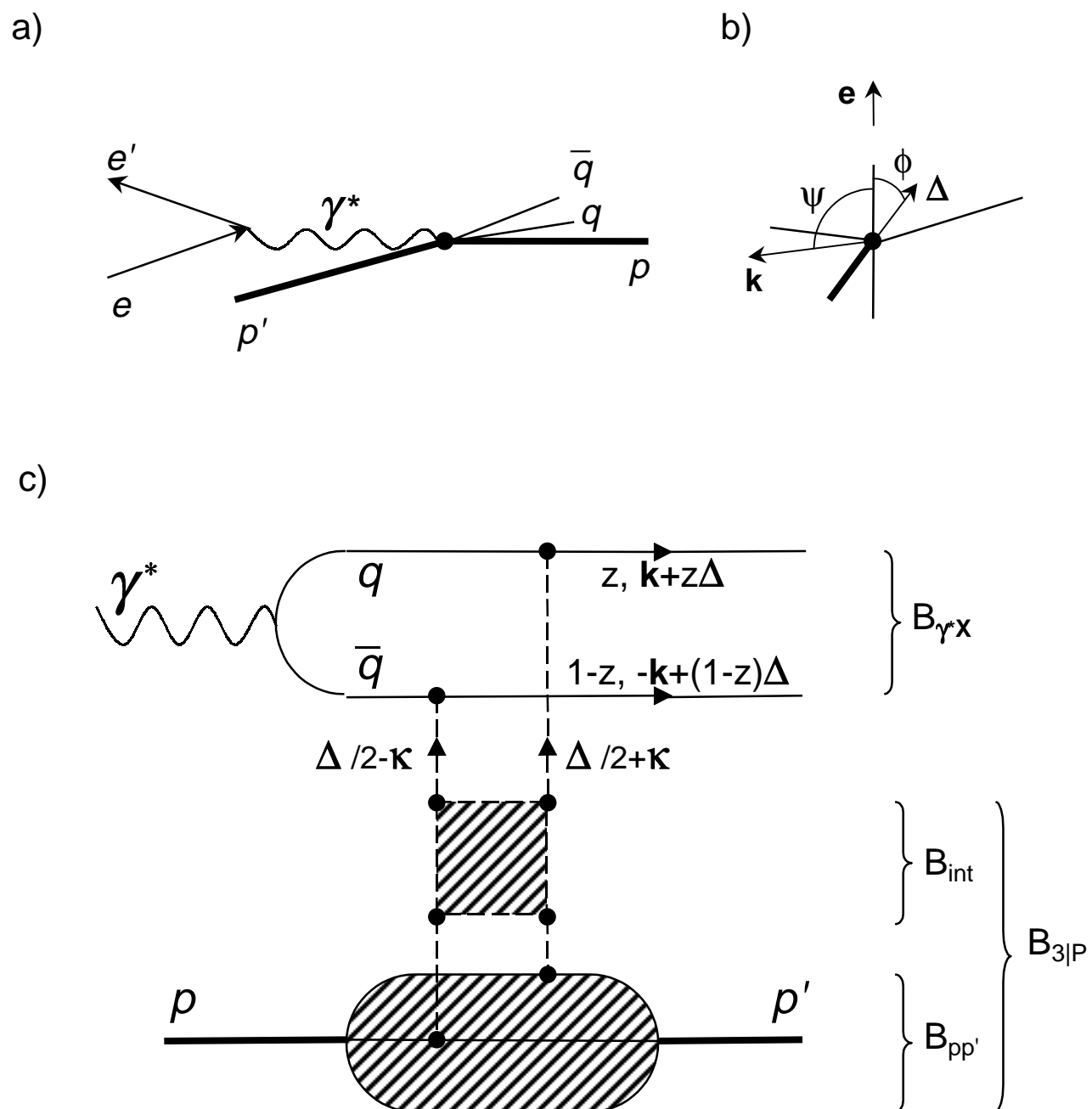


Fig.(2.1)-1

2.2 Leptonic part

We will work in the photon-proton center of mass frame for $x \ll 1$, with large energy squared $s = Q^2/x$, larger than any other scale. Effectively, it is an infinite momentum frame with longitudinal momentum $\sqrt{s} \rightarrow \infty$. We choose the z-axis to be directed along the virtual photon momentum. See Fig.(2.1)-1. Then, for the momenta of the external particles we have (recall eqs. (2.1), (2.2)), using light-cone parameterization as in (A.1),

$$q = \left(\sqrt{s}, -\frac{Q^2}{\sqrt{s}}, \mathbf{0} \right), \quad (2.16)$$

$$q_M = \left(\sqrt{s}, \frac{M^2}{\sqrt{s}}, \mathbf{\Delta} \right), \quad (2.17)$$

$$p = \left(\frac{m_p^2}{\sqrt{s}}, \sqrt{s}, \mathbf{0} \right), \quad (2.18)$$

$$p' = \left(\frac{m_p^2}{\sqrt{s}}, \sqrt{s}, -\mathbf{\Delta} \right), \quad (2.19)$$

where $\mathbf{\Delta}$ is the small transverse momentum, transferred from the proton, $-t = \mathbf{\Delta}^2 \ll m_p^2 \ll s$. We neglected the longitudinal transferred momentum in our infinite momentum frame. One should note that for the lower portion of graph in Fig.(2.1)-1b, which is the proton sector, the $(-)$ light-cone components dominate and the $(+)$ components are determined from the on-shell conditions. However, we primarily deal with the photon sector of the interaction for which the Feynman rules introduced in Ref. [15] apply, and in which case the $(+)$ component is dominant.

Four polarization vectors can be defined: longitudinal (L), scalar (S) and two transverse

(T) and (T'):

$$e_L \equiv \frac{q}{Q} = \left(\frac{\sqrt{s}}{Q}, -\frac{Q}{\sqrt{s}}, \mathbf{0} \right), \quad (2.20)$$

$$e_S = \left(\frac{\sqrt{s}}{Q}, \frac{Q}{\sqrt{s}}, \mathbf{0} \right), \quad (2.21)$$

$$e_T = (0, 0, \mathbf{e}) = (0, 0, e_1, e_2), \quad (2.22)$$

$$e_{T'} = (0, 0, \mathbf{e}') = (0, 0, -e_2, e_1). \quad (2.23)$$

These vectors are chosen to be orthogonal to each other $e_i \cdot e_j = (\mathbf{e} \mathbf{e}') = 0$ for $i \neq j = S, L, T, T'$ and are normalized as $e_S^2 = -e_L^2 = -e_T^2 = -e_{T'}^2 = \mathbf{e}^2 = \mathbf{e}'^2 = 1$. Using this complete basis of four-vectors, we write the momenta of the initial and final electrons as

$$p_e = p_e^S e_S + p_e^L e_L + p_e^T e_T, \quad (2.24)$$

$$p'_e = p_e^S e_S - p_e^L e_L + p_e^T e_T. \quad (2.25)$$

One can see that, as defined above, the transverse polarization vector e_T is tangential to the (e, e') plane and $e_{T'}$ is perpendicular to it. In our approximation of small Bjorken x we have the following coefficients for p_e, p'_e decomposition:

$$p_e^S = \frac{Q}{y} \left(1 - \frac{1}{2}y \right), \quad p_e^L = \frac{Q}{2}, \quad p_e^T = \frac{Q}{y} \sqrt{1-y}. \quad (2.26)$$

The differential cross-section can be written as convolution of leptonic and hadronic tensors $d\sigma^D = \mathcal{L}^{\mu\nu} \mathcal{H}_{\mu\nu}$. The standard leptonic tensor

$$\mathcal{L}^{\mu\nu} = Tr [\gamma^\mu \hat{p} \gamma^\nu \hat{p}'] = 4 [p_e^\mu p_e'^\nu + p_e'^\mu p_e^\nu - (p_e \cdot p_e') \delta^{\mu\nu}], \quad (2.27)$$

where $\hat{p} \equiv p_\sigma \gamma^\sigma$, can be rewritten using (2.24-2.26) as the γ^* polarization density matrix

$$\begin{aligned} \mathcal{L}^{\mu\nu} = & \frac{8Q^2}{y^2} \left[(1-y) \cdot e_S^\mu e_S^\nu + \left(1-y + \frac{1}{2}y^2\right) \cdot \frac{1}{2}(e_T^\mu e_T^\nu + e_{T'}^\mu e_{T'}^\nu) \right. \\ & \left. + (1-y) \cdot \frac{1}{2}(e_T^\mu e_T^\nu - e_{T'}^\mu e_{T'}^\nu) + (2-y)\sqrt{1-y} \cdot \frac{1}{2}(e_S^\mu e_T^\nu + e_T^\mu e_S^\nu) \right]. \end{aligned} \quad (2.28)$$

One can see that in the limit of $y \ll 1$, the soft photon is polarized in the (e, e') plane. If we contract $\mathcal{L}^{\mu\nu}$ with its hadronic counterpart $\mathcal{H}_{\mu\nu}$, we will get the total DDIS cross-section, written as a sum of four different components:

$$\begin{aligned} Q^2 y \frac{d\sigma(ep \rightarrow e'p'X)}{dQ^2 dy} = & \frac{\alpha_{em}}{\pi} \left[\left(1-y + \frac{1}{2}y^2\right) \sigma_T^D + (1-y) \sigma_L^D \right. \\ & \left. + (1-y) \sigma_{TT'}^D + \left(1 - \frac{y}{2}\right) \sqrt{1-y} \sigma_{LT}^D \right], \end{aligned} \quad (2.29)$$

where the σ_j^D 's are the diffractive excitation cross-section components of the process $\gamma^* p \rightarrow Xp'$, which have labels $j = T, L, TT', LT$, standing for the transverse (T), longitudinal (L , the misnomer notation used in modern literature for scalar photons), longitudinal-transverse interference (LT) and transverse-transverse interference (TT') cross-sections. In what follows we will consider the standard case of $y \ll 1$, and all factors multiplying the σ_j^D 's in (2.29) become equal to 1.

2.3 Hadronic part

By virtue of the optical theorem, we need to calculate the imaginary part of the forward Compton amplitude $\gamma_{\mu}^* p \rightarrow \gamma_{\nu}^* p$ to obtain the cross-section for $\gamma_{\mu}^* p \rightarrow X p'$. The sample diagram for this process is shown in Fig.(2.3)-1a. The leading contribution to DDIS with intermediate and low invariant mass $M^2 \lesssim Q^2$ and small x is the excitation of the quark-antiquark $q\bar{q}$ Fock state in the photon by a colorless double gluon (labeled Pomeron) exchange. The calculations of Ref. [3] show that multi-parton Fock states like $q\bar{q}g$ contribute for large mass continuum excitation $M^2 \gg Q^2$, $\beta \lesssim 0.1$. For large $x \gtrsim 0.1$ region, the gluon distribution in the proton no longer dominates and one needs to take into account processes where virtual photon interacts directly with valence quarks (see Ref. [18] for corresponding calculations). In this thesis we use the existing gluon structure function parameterizations (see discussion in Chapter 4) as input for the bottom blobs in Fig.(2.3)-1a. For the QCD evaluation of gluon structure functions and its relation to DDIS Regge phenomenology see Ref. [16] and references therein.

We introduce four-momenta: k_i of the quark and \bar{k}_i of the antiquark,

$$k_i = \left(z\sqrt{s}, \frac{\mathbf{k}_i^2 + m_f^2}{z\sqrt{s}}, \mathbf{k}_i \right), \quad (2.30)$$

$$\bar{k}_i = \left((1-z)\sqrt{s}, \frac{\mathbf{k}_i^2 + m_f^2}{(1-z)\sqrt{s}}, -\mathbf{k}_i \right), \quad (2.31)$$

which combine to form the momentum of the virtual photon (2.16)

$$q = k_i + \bar{k}_i. \quad (2.32)$$

In Eqs. (2.30) and (2.31), z and $(1 - z)$ are the fractions of the photon's longitudinal momentum, carried by the quark and the antiquark, respectively, and $\pm \mathbf{k}$ are the transverse momenta.

We use the prescriptions of *old-fashioned* (Heitler-type, time ordered, pre-Feynman) perturbation theory [15] and calculate the *energy denominators*, for which we subtract light-cone *energies* (which are not conserved, see Eq. (A.1)) of the incident (γ^*) and the intermediate ($q\bar{q}$) states, q^- and $k^- + \bar{k}^-$,

$$D_\gamma = q^- - k_i^- - \bar{k}_i^- = -\frac{1}{z(1-z)\sqrt{s}} \cdot (\mathbf{k}_i^2 + m^2 + z(1-z)Q^2). \quad (2.33)$$

The $\gamma^*(j, q) q(\lambda_i, k_i) \bar{q}(\bar{\lambda}_i, \bar{k}_i)$ vertex with definite helicities λ_i of the quark and $\bar{\lambda}_i$ of the anti-quark, and polarization j of the virtual photon, according to the rules of light-cone perturbation theory [15], is

$$G_{\gamma_j}^{\lambda_i, \bar{\lambda}_i} = -\frac{\bar{v}_{\bar{\lambda}_i}(\bar{k}_i)}{\sqrt{\bar{k}_i^+}} \Gamma_\mu \frac{u_{\lambda_i}(k_i)}{\sqrt{k_i^+}} \cdot e_j^\mu, \quad (2.34)$$

where $\Gamma_\mu = \gamma_\mu$ is the standard electromagnetic interaction vertex and $u_\lambda(k_i)$ with $v_{\bar{\lambda}}(\bar{k}_i)$ are light-cone helicity spinors. See Eqs. (A.4), (A.5). For the matrix elements (2.34) we find

$$G_{\gamma_j}^{\lambda_i, \bar{\lambda}_i} = (-1)^{\lambda_i + \bar{\lambda}_i} [G_{\gamma_j}^{-\lambda_i, -\bar{\lambda}_i}]^*, \quad (2.35)$$

$$G_{\gamma_T}^{+-} = \frac{1}{z(1-z)\sqrt{s}} \cdot [(1-2z)(\mathbf{e}\mathbf{k}_i) + i(\mathbf{e} \times \mathbf{k}_i)], \quad (2.36)$$

$$G_{\gamma_T}^{++} = -\frac{1}{z(1-z)\sqrt{s}} \cdot m(e_1 - ie_2), \quad (2.37)$$

$$G_{\gamma_L}^{+-} = -\frac{1}{z(1-z)\sqrt{s}} \cdot 2z(1-z)Q, \quad (2.38)$$

$$G_{\gamma_L}^{++} = 0. \quad (2.39)$$

Each gluon enters with a Feynman gauge propagator factor $g_{\mu\nu}$, for which the following decomposition holds

$$g^{\mu\nu} = g_{\perp}^{\mu\nu} + n_{(+)}^{\mu}n_{(-)}^{\nu} + n_{(-)}^{\mu}n_{(+)}^{\nu}, \quad (2.40)$$

where we used light-cone vectors $n_{(+)} = (1, 0, \mathbf{0})$ and $n_{(-)} = (0, 1, \mathbf{0})$, and the index μ is considered to enter the $q(\bar{q})g\bar{q}(\bar{q})$ vertex of the $q\bar{q}$ pair. For the $q(\lambda_i, k_i)gq(\lambda_f, k_f)$ vertices we have, using (A.4) and (A.5), the dominant contribution in the infinite momentum frame

$$G_{g^{(+)}}^{\lambda_i, \lambda_f} = \frac{\bar{u}_{\lambda_f}(k_f)}{\sqrt{k_f^+}} \gamma^+ \frac{u_{\lambda_i}(k_i)}{\sqrt{k_i^+}} = 2\delta_{\lambda_i \lambda_f}, \quad (2.41)$$

which contracts with the last term in (2.40), containing the nonzero component $n_{(-)}^- = 1$. This leads to the conservation of (anti)quark helicity $\lambda_i = \lambda_f$ in our infinite-momentum frame.

Denoting the $q\bar{q}$ loop transverse momentum as \mathbf{k} we have

$$\mathbf{k}_f = \mathbf{k} + z\mathbf{\Delta} = \mathbf{r} + \frac{1}{2}\mathbf{\Delta}, \quad (2.42)$$

$$\bar{\mathbf{k}}_f = -\mathbf{k} + (1-z)\mathbf{\Delta} = -\mathbf{r} + \frac{1}{2}\mathbf{\Delta}, \quad (2.43)$$

for momenta k_f and \bar{k}_f of the quark and antiquark in the final $q\bar{q}$ state (the same for all diagrams), where we introduced a useful transverse vector

$$\mathbf{r} \equiv \mathbf{k} - \frac{1}{2}(1-2z)\mathbf{\Delta} = \frac{1}{2}(\mathbf{k}_f - \bar{\mathbf{k}}_f). \quad (2.44)$$

In our infinite-momentum frame, we neglect longitudinal momentum transfer; and thus the longitudinal momentum fractions, z and $(1-z)$, stay unchanged for the quark and antiquark.

The final quark and antiquark constitute the diffractive state $X = q\bar{q}$ with momentum

$$q_M = k_f + \bar{k}_f. \quad (2.45)$$

The invariant mass of the diffractive state, $X = q\bar{q}$, is then given by

$$M^2 = (k_f + \bar{k}_f)^2 = \frac{\mathbf{k}^2 + m_f^2}{z(1-z)}, \quad (2.46)$$

where we neglected $\mathbf{\Delta}$ in (2.44) in our approximation of $\Delta^2 \ll m_f^2$.

We sum over four different diagrams with two gluons, with momenta $\mathbf{\Delta}_{1,2} = \mathbf{\Delta}/2 \pm \boldsymbol{\kappa}$ ($\mathbf{\Delta} = \mathbf{\Delta}_1 + \mathbf{\Delta}_2$ is a total gluon momentum and $\boldsymbol{\kappa}$ is a gluon loop momentum), attached to the quark lines. See Fig.(2.3)-2. With the final quark momentum \mathbf{k}_f fixed, the quark at the $\gamma^* q\bar{q}$ vertex will have a different momentum \mathbf{k}_i for each diagram. The sign factor $c_i = \pm 1$ appears for diagrams with gluons connected to the same/different quark lines. We combine vertices (2.34) and energy denominators (2.33) in the unintegrated reduced amplitude of the $\gamma^* \rightarrow q\bar{q}$ transition

$$A_{\gamma_j}^{\lambda_f \bar{\lambda}_f} \equiv \sum_i c_i \frac{G_{\gamma_j}^{\lambda_f, \bar{\lambda}_f}(\mathbf{k}_i)}{D_\gamma(\mathbf{k}_i)}, \quad (2.47)$$

where the summation is over the four diagrams in Fig.(2.3)-2. It is convenient to use the virtual photon circular polarization vectors with definite helicity $\lambda = \pm 1$

$$\mathbf{e}_{\pm} = -\frac{1}{\sqrt{2}}(\pm \mathbf{e} + i\mathbf{e}'), \quad (2.48)$$

with $\mathbf{e}_{\pm}^* \mathbf{e}_{\pm} = 1$. With the use of $\mathbf{n}_{\pm} = -(\pm, i)/\sqrt{2}$ one can find a compact expression for the unintegrated reduced helicity amplitudes of the $\gamma_{\lambda}^* \rightarrow q_{\lambda_f} \bar{q}_{\bar{\lambda}_f}$ transition

$$\begin{aligned} A_{\lambda}^{\lambda_f \bar{\lambda}_f} &= -2z(1-z)Q \phi_2 \delta_{\lambda 0} \delta_{\lambda_f - \bar{\lambda}_f} - \lambda(\mathbf{n}_{\lambda}^* \mathbf{e}_{\lambda}) m_f \phi_2 \delta_{\lambda \lambda_f} \delta_{\lambda \bar{\lambda}_f} \\ &\quad + \sqrt{2}\lambda(\mathbf{e}_{\lambda} \phi_1) [(1-z) \delta_{\lambda \lambda_f} - z \delta_{\lambda \bar{\lambda}_f}] \delta_{\lambda_f - \bar{\lambda}_f}. \end{aligned} \quad (2.49)$$

We introduced the sum

$$\phi_j \equiv \sum_i c_i \psi_j(\mathbf{k}_i) = \psi_j\left(\mathbf{r} + \frac{1}{2}\mathbf{\Delta}\right) + \psi_j\left(\mathbf{r} - \frac{1}{2}\mathbf{\Delta}\right) - \psi_j(\mathbf{r} + \boldsymbol{\kappa}) - \psi_j(\mathbf{r} - \boldsymbol{\kappa}) \quad (2.50)$$

over functions

$$\psi_1(\mathbf{k}_i) \equiv \mathbf{k}_i \cdot \psi_2(\mathbf{k}_i) \equiv \frac{\mathbf{k}_i}{\mathbf{k}_i^2 + \varepsilon^2}, \quad (2.51)$$

where ψ_2 has a meaning of the virtual photon light-cone wave function and

$$\varepsilon^2 \equiv m_f^2 + z(1-z)Q^2 \quad (2.52)$$

is sometimes called the *transverse mass* of the quark. One can see from Eq. (2.49) that ϕ_1 corresponds to $\gamma_{\lambda}^* \rightarrow q_{\lambda_f} \bar{q}_{\bar{\lambda}_f}$ transitions with altering helicity $\lambda \neq \lambda_f + \bar{\lambda}_f$, and ϕ_2 corresponds to helicity conservation $\lambda = \lambda_f + \bar{\lambda}_f$.

The light-cone vectors $n'_{(+)}$ of Eq. (2.40) enter the $pp'gg$ contribution in Fig.(2.3)-1a, which gives the off-forward unintegrated gluon density in the proton (see discussion in Seq.2.4

and Sec.4.4): $f(x_{\mathbf{P}}, \boldsymbol{\kappa}, \boldsymbol{\Delta})$. It is customary to single out the factor $1/\kappa^4$ which emerges from the denominators $\boldsymbol{\Delta}_1^2$ and $\boldsymbol{\Delta}_2^2$ in the gluon propagators for the forward scattering case $\Delta = 0$. The $\boldsymbol{\Delta}$, $\boldsymbol{\kappa}$ and $x_{\mathbf{P}}$ dependence of the gluon density matrix will be discussed in the next chapter. We combine the γ^*X and $pp'gg$ contributions into an amplitude of the $\gamma^*p \rightarrow Xp'$ transition (see Fig.(2.1)-1b), integrated over the gluon loop transverse momentum $\boldsymbol{\kappa}$,

$$A_{j;\lambda_f\bar{\lambda}_f}^D \equiv \int d^2\boldsymbol{\kappa} \frac{f(x_{\mathbf{P}}, \boldsymbol{\kappa}, \boldsymbol{\Delta})}{\kappa^4} A_j^{\lambda_f\bar{\lambda}_f}. \quad (2.53)$$

We also define the helicity changing and conserving amplitudes Φ_1 and Φ_2 (first introduced for the $\Delta = 0$ case in Ref. [3]):

$$\Phi_i = \int d^2\boldsymbol{\kappa} \frac{f(x_{\mathbf{P}}, \boldsymbol{\kappa}, \boldsymbol{\Delta})}{\kappa^4} \phi_i. \quad (2.54)$$

Finally, we introduce the vector meson polarization vectors, which are used in the calculations of vector meson diffractive production

$$V_S = \left(\frac{\sqrt{s}}{M}, -\frac{M}{\sqrt{s}}, \mathbf{0} \right) \quad (2.55)$$

$$V_L = \frac{q_M}{M} = \left(\frac{\sqrt{s}}{M}, \frac{M}{\sqrt{s}}, \mathbf{0} \right), \quad (2.56)$$

$$V_T = (0, 0, \mathbf{V}) = (0, 0, V_1, V_2), \quad (2.57)$$

$$V_{T'} = (0, 0, \mathbf{V}') = (0, 0, -V_2, V_1). \quad (2.58)$$

These vectors are orthogonal $V_i \cdot V_j = (\mathbf{V}\mathbf{V}') = 0$ for $i \neq j = S, L, T, T'$ and are normalized by $-V_S^2 = V_L^2 = -V_T^2 = -V_{T'}^2 = \mathbf{V}^2 = \mathbf{V}'^2 = 1$. We also use the circular polarization vectors

with definite helicity

$$\mathbf{V}_\pm = -\frac{1}{\sqrt{2}}(\pm\mathbf{V} + i\mathbf{V}'). \quad (2.59)$$

Employing the same technique as used for the $\gamma^* q\bar{q}$ vertex, one finds the unintegrated amplitude for the $V(\lambda_V, q_m) q(\lambda_f, k_f) \bar{q}(\bar{\lambda}_f, \bar{k}_f)$ vertex

$$\begin{aligned} A_{\lambda_V; \lambda_f \bar{\lambda}_f}^V &= -2z(1-z)M \delta_{\lambda_V 0} \delta_{\lambda_f - \bar{\lambda}_f} - \lambda_V (\mathbf{n}_{\lambda_V}^* \mathbf{V}_{\lambda_V}) m_f \delta_{\lambda_V \lambda_f} \delta_{\lambda_f \bar{\lambda}_f} \\ &\quad + \sqrt{2} \lambda_V (\mathbf{V}_{\lambda_V} \mathbf{k}) [(1-z) \delta_{\lambda_V \lambda_f} - z \delta_{\lambda_V \bar{\lambda}_f}] \delta_{\lambda_f - \bar{\lambda}_f}, \end{aligned} \quad (2.60)$$

in which we used the plain γ_μ matrix (see [19] for discussion of S-D mixing in vector meson wave function) in the $\Gamma_\mu^V = \gamma_\mu \Gamma^V$ vertex. Together with the energy denominator

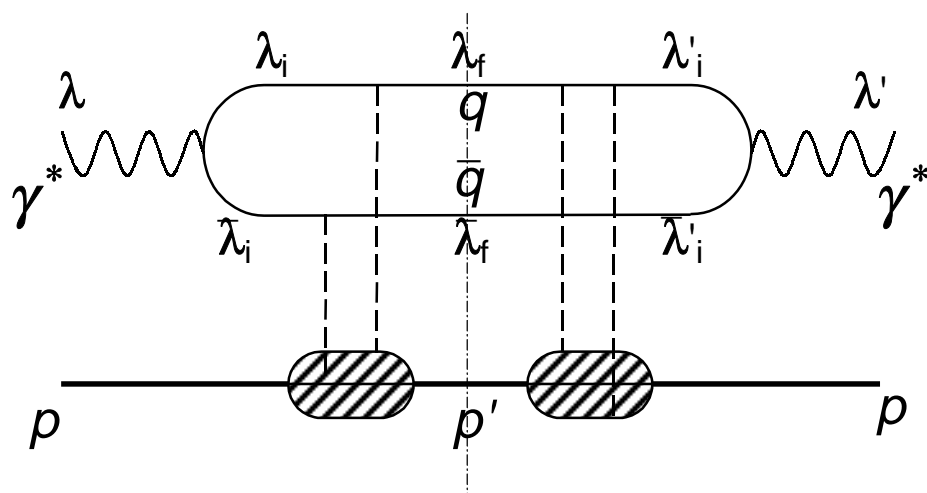
$$D_V = q_V^- - k_i^- - \bar{k}_i^- = -\frac{1}{\sqrt{s}} \cdot (M^2 - M_V^2), \quad (2.61)$$

the reduced vertex Γ^V constitutes the vector meson light-cone wave function

$$\psi_V(M^2) = \frac{\Gamma^V(M^2)}{M^2 - M_V^2}. \quad (2.62)$$

See Ref. [20] for its parameterization.

a)



b)

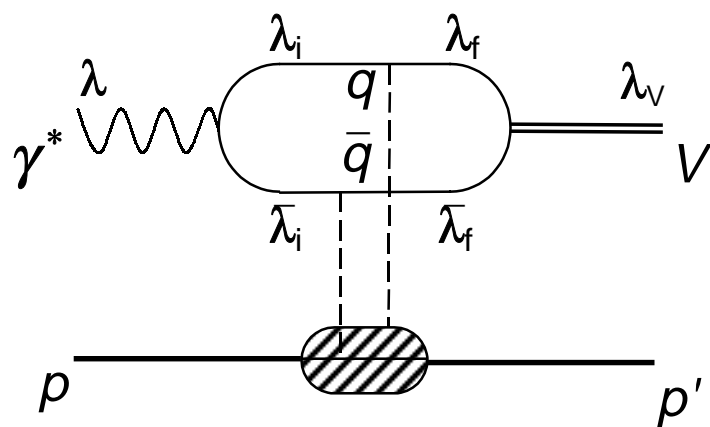


Fig.(2.3)-1

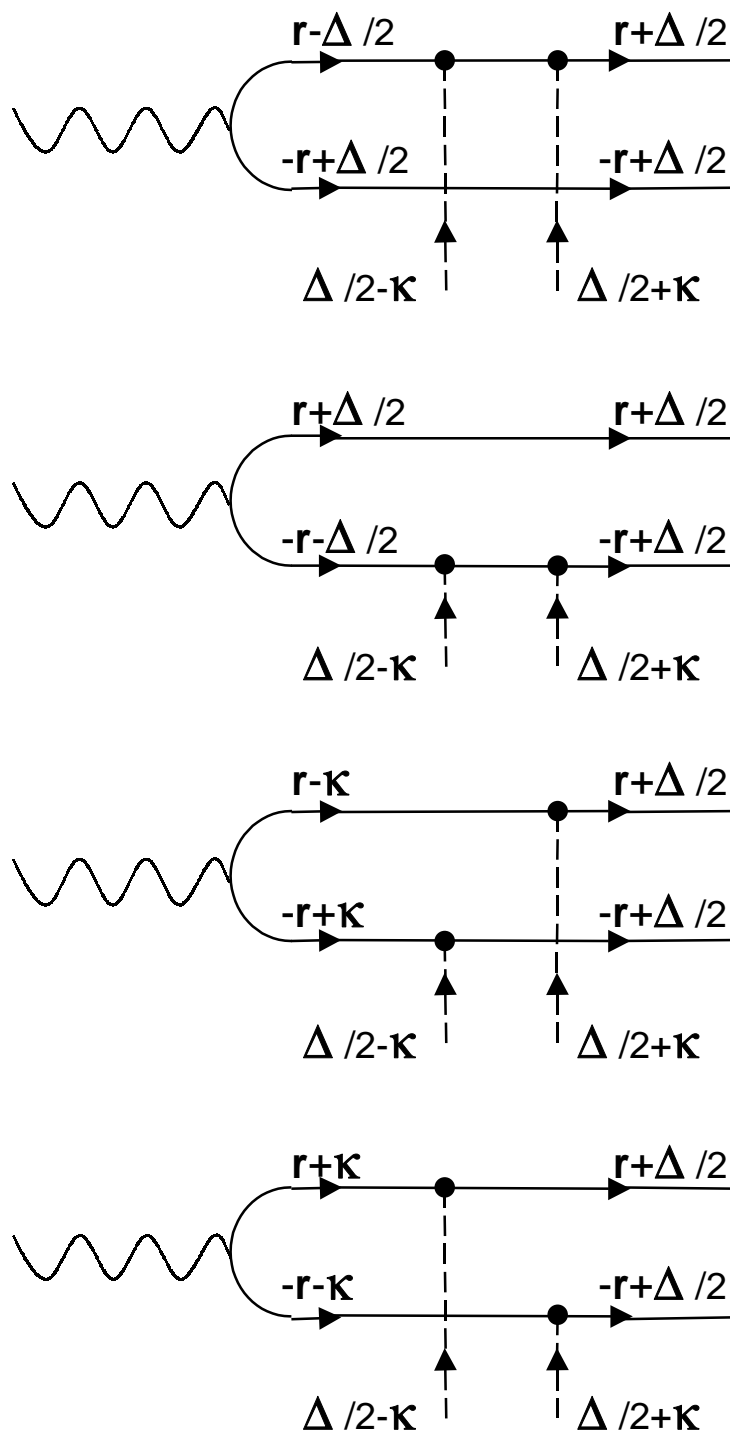


Fig.(2.3)-2

2.4 Diffractive excitation of continuum

We use unitarity to calculate the hadronic helicity tensor $H_{\lambda\lambda'}$ of the $\gamma_{\lambda}^* p \rightarrow \gamma_{\lambda'}^* p$ process (see Fig.(2.3)-1a) as a sum over the (anti)quark helicities λ_f and $\bar{\lambda}_f$ in the product of $\gamma_{\lambda}^* p \rightarrow (q_{\lambda_f} \bar{q}_{\bar{\lambda}_f}) p'$ and $\gamma_{\lambda'}^* p \rightarrow (q_{\lambda_f} \bar{q}_{\bar{\lambda}_f}) p'$ amplitudes:

$$H_{\lambda\lambda'} = \sum_{\lambda_f \bar{\lambda}_f} [A_{\lambda'; \lambda_f \bar{\lambda}_f}^D]^* A_{\lambda; \lambda_f \bar{\lambda}_f}^D. \quad (2.63)$$

Performing all intermediate particle momentum integrations (see Appendix A) and multiplying by all standard QCD factors, we obtain

$$\sigma_i^D = \frac{\alpha_{em}}{6\pi^2} \sum_f e_f^2 \int dz \int d^2\mathbf{k} \int d^2\Delta \alpha_s^2 H_i \quad (2.64)$$

for the components $i = T, L, TT', LT$ of the diffractive cross-sections in (2.29), where e_f is the charge of quark with flavor f , and α_s is the running QCD strong coupling constant (calculated at hardness scale \bar{Q}^2 , introduced below). We introduced the averaged contributions H_i , which correspond to the components of the cross-section σ_i^D , as

$$\begin{aligned} H_T &\equiv \frac{1}{2} \{(H_{++} + H_{--})\} \\ &= \{1 - 2z(1-z)\} \Phi_1^2 + m_f^2 \Phi_2^2, \end{aligned} \quad (2.65)$$

$$\begin{aligned} H_L &\equiv H_{LL} \\ &= 4z^2(1-z)^2 Q^2 \Phi_2^2, \end{aligned} \quad (2.66)$$

$$H_{TT'} \equiv \frac{1}{2} \{H_{+-} + H_{-+}\}$$

$$= 2z(1-z) \left[\Phi_1^2 - 2(\mathbf{e}\Phi_1)^2 \right], \quad (2.67)$$

$$\begin{aligned} H_{LT} &\equiv \frac{1}{4} \{H_{+L} + H_{L+} + H_{-L} + H_{L-}\} \\ &= 4z(1-z)(1-2z) Q(\mathbf{e}\Phi_1) \Phi_2, \end{aligned} \quad (2.68)$$

where the helicity tensor (2.63) components are calculated using (2.49-2.54):

$$H_{\pm\pm} = 2\{1 - 2z(1-z)\} (\mathbf{e}_\pm^* \Phi_1)(\mathbf{e}_\pm \Phi_1) + (\mathbf{e}_\pm^* \mathbf{e}_\pm) m_f^2 \Phi_2^2, \quad (2.69)$$

$$H_{\pm\mp} = 4z(1-z) (\mathbf{e}_\pm^* \Phi_1)(\mathbf{e}_\mp \Phi_1), \quad (2.70)$$

$$H_{\pm L} = H_{L\pm}^* = \pm 4\sqrt{2}z(1-z)(1-2z) Q(\mathbf{e}_\pm^* \Phi_1) \Phi_2. \quad (2.71)$$

For future discussion, we also introduce the helicity altering and conserving leading twist contributions to the transverse component

$$H_{T_0} = \Phi_1^2 \quad (2.72)$$

and

$$H_{T_1} = m_f^2 \Phi_2^2, \quad (2.73)$$

respectively, and the higher twist (as shown in Sec.3.3) contribution \hat{T}_0 to the transverse cross-section

$$H_{\hat{T}_0} = -2z(1-z) \Phi_1^2, \quad (2.74)$$

so in total:

$$H_T = H_{T_0} + H_{T_1} + H_{\hat{T}_0}. \quad (2.75)$$

In the above formulae \mathbf{e} is a unit transverse projection of the electron momentum which defines the azimuthal angle of the (e, e') plane. See Eqs. (2.22), (2.24) and (2.25). One can already see in Eqs. (2.67) and (2.67) that both TT' and LT interference components depend on the direction of \mathbf{e} and vanish if we integrate it out, leaving us with the transverse T and longitudinal L components, which were calculated in Refs. [3] and [6] for zero momentum transfer $\Delta = 0$.

To evaluate the helicity amplitudes Φ_i defined in Eq. (2.54), we follow Ref. [21] and approximate the off-forward gluon density by

$$f(x_{\mathbf{P}}, \boldsymbol{\kappa}, \boldsymbol{\Delta}) = \exp\left(-\frac{1}{2}B_{3\mathbf{P}}\Delta^2\right)f(x_{\mathbf{P}}, \kappa^2). \quad (2.76)$$

In Eq. (2.76) the dependence on $(\boldsymbol{\Delta}\boldsymbol{\kappa})$ can be neglected for small $x_{\mathbf{P}}$ as the subleading Balitskii-Fadin-Kuraev-Lipatov (BFKL) singularity [22]. We also parameterized the small- Δ^2 dependence by the universal diffractive slope $B_{3\mathbf{P}} \sim 6 \text{ GeV}^2$, which will be discussed in Sec.4.3.

To perform the gluon loop momentum $\boldsymbol{\kappa}$ integration in Eq. (2.54), we expand Eq. (2.50) in $\kappa^2 \lesssim \overline{Q}^2$, where

$$\overline{Q}^2 = k^2 + \varepsilon^2 \quad (2.77)$$

is the perturbative QCD scale from energy denominator (2.33), average over the $\boldsymbol{\kappa}$ orientation, and obtain

$$\langle\phi_1\rangle = \mathbf{r} \left[\frac{2\varepsilon^2}{(r^2 + \varepsilon^2)^3} \kappa^2 - \frac{1}{4} \frac{\Delta^2(r^2 + \varepsilon^2) - 4(\mathbf{r}\boldsymbol{\Delta})^2}{(r^2 + \varepsilon^2)^3} \right] - \frac{1}{2} \boldsymbol{\Delta} \frac{(\mathbf{r}\boldsymbol{\Delta})}{(r^2 + \varepsilon^2)^2} \quad (2.78)$$

and

$$\langle \phi_2 \rangle = \frac{\varepsilon^2 - r^2}{(r^2 + \varepsilon^2)^3} \kappa^2 - \frac{1}{4} \frac{\Delta^2(r^2 + \varepsilon^2) - 4(\mathbf{r}\Delta)^2}{(r^2 + \varepsilon^2)^3}. \quad (2.79)$$

We used the notation $\langle \phi_i \rangle \equiv \int d\theta \phi_i / (2\pi)$, where θ is an angle between $\boldsymbol{\kappa}$ and \mathbf{r} .

Then, we encounter two types of $d\kappa^2$ integrals in Eq. (2.54). The first one is the Leading Log Approximation (LLA) integral

$$G(x_{\mathbf{P}}, \overline{Q}^2) = \int^{\overline{Q}^2} \frac{d\kappa^2}{\kappa^4} f(x_{\mathbf{P}}, \kappa^2) \kappa^2, \quad (2.80)$$

which is the gluon structure function of the proton at the pQCD scale \overline{Q}^2 . The second integral is a soft gluon structure function

$$G(x_{\mathbf{P}}, \mu_G^2) = \mu_G^2 \int_{\mu_G^2} \frac{d\kappa^2}{\kappa^4} f(x_{\mathbf{P}}, \kappa^2), \quad (2.81)$$

where the integration converges for small κ with soft gluon momentum scale $\mu_G \sim 0.7 \text{ GeV}$.

We also define for future use an infrared parameter

$$b(x_{\mathbf{P}}, \mu_G^2, \overline{Q}^2) = \frac{G(x_{\mathbf{P}}, \mu_G^2)}{2\mu_G^2 G(x_{\mathbf{P}}, \overline{Q}^2)}, \quad (2.82)$$

which, at large \overline{Q}^2 , decreases only because of the scaling violations and stays substantial.

The next step is to expand Eqs. (2.78) and (2.79) in small Δ , up to terms $\propto \Delta^3$, and obtain for the helicity amplitudes (2.54) the following expressions:

$$\begin{aligned} \Phi_1 = & \left(1 - \frac{k^2}{\overline{Q}^2}\right) \left[2\mathbf{k} - (1 - 2z)\Delta + 6(1 - 2z) \frac{\mathbf{k}(\mathbf{k}\Delta)}{\overline{Q}^2} \right. \\ & \left. - \frac{3}{2}(1 - 2z)^2 \left\{ 2 \frac{\Delta(\mathbf{k}\Delta)}{\overline{Q}^2} + \frac{\mathbf{k}\Delta^2}{\overline{Q}^2} - 8 \frac{\mathbf{k}(\mathbf{k}\Delta)^2}{\overline{Q}^4} \right\} \right] \frac{G(x_{\mathbf{P}}, \overline{Q}^2)}{\overline{Q}^4} \end{aligned}$$

$$-\frac{1}{4} \left[2 \frac{\Delta(\mathbf{k}\Delta)}{Q^2} + \frac{\mathbf{k}\Delta^2}{Q^2} - 4 \frac{\mathbf{k}(\mathbf{k}\Delta)^2}{Q^4} \right] \frac{G(x_{\mathbf{P}}, \mu_G^2)}{\mu_G^2 Q^2} \quad (2.83)$$

and

$$\begin{aligned} \Phi_2 = & \left[1 - 2 \frac{k^2}{Q^2} + 4(1-2z) \frac{(\mathbf{k}\Delta)}{Q^2} - 6(1-2z) \frac{k^2(\mathbf{k}\Delta)}{Q^2} \right. \\ & \left. - \frac{1}{2}(1-2z)^2 \left\{ 2 \frac{\Delta^2}{Q^2} - 3 \frac{k^2 \Delta^2}{Q^4} - 18 \frac{(\mathbf{k}\Delta)^2}{Q^4} + 24 \frac{k^2(\mathbf{k}\Delta)^2}{Q^6} \right\} \right] \frac{G(x_{\mathbf{P}}, \bar{Q}^2)}{Q^4} \\ & - \frac{1}{4} \left[\frac{\Delta^2}{Q^2} - 4 \frac{(\mathbf{k}\Delta)^2}{Q^4} \right] \frac{G(x_{\mathbf{P}}, \mu_G^2)}{\mu_G^2 Q^2}. \end{aligned} \quad (2.84)$$

Next, we perform the quark loop-momentum integrations over z and k^2 in Eq. (2.64).

We use the invariant mass definition, Eq. (2.46), to eliminate the dk^2 integration. For the differential diffractive cross-sections with fixed invariant mass M^2 , we have

$$(2\pi)^2 \frac{d\sigma_i^D}{dM^2 d\Delta^2 d\phi d\varphi} = \frac{\alpha_{em}}{6} \sum_f e_f^2 \int_{z_-}^{z_+} dz \cdot z(1-z) \alpha_s^2 H_i, \quad (2.85)$$

where the longitudinal momentum integration is over the symmetric range with respect to $z = 1/2$,

$$z_{\pm} = \frac{1}{2} \left(1 \pm \sqrt{1 - \frac{4m_f^2}{M^2}} \right). \quad (2.86)$$

It is convenient to set the scale for invariant mass M^2 with the use of Q^2 and β

$$M^2 = Q^2 \frac{1 - \beta}{\beta}. \quad (2.87)$$

See (2.11). Then, we substitute the helicity amplitudes (2.83) and (2.83) into hadronic tensors (2.65-2.68) and perform the final dz integration in Eq. (2.85). To do this integration,

we change variables using the pQCD scale (2.77)

$$\bar{Q}^2 = \frac{k^2 + m_f^2}{1 - \beta} = \frac{z(1 - z)Q^2}{\beta}. \quad (2.88)$$

After lengthy, but simple calculations we get integrations in the form

$$\int_{\frac{m_f^2}{1-\beta}}^{\frac{Q^2}{4\beta}} \frac{d\bar{Q}^2}{\bar{Q}^{2n}} \left(1 - \frac{4\beta\bar{Q}^2}{Q^2}\right)^{-\frac{1}{2}} \left[\alpha_s(\bar{Q}^2)G(x_{\mathbf{P}}, \bar{Q}^2)\right]^m, \quad (2.89)$$

where $n = 1, 2 \dots 6$ and $m = 1, 2$, and the factor in the square brackets has weak logarithmic dependence on \bar{Q}^2 .

Integrals with $n = 1$ converge at the upper integration limit: the pQCD scale is

$$\bar{Q}_L^2 \sim \frac{Q^2}{4\beta}, \quad (2.90)$$

which corresponds to symmetrical $q\bar{q}$ pairs $z \sim 1/2$ and large transverse momentum $k^2 \sim M^2/4$. The lower integration limit of Eq. (2.89) contributes to the $n \geq 2$ integrals and yields the pQCD scale

$$\bar{Q}_T^2 \sim \frac{m_f^2}{1 - \beta}, \quad (2.91)$$

which corresponds to asymmetrical $q\bar{q}$ pairs with $z \sim m_f^2/M^2$ and small $k^2 \sim m_f^2$. For heavy flavors and/or sufficiently small $(1 - \beta)$, the pQCD scale \bar{Q}_T^2 is large and we remain in a perturbative domain.

We introduce the scaling violating functions of pQCD scales \bar{Q}_T^2 and \bar{Q}_L^2 , which, to the *log*-accuracy, are

$$\bar{G}_{T,L}^2 = \left[\alpha_s(\bar{Q}_{T,L}^2)G(x_{\mathbf{P}}, \bar{Q}_{T,L}^2)\right]^2. \quad (2.92)$$

Below we will also use the short-hand notation

$$b_{T,L} \equiv b(x_{\mathbf{P}}, \mu_G^2, \overline{Q}_{T,L}^2). \quad (2.93)$$

The final step is to expand our expressions for cross-section components σ_i in powers of m_f^2 , and retain the leading twist in each case. We present the results of the above calculations in the next chapter.

Chapter 3

Cross-sections

In this chapter, we present the results of analytical calculations of the diffractive cross-sections in the color-dipole approach. The transverse and longitudinal components were first calculated in Refs. [5], [6] in the zero momentum transfer $\Delta = 0$ limit for the diffractive excitation of continuum case. The evaluations of the vector meson diffractive production amplitudes were done in Refs. [23], [19]. The author's contribution is an analytical evaluation of non-zero momentum transfer, higher twist and azimuthal angle components of DDIS into continuum. The duality correspondence between s-channel helicity non-conserving cross-section components in low-mass continuum and vector meson diffractive excitation is established. We focus here on the azimuthal angle, twist, and gluon structure function dependence of the cross-section components.

3.1 Angular dependence

In this section we write down the result of calculations described in previous chapter. First, we introduce the azimuthal angles for DDIS as follows: φ - angle between \mathbf{k} and $\mathbf{\Delta}$, ψ - between \mathbf{k} and \mathbf{e} , ϕ - between $\mathbf{\Delta}$ and \mathbf{e} , so $\psi = \varphi - \phi$. In experiments, φ is measured as an angle between the proton (p, p') and the $q\bar{q}$ -jet planes and ϕ as an angle between the electron (e, e') and the proton (p, p') planes. See Fig.(2.1)-1b.

To the *log*-accuracy, for the differential DDIS cross-section

$$(2\pi)^2 (M^2 + Q^2) \frac{d\sigma_i^D}{dM^2 d\Delta^2 d\phi d\varphi} \equiv \sum_f \partial\sigma_{f,i}^{D(4)}, \quad (3.1)$$

we have (we suppress index f in $\partial\sigma_{f,i}^{D(n)}$ below, index (n) refers to the number of derivatives), using the results of previous chapter and universal short-hand factor

$$S_f = \frac{\pi^2 \alpha_{em} e_f^2}{18} \exp(-B_{3\mathbf{P}} \Delta^2), \quad (3.2)$$

the following expressions. The transverse cross-section is

$$\begin{aligned} \partial\sigma_T^{D(4)} &= S_f \frac{\beta(1-\beta)^2}{m_f^2 Q^2} \left[(1 - b_T \Delta^2) \cdot (3 + 4\beta + 8\beta^2) \right. \\ &\quad + \frac{\Delta^2}{m_f^2} \cdot \frac{1}{10} \left\{ (5 - 16\beta - 7\beta^2 - 78\beta^3 + 126\beta^4) \right. \\ &\quad \left. \left. + \cos(2\varphi) \cdot (1 - \beta) (25 - \beta - 18\beta^2 - 126\beta^3) \right\} \right. \\ &\quad \left. + b_T \Delta^2 \cdot \cos(2\varphi) \cdot 2\beta(1 - 4\beta) \right] \cdot \overline{G}_T^2. \end{aligned} \quad (3.3)$$

The longitudinal cross-section:

$$\begin{aligned}
\partial\sigma_L^{D(4)} &= S_f \frac{12\beta^3}{Q^4} \left[(1 - b_L \Delta^2) \cdot 2(1 - 2\beta)^2 \cdot \overline{G}_L^2 \right. \\
&\quad + \frac{\Delta^2}{m_f^2} \cdot (1 - \beta) \left\{ (1 - 7\beta + 23\beta^2 - 21\beta^3) \right. \\
&\quad \left. + \cos(2\varphi) \cdot (1 - \beta) (2 - 6\beta + 21\beta^2) \right\} \cdot \overline{G}_T^2 \\
&\quad \left. - b_L \Delta^2 \cdot \cos(2\varphi) \cdot 4(1 - \beta)(1 - 2\beta) \cdot \overline{G}_L^2 \right]. \tag{3.4}
\end{aligned}$$

The transverse-transverse interference cross-section:

$$\begin{aligned}
\partial\sigma_{TT'}^{D(4)} &= -S_f \frac{2\beta^2(1 - \beta)}{Q^4} \left[(1 - b_L \Delta^2) \cdot \cos(2\psi) \cdot 24\beta^2 \cdot \overline{G}_L^2 \right. \\
&\quad + \frac{\Delta^2}{m_f^2} \cdot \frac{1}{5} \left\{ -\cos(2\psi) \cdot 3(1 - \beta) (1 + 2\beta + 3\beta^2 + 84\beta^3) \right. \\
&\quad + 2\cos(2\psi) \cos(2\varphi) \cdot 21(1 - \beta)^2 (1 + 3\beta + 6\beta^2) \\
&\quad \left. - \cos(2\phi) \cdot 10(2 + 2\beta + 2\beta^2 - 9\beta^3) \right\} \cdot \overline{G}_T^2 \\
&\quad - b_L \Delta^2 \cdot 12\beta \{ \cos(2\phi) \\
&\quad \left. - 2\cos(2\psi) \cos(2\varphi) \cdot (1 - \beta) \} \cdot \overline{G}_L^2 \right]. \tag{3.5}
\end{aligned}$$

The longitudinal-transverse interference cross-section:

$$\begin{aligned}
\partial\sigma_{LT}^{D(4)} &= S_f \frac{\Delta}{Q} \frac{2\beta^2(1 - \beta)}{m_f^2 Q^2} \left[\{ -2\cos(\phi) \cdot (1 + \beta + 4\beta^2) \right. \\
&\quad \left. + 4\cos(\psi) \cos(\varphi) \cdot (1 - \beta) (1 + 2\beta + 18\beta^2) \right\} \\
&\quad - \frac{\Delta^2}{m_f^2} \cdot \frac{1}{10} (1 - \beta) \left\{ \cos(\phi) \cdot (11 + 7\beta + 3\beta^2 - 126\beta^3) \right. \\
&\quad \left. + 3\cos(\phi) \cos(2\varphi) \cdot (1 - \beta) (17 + 31\beta + 42\beta^2) \right\}
\end{aligned}$$

$$\begin{aligned}
& -3 \cos(\psi) \cos(\varphi) \cdot (1 - \beta) (8 + 15\beta + 21\beta^2 - 224\beta^3) \\
& -7 \cos(\psi) \cos(3\varphi) \cdot (1 - \beta)^2 (6 + 17\beta + 32\beta^2) \} \\
& + b_T \Delta^2 \{ \cos(\phi) \cdot (4 - 17\beta + 28\beta^2) \\
& + 3 \cos(\phi) \cos(2\varphi) \cdot (1 - \beta) (1 - 8\beta) \\
& - 6 \cos(\psi) \cos(\varphi) \cdot (1 - \beta) (1 - 5\beta + 18\beta^2) \\
& + 2 \cos(\psi) \cos(3\varphi) \cdot (1 - \beta)^2 (1 + 18\beta) \} \cdot \overline{G}_T^2. \tag{3.6}
\end{aligned}$$

These expressions are valid for $4m_f^2 \ll M^2, Q^2$; the case of low continuum mass $M^2 \sim 4m_f^2$ will be discussed separately. Below we discuss our results (3.3-3.6) in more details.

3.2 Helicity components

In this section, we split the cross-sections (3.3-3.6) into helicity components. We will discuss here only the azimuthal angle and twist content, leaving the rest of the discussion for subsequent sections. In general, twist- n means that the cross-section has a $1/Q^n$ dependence to *log*-accuracy. We will refer to (2.83) and (2.84) for properties of helicity amplitudes Φ_1 and Φ_2 which enter in cross-section components (2.85) as bi-products. See (2.65-2.68).

The leading twist-2 transverse cross-section is written in the form

$$\begin{aligned} \partial\sigma_T^{D(3)} &= S_f \frac{\beta(1-\beta)^2}{m_f^2 Q^2} \left[(1 - b_T \Delta^2) \cdot (3 + 4\beta + 8\beta^2) \right. \\ &\quad \left. + \frac{\Delta^2}{m_f^2} \cdot \frac{1}{10} (5 - 16\beta - 7\beta^2 - 78\beta^3 + 126\beta^4) \right] \cdot \overline{G}_T^2 \end{aligned} \quad (3.7)$$

and is a sum of helicity components: $\partial\sigma_T^{D(3)} = \partial\sigma_{T_0}^{D(3)} + \partial\sigma_{T_1}^{D(3)}$. See (2.72) and (2.73).

Helicity-violating amplitudes $\Phi_1 \propto \mathbf{k}$ in both vertices contribute to the component of the transverse cross-section T_0 with zero total helicity of the final quark and antiquark pair

$$\begin{aligned} \partial\sigma_{T_0}^{D(3)} &= S_f \frac{\beta(1-\beta)^2}{m_f^2 Q^2} \left[(1 - b_T \Delta^2) \cdot 2(1 + 2\beta + 3\beta^2) \right. \\ &\quad \left. + \frac{\Delta^2}{m_f^2} \cdot \frac{1}{10} (3 - 8\beta - 19\beta^2 - 30\beta^3 + 84\beta^4) \right] \cdot \overline{G}_T^2, \end{aligned} \quad (3.8)$$

and helicity conserving amplitudes $\Phi_2 \propto 1$ in both vertices contribute to the component T_1 with conservation of helicity at the $\gamma^* q\bar{q}$ vertex,

$$\partial\sigma_{T_1}^{D(3)} = S_f \frac{\beta(1-\beta)^2}{m_f^2 Q^2} \left[(1 - b_T \Delta^2) \cdot (1 + 2\beta^2) \right]$$

$$+\frac{\Delta^2}{m_f^2} \cdot \frac{1}{5} (1 - \beta) (1 - 3\beta + 3\beta^2 - 21\beta^3) \Big] \cdot \overline{G}_T^2. \quad (3.9)$$

Both T_0 and T_1 components give comparable twist-2 contributions at pQCD scale $\overline{Q}_T^2 \sim m_f^2/(1 - \beta)$. For light flavors and intermediate β , the typical range of gluon structure function variation μ_G^2 replaces smaller scale \overline{Q}_T^2 and (3.7-3.9) must not be taken literally. For heavy flavors and small $(1 - \beta)$ we are in legitimate pQCD domain and all results are valid within the approximations we have made. Gluon structure functions and pQCD scales will be discussed in more detail in Sec.4.4.

The longitudinal component is dominated by the helicity conserving amplitudes $\Phi_2 \propto 1$ in both vertices,

$$\begin{aligned} \partial\sigma_L^{D(3)} = & S_f \frac{12\beta^3}{Q^4} \left[(1 - b_L \Delta^2) \cdot 2(1 - 2\beta)^2 \cdot \overline{G}_L^2 \right. \\ & \left. + \frac{\Delta^2}{m_f^2} \cdot (1 - \beta) (1 - 7\beta + 23\beta^2 - 21\beta^3) \cdot \overline{G}_T^2 \right], \quad (3.10) \end{aligned}$$

which is twist-4, and the pQCD scale is hard, $\overline{Q}_L^2 \sim Q^2/4$ for large Q^2 . In comparison to the twist-2 transverse component, the L contribution lacks a small factor $(1 - \beta)^2$ for large β , and has a factor $G^2(x_{\mathbf{P}}, \overline{Q}_L^2)$ which dominates $G^2(x_{\mathbf{P}}, \overline{Q}_T^2)$ due to the scaling violating rise of the gluon structure function from scale \overline{Q}_T^2 to \overline{Q}_L^2 . Both these effects make the L contribution dominant for large β , and this is confirmed by numerical calculations in the next chapter.

Transverse-transverse interference has a contribution from the helicity-violating ampli-

tudes $\Phi_1 \propto \Delta$ in both vertices,

$$\begin{aligned} \partial\sigma_{TT'}^{D(3)} = & -S_f \frac{2\beta^2(1-\beta)}{Q^4} \left[-b_L \Delta^2 \cdot 12\beta^2 \cdot \overline{G}_L^2 \right. \\ & \left. + \frac{\Delta^2}{m_f^2} \cdot \frac{1}{5} (1 + \beta + \beta^2 - 99\beta^3 + 126\beta^4) \cdot \overline{G}_T^2 \right] \cdot \cos(2\phi), \end{aligned} \quad (3.11)$$

and has a standard interference factor $\Delta^2 \cos(2\phi)$. It is twist-4 with competition from the soft-hard contribution $\propto b_L G_L^2 \propto G(x_{\mathbf{P}}, \overline{Q}_L^2) G(x_{\mathbf{P}}, \mu_G^2) / \mu_G^2$, and from the semi-hard (for light flavors) contribution $\propto G^2(x_{\mathbf{P}}, \overline{Q}_T^2) / m_f^2$. For large β , the pQCD scale \overline{Q}_T rapidly increases and the second term in (3.11) becomes dominant.

The longitudinal-transverse interference with contributions from helicity amplitudes $\Phi_1 \propto \Delta$ and $\Phi_2 \propto 1$ is expressed by

$$\begin{aligned} \partial\sigma_{LT}^{D(3)} = & -S_f \frac{\Delta}{Q} \cdot \frac{2\beta^2(1-\beta)}{m_f^2 Q^2} \left[2(1 + \beta + 4\beta^2) \right. \\ & \left. - b_T \Delta^2 \cdot (4 - 17\beta + 28\beta^2) \right. \\ & \left. + \frac{\Delta^2}{m_f^2} \cdot \frac{1}{10} (1 - \beta) (11 + 7\beta + 3\beta^2 - 126\beta^3) \right] \cdot \overline{G}_T^2 \cdot \cos(\phi). \end{aligned} \quad (3.12)$$

The factor $\Delta \cos(\phi)$ reflects spin flip and one has twist-3 with pQCD scale \overline{Q}_T^2 , the same as for the transverse component (3.7). The importance of this term for pQCD scale separation will be discussed in more detail in the next chapter.

There are additional azimuthal angle contributions (denoted with *prime* below) which one can analyze, if the direction of \mathbf{k} , i.e. orientation of the $q\bar{q}$ plane, is reconstructed. It can be done, in principle, by a detailed study of the azimuthal configuration of the state

$X = q\bar{q}$. The transverse cross-section receives a contribution from the product of helicity violating amplitudes $\Phi_1 \propto \mathbf{k}$ and $\Phi_1 \propto \Delta(\mathbf{k}\Delta)$,

$$\begin{aligned} \partial\sigma_T^{D'(3)} &= S_f \frac{\beta(1-\beta)^2}{m_f^2 Q^2} \left[b_T \Delta^2 \cdot 2\beta(1-4\beta) \right. \\ &\quad \left. + \frac{\Delta^2}{10m_f^2} (1-\beta) (25 - \beta - 18\beta^2 - 126\beta^3) \right] \cdot \overline{G}_T^2 \cdot \cos(2\varphi), \end{aligned} \quad (3.13)$$

which is also twist-2 with pQCD scale \overline{Q}_T^2 , but has interference factor $\Delta^2 \cos(2\varphi)$ and contribution from the gluon structure function at both soft and hard scales $\propto b_T G_T^2 \propto G(x_{\mathbf{P}}, \overline{Q}_T^2) G(x_{\mathbf{P}}, \mu_G^2) / \mu_G^2$. One should notice a small factor $(1-\beta)$ in the contribution $\propto G^2(x_{\mathbf{P}}, \overline{Q}_T^2) / m_f^2$ and thus for large β the first term in (3.13) becomes dominant.

Similar factors are present in the twist-4 component of the longitudinal cross-section which comes from helicity amplitude $\Phi_2 \propto 1$ in one vertex and $\Phi_2 \propto (\mathbf{k}\Delta)^2$ in the other,

$$\begin{aligned} \partial\sigma_L^{D'(3)} &= S_f \frac{12\beta^3(1-\beta)}{Q^4} \left[-b_L \Delta^2 \cdot 4(1-2\beta) \cdot \overline{G}_L^2 \right. \\ &\quad \left. + \frac{\Delta^2}{m_f^2} (1-\beta) (2 - 6\beta + 21\beta^2) \cdot \overline{G}_T^2 \right] \cdot \cos(2\varphi), \end{aligned} \quad (3.14)$$

where the first term $\propto b_L G_L^2 \propto G(x_{\mathbf{P}}, \overline{Q}_L^2) G(x_{\mathbf{P}}, \mu_G^2) / \mu_G^2$ dominates the whole range of β due to a large pQCD scale \overline{Q}_L^2 in one of the gluon structure functions.

The transverse-transverse interference also receives contributions from amplitudes with $\Phi_1 \propto \mathbf{k}$ in both vertices,

$$\begin{aligned} \partial\sigma_{TT}^{D'(3)} &= -S_f \frac{4\beta^2(1-\beta)}{Q^4} \left[(1 - b_T \Delta^2) \cdot 12\beta^2 \cdot \overline{G}_L^2 \right. \\ &\quad \left. - \frac{\Delta^2}{m_f^2} \cdot \frac{3}{10} (1-\beta) (1 + 2\beta + 3\beta^2 + 84\beta^3) \cdot \overline{G}_T^2 \right] \cdot \cos(2\psi), \end{aligned} \quad (3.15)$$

and has a similar form as the longitudinal component multiplied by an interference factor $\cos(2\psi)$.

The longitudinal-transverse interference has an additional contribution from the product of helicity amplitudes $\Phi_1 \propto \mathbf{k}$ and $\Phi_2 \propto (\mathbf{k}\Delta)$,

$$\begin{aligned} \partial\sigma_{LT}^{D'(3)} &= S_f \frac{\Delta}{Q} \frac{2\beta^2(1-\beta)^2}{m_f^2 Q^2} \left[4(1+2\beta+18\beta^2) \right. \\ &\quad \left. + \frac{\Delta^2}{m_f^2} \cdot \frac{3}{10} (1-\beta)(8+15\beta+21\beta^2-224\beta^3) \right. \\ &\quad \left. - b_T \Delta^2 \cdot 6(1-5\beta+18\beta^2) \right] \cdot \overline{G}_T^2 \cdot \cos(\psi) \cos(\varphi). \end{aligned} \quad (3.16)$$

It is similar to (3.6), except for a different interference factor $\Delta \cos(\psi) \cos(\varphi)$. Both components (3.16) and (3.12) contribute to the LT interference cross-section, which when integrated over the jet plane direction \vec{k} (integrated over azimuthal angle φ with ϕ fixed) becomes,

$$\begin{aligned} \partial\sigma_{LT}^{D(3)} &= S_f \frac{\Delta}{Q} \cdot \frac{2\beta^2(1-\beta)}{m_f^2 Q^2} \left[12\beta^2(2-3\beta) \right. \\ &\quad \left. + b_T \Delta^2 \cdot (1+\beta-41\beta^2+54\beta^3) \right. \\ &\quad \left. + \frac{\Delta^2}{m_f^2} \cdot \frac{1}{20} (1-\beta)(2+7\beta+12\beta^2-483\beta^3+672\beta^4) \right] \cdot \overline{G}_T^2 \cdot \cos(\phi). \end{aligned} \quad (3.17)$$

3.3 Higher twist in transverse cross-section

For the portion of the transverse amplitude \hat{T}_0 defined in (2.74), the calculations indeed give the twist-4 contribution to the transverse cross-section

$$\begin{aligned} \partial\sigma_{\hat{T}_0}^{D(3)} = & -S_f \frac{4\beta^2(1-\beta)}{Q^4} \left[(1 - b_L \Delta^2) \cdot 12\beta^2 \cdot \overline{G}_L^2 \right. \\ & \left. + \frac{\Delta^2}{m_f^2} \cdot \frac{1}{10} (7 + 7\beta + 7\beta^2 - 243\beta^3 + 252\beta^4) \cdot \overline{G}_T^2 \right]. \end{aligned} \quad (3.18)$$

One can notice the similarity to the longitudinal term (3.10) with a large pQCD scale \overline{Q}_L^2 . Its only difference from the transverse-transverse interference contribution $\partial\sigma_{TT'}^{D'(3)}(\Delta = 0)$ is the lack of the azimuthal angle factor $\cos(2\psi)$. This general result holds for the case of $\Delta = 0$ in the *exact* formulae (2.67) and (2.74) and can be traced from (2.50) and (2.51).

There exists, though, a twist-4 correction to the T_0 part of the transverse amplitude, which cancels identically with the \hat{T}_0 part in the leading $\log \overline{Q}_L^2$ approximation and thus, one should take into account the next to leading $\log \overline{Q}_L^2$ terms to obtain the total twist-4 component of the transverse cross-section

$$\begin{aligned} \partial\sigma_{\hat{T}}^{D(3)} = & -S_f \frac{4\beta^2(1-\beta)}{Q^4} \left[(1 - \hat{b}_L \Delta^2) \cdot 12\beta^2 \cdot \hat{G}_L^2 \right. \\ & \left. - \frac{\Delta^2}{m_f^2} \cdot \frac{1}{10} (17 + 2\beta + 62\beta^2 - 588\beta^3 + 567\beta^4) \cdot \overline{G}_T^2 \right]. \end{aligned} \quad (3.19)$$

This twist-4 contribution contains the next to LLA term $\hat{G}_L^2 = \partial\overline{G}_L^2/\partial\log(\overline{Q}_L^2)$ due to cancellation of the LLA terms \overline{G}_L^2 . We also used the short-hand $\hat{b}_L \equiv b_L \overline{G}_L^2/\hat{G}_L^2$. One can still neglect terms \overline{G}_T^2 compared with \hat{G}_L^2 in the limit $\overline{Q}_T^2 \ll \overline{Q}_L^2$ for intermediate β . Unfortunately,

the full twist-4 contribution \hat{T} is not separable experimentally from the leading twist. Below we will omit the subscript (0) in the explicit twist-4 contribution \hat{T}_0 which one can measure using mentioned above identity to the interference term TT' (see more discussion in Chapter 4).

3.4 Hard scale

One can calculate the pQCD scale (2.88) averages using the cross-sections (2.85),

$$\langle \log(\overline{Q}^2) \rangle_j = \frac{\int dz \cdot z(1-z) \alpha_s^2(\overline{Q}^2) H_j(\overline{Q}^2) \log(\overline{Q}^2)}{\int dz \cdot z(1-z) \alpha_s^2(\overline{Q}^2) H_j(\overline{Q}^2)}. \quad (3.20)$$

For the transverse case, the result for the $\log(\overline{Q}^2)$ average reads

$$\langle \log(\overline{Q}^2) \rangle_T = \log\left(\frac{m_f^2}{1-\beta}\right) + \frac{9 + 20\beta + 88\beta^2}{6(3 + 4\beta + 8\beta^2)} \quad (3.21)$$

A similar expression can be deduced for the longitudinal-transverse case

$$\langle \log(\overline{Q}^2) \rangle_{LT} = \log\left(\frac{m_f^2}{1-\beta}\right) - \frac{1 + 7\beta - 71\beta^2 + 75\beta^3}{12\beta^2(2 - 3\beta)} \quad (3.22)$$

Additional β polynomials on the right-hand side of (3.21-3.22) are due to the fact that in both the T and LT cases integrations with different n in (2.89) contribute with different β dependence. Numerical calculations show the proximity and hardness of both scales, and are discussed in the next chapter.

3.5 Sum rule

We calculate cross-sections integrated over the continuum mass M^2 (see in (3.1) how differential cross-sections are defined) using the formula

$$\partial\sigma_i^{D(2)} = \int \frac{dM^2}{M^2 + Q^2} \partial\sigma_i^{D(3)} = \int \frac{d\beta}{\beta} \partial\sigma_i^{D(3)}. \quad (3.23)$$

If we fix the pQCD scale \overline{Q}^2 and perform a formal β integration from 0 to 1 we find

$$\partial\sigma_T^{D(2)} = \frac{8}{5} S_f \frac{(1 - b_T \Delta^2)}{m_f^2 Q^2} \cdot \overline{G}_T^2, \quad (3.24)$$

$$\partial\sigma_{T_0}^{D(2)} = \frac{6}{5} S_f \frac{(1 - b_T \Delta^2)}{m_f^2 Q^2} \cdot \overline{G}_T^2, \quad (3.25)$$

$$\partial\sigma_{T_1}^{D(2)} = \frac{2}{5} S_f \frac{(1 - b_T \Delta^2)}{m_f^2 Q^2} \cdot \overline{G}_T^2, \quad (3.26)$$

$$\partial\sigma_{\hat{T}}^{D(2)} = -\frac{12}{5} S_f \frac{(1 - b_L \Delta^2)}{Q^4} \cdot \overline{G}_L^2, \quad (3.27)$$

$$\partial\sigma_L^{D(2)} = \frac{16}{5} S_f \frac{(1 - b_L \Delta^2)}{Q^4} \cdot \overline{G}_L^2, \quad (3.28)$$

$$\partial\sigma_{TT'}^{D(2)} = \frac{6}{5} S_f \frac{b_L \Delta^2}{Q^4} \cdot \overline{G}_L^2 \cdot \cos(2\phi), \quad (3.29)$$

$$\partial\sigma_{LT}^{D(2)} = 0. \quad (3.30)$$

It is an important consequence of gauge invariance and unitarity that all terms $\propto \Delta^2/m_f^2$ in the cross-sections vanish identically. Invariant mass M^2 integration of cross-section components without angular dependence on the direction of \mathbf{k} allows us to restore the full and independent $d^2\mathbf{k}$ and dz integrations, as in (2.64). Then $d^2\mathbf{k}$ can be replaced by the $d^2\mathbf{r}$ integration if one assumes a k^2 -independent pQCD scale \overline{Q}^2 . Finally, one can notice that

in (2.50) only the first two terms can potentially contribute to leading-log \overline{Q}^2 components $\propto \Delta^2/m_f^2$, but with independence of variable \mathbf{r} there is, in fact, no Δ dependence left and terms $\propto \Delta^2/m_f^2$ vanish. This sum rule serves as a good check of the coefficients in the β polynomials.

The same analysis can be repeated for the LT term which vanishes upon $d\beta/\beta$ integration. This is due to the explicit asymmetrical $(1 - 2z)$ factor in (2.68) in case of independent \mathbf{r} variable. The symmetry of (2.50) with respect to $\boldsymbol{\kappa}$ and $\boldsymbol{\Delta}/2$ gives rise to $(1 - b\Delta^2)$ dependence and for $\partial\sigma_j^{D'(2)}$ cross-sections we have only relatively small correction equal to the infrared parameter $b_{T,L}$ in addition to the universal slope $B_{3\mathbf{P}}$.

The above sum rule does not work if we do not integrate out $d^2\mathbf{k}$ completely, as in the azimuthal angle components with fixed direction of \mathbf{k} :

$$\partial\sigma_T^{D'(2)} = S_f \frac{1}{10m_f^2 Q^2} \left(-b_T \Delta^2 + \frac{5\Delta^2}{m_f^2} \right) \overline{G}_T^2 \cdot \cos(2\varphi), \quad (3.31)$$

$$\partial\sigma_L^{D'(2)} = S_f \frac{4}{5m_f^2 Q^2} \left(b_L \Delta^2 \cdot \overline{G}_L^2 + \frac{17\Delta^2}{2m_f^2} \cdot \overline{G}_T^2 \right) \cdot \cos(2\varphi), \quad (3.32)$$

$$\partial\sigma_{TT'}^{D'(2)} = -S_f \frac{12}{5Q^4} \left[(1 - b_L \Delta^2) \cdot \overline{G}_L^2 - \frac{\Delta^2}{2m_f^2} \cdot \overline{G}_T^2 \right] \cdot \cos(2\psi), \quad (3.33)$$

$$\partial\sigma_{LT}^{D'(2)} = S_f \frac{\Delta}{Q} \frac{9}{5m_f^2 Q^2} \left(1 - b_T \Delta^2 \cdot \frac{13}{9} \right) \overline{G}_T^2 \cdot \cos(\psi) \cos(\varphi). \quad (3.34)$$

3.6 Low-mass excitation

The relative velocity of quarks in the $q\bar{q}$ pair is given by

$$v^2 = 1 - \frac{4m_f^2}{M^2}. \quad (3.35)$$

The kinematical threshold corresponds to $v = 0$, $M_{th}^2 = 4m_f^2$ and $\beta_{th} \approx 1 - 4m_f^2/Q^2$. In the region of $4m_f^2 \lesssim M^2 \ll Q^2$ we have small $v^2 = (\beta_{th} - \beta)Q^2/(4m_f^2)$, and it is convenient to use the velocity v instead of β , because of the longitudinal momentum phase space constraint

$$|1 - 2z| \leq v. \quad (3.36)$$

In the limit of $v \ll 1$, we have a large pQCD scale $\bar{Q}_{th}^2 = Q^2/4 \gg m_f^2$, and the following expressions for the leading twist, small Δ decomposition of helicity amplitudes

$$\Phi_1 = \frac{1}{\bar{Q}_{th}^4} \left\{ [2\mathbf{k} - (1 - 2z)\mathbf{\Delta}] G(x, \bar{Q}_{th}^2) - \frac{\mathbf{\Delta}(\mathbf{k}\mathbf{\Delta})}{2\mu_G^2} G(x, \mu_G^2) \right\} \exp(-\frac{1}{2}B_{3\mathbf{P}}\mathbf{\Delta}^2), \quad (3.37)$$

$$\Phi_2 = \frac{1}{\bar{Q}_{th}^4} \left\{ \left[1 - 4(1 - 2z)\frac{(\mathbf{k}\mathbf{\Delta})}{\bar{Q}^2} \right] G(x, \bar{Q}_{th}^2) + \frac{(\mathbf{k}\mathbf{\Delta})^2}{\bar{Q}_{th}^2\mu_G^2} G(x, \mu_G^2) \right\} \exp(-\frac{1}{2}B_{3\mathbf{P}}\mathbf{\Delta}^2), \quad (3.38)$$

where, according to (2.12) we substituted $x_{\mathbf{P}}$ with Bjorken x for $\beta \sim 1$.

In the close to threshold limit $v \ll 1$ we set a scale for M^2 using v instead of β , use the small transverse momentum of the (anti)quark $k^2 = m_f^2[v^2 - (1 - 2z)^2] \ll m_f^2$, perform z -integration and decompose in powers of v . Then, up to v^3 terms, the following results for cross-section components are obtained,

$$\partial\sigma_T^{D(3)} = 32S_f \frac{6m_f^2}{Q^6} v \left[(1 - b\Delta^2) + \frac{\Delta^2}{6m_f^2} v^2 \right] \cdot \bar{G}_{th}^2, \quad (3.39)$$

$$\partial\sigma_T^{D'(3)} = -32S_f \frac{4m_f^2}{Q^6} v^3 b \Delta^2 \cdot \overline{G}_{th}^2 \cdot \cos(2\varphi), \quad (3.40)$$

$$\partial\sigma_{T_0}^{D(3)} = 32S_f \frac{16m_f^2}{Q^6} v^3 \left[(1 - b\Delta^2) + \frac{\Delta^2}{8m_f^2} \right] \cdot \overline{G}_{th}^2, \quad (3.41)$$

$$\partial\sigma_{T_1}^{D(3)} = 32S_f \frac{6m_f^2}{Q^6} v (1 - b\Delta^2) \cdot \overline{G}_{th}^2, \quad (3.42)$$

$$\partial\sigma_{\hat{T}}^{D(3)} = -32S_f \frac{8m_f^2}{Q^6} v^3 \left[(1 - b\Delta^2) + \frac{\Delta^2}{8m_f^2} \right] \cdot \overline{G}_{th}^2, \quad (3.43)$$

$$\partial\sigma_L^{D(3)} = 32S_f \frac{3}{2Q^4} v (1 - b\Delta^2) \cdot \overline{G}_{th}^2, \quad (3.44)$$

$$\partial\sigma_L^{D'(3)} = 32S_f \frac{8m_f^2}{Q^6} v^3 b \Delta^2 \cdot \overline{G}_{th}^2 \cdot \cos(2\varphi), \quad (3.45)$$

$$\partial\sigma_{TT'}^{D(3)} = 32S_f \frac{4m_f^2}{Q^6} v^3 \left[b\Delta^2 - \frac{\Delta^2}{4m_f^2} \right] \cdot \overline{G}_{th}^2 \cdot \cos(2\phi), \quad (3.46)$$

$$\partial\sigma_{TT'}^{D'(3)} = -32S_f \frac{8m_f^2}{Q^6} v^3 (1 - b\Delta^2) \cdot \overline{G}_{th}^2 \cdot \cos(2\psi), \quad (3.47)$$

$$\partial\sigma_{LT}^{D(3)} = -32S_f \frac{\Delta}{Q} \frac{2}{Q^4} v^3 \left(1 - \frac{5}{4} b\Delta^2 \right) \cdot \overline{G}_{th}^2 \cdot \cos(\phi), \quad (3.48)$$

$$\partial\sigma_{LT}^{D'(3)} = 32S_f \frac{\Delta}{Q} \frac{224m_f^2}{5Q^6} v^5 (1 - b\Delta^2) \cdot \overline{G}_{th}^2 \cdot \cos(\psi) \cos(\varphi). \quad (3.49)$$

Notice that the pQCD scales \overline{Q}_T^2 and \overline{Q}_L^2 , defined in (2.91) and (2.90), coincide and are equal to $\overline{Q}_{th}^2 = Q^2/4$ in the limit of $\beta \sim 1$. We used for the threshold a short-hand notation $\overline{G}_{th}^2 = [\alpha_s(\overline{Q}_{th}^2)G(x_{\mathbf{P}}, \overline{Q}_{th}^2)]^2$. All the cross-sections vanish as $v \rightarrow 0$ at the threshold. The Δ^2 dependence of (3.39-3.48) describes the near-threshold behavior of the DDIS slopes, discussed in Sec.4.3. Cross-section components $\partial\sigma_T^{D'(3)}$ and $\partial\sigma_L^{D'(3)}$ receive leading twist contributions from the soft-hard contribution $\propto G(x_{\mathbf{P}}, \overline{Q}_{th}^2)G(x_{\mathbf{P}}, \mu_G^2)/\mu_G^2$ which comes from sub-leading $\log \overline{Q}^2$ terms in (3.38). These important contributions, which allow one to find the characteristic scale for soft gluons, have an analog in vector meson photoproduction,

discussed in the next section. A similar twist-4 term $\propto G(x_{\mathbf{P}}, \bar{Q}_{th}^2)G(x_{\mathbf{P}}, \mu_G^2)/\mu_G^2$ exists in the transverse-transverse interference cross-section component $\partial\sigma_{TT'}^{D(3)}$, but it is suppressed by the hard scale contribution $\propto G^2(x_{\mathbf{P}}, \bar{Q}_{th}^2)/m_f^2$ in (3.46). In the region close to the kinematical threshold, the longitudinal cross-section remains twist-4 (now the leading twist) and the transverse cross-section becomes of explicitly higher twist-6. In (3.7-3.17), one can already see how the transition from $1 - \beta \sim 1$ to $1 - \beta \sim M^2/Q^2$ for the increasing value of β changes the Q^2 dependence of corresponding components in the region close to the threshold.

The results for low-mass continuum excitation cross-section components will be used to establish the duality correspondence with the virtual photoproduction of vector mesons.

3.7 Vector meson production in DDIS

Using the same technique as for continuum excitation and following [23], for amplitudes of vector meson virtual photoproduction $\gamma^*p \rightarrow Vp'$ (dominant imaginary parts) we find

$$A(V_i\gamma_j) = is \frac{2C_V \sqrt{4\pi\alpha_{em}}}{\pi^2} \int dz \int d^2\mathbf{k} \alpha_s I(V_i\gamma_j) \frac{\psi_V(M^2)}{z(1-z)}, \quad (3.50)$$

where we projected a definite helicity $q_{\lambda_f}\bar{q}_{\bar{\lambda}_f}$ state onto the vector meson state V_{λ_V} with helicity $\lambda_V = 0, \pm 1$ and used the light-cone wave function $\psi_V(z, \mathbf{k}) \equiv \psi_V(M^2)$ (see (2.62) and [20] for its parameterization). In (3.50), $C_V = 1/\sqrt{2}, 1/(3\sqrt{2}), 1/3, 2/3$ are the charge-isospin factors for $V = \rho^0, \omega^0, \phi^0, J/\Psi$ production, respectively. We summed over (anti)quark helicities λ_f and $\bar{\lambda}_f$ in the products of $\gamma_{\lambda}^* q_{\lambda_f} \bar{q}_{\bar{\lambda}_f}$ and $V_{\lambda_V} q_{\lambda_f} \bar{q}_{\bar{\lambda}_f}$ amplitudes, $A_{\lambda; \lambda_f \bar{\lambda}_f}^D$ and $A_{\lambda_V; \lambda_f \bar{\lambda}_f}^V$ respectively, to get the unintegrated hadronic amplitude $I_{\lambda_V \lambda}$ (see also Fig.(2.3)-1b)

$$I_{\lambda_V \lambda} = \sum_{\lambda_f \bar{\lambda}_f} [A_{\lambda_V; \lambda_f \bar{\lambda}_f}^V]^* A_{\lambda; \lambda_f \bar{\lambda}_f}^D. \quad (3.51)$$

We define unintegrated hadronic amplitudes with explicit angular dependence as averages of helicity amplitudes $I_{\lambda_V \lambda}$

$$\begin{aligned} I(V_T\gamma_T) &\equiv \frac{1}{2} \{(I_{++} + I_{--})\} \\ &= \{1 - 2z(1-z)\} [(\mathbf{V}\mathbf{e})(\mathbf{k}\Phi_1) + (\mathbf{V}\mathbf{k})(\mathbf{e}\Phi_1) - (\mathbf{V}\Phi_1)(\mathbf{e}\mathbf{k})] + (\mathbf{V}\mathbf{e})m_f^2\Phi_2, \end{aligned} \quad (3.52)$$

$$\begin{aligned} I(V_T\gamma_{T'}) &\equiv \frac{1}{2} \{(I_{+-} + I_{-+})\} \\ &= 2z(1-z)[(\mathbf{V}\mathbf{e})(\mathbf{k}\Phi_1) - (\mathbf{V}\mathbf{k})(\mathbf{e}\Phi_1) - (\mathbf{V}\Phi_1)(\mathbf{e}\mathbf{k})], \end{aligned} \quad (3.53)$$

$$\begin{aligned}
I(V_L\gamma_L) &\equiv I_{LL} \\
&= -2z(1-z)Q\Phi_2 \cdot 2z(1-z)M,
\end{aligned} \tag{3.54}$$

$$\begin{aligned}
I(V_L\gamma_T) &\equiv \frac{1}{2}\{(I_{L+} + I_{L-})\} \\
&= (1-2z)(\mathbf{e}\Phi_1) \cdot 2z(1-z)M,
\end{aligned} \tag{3.55}$$

$$\begin{aligned}
I(V_T\gamma_L) &\equiv \frac{1}{2}\{(I_{+L} + I_{-L})\} \\
&= -2z(1-z)Q\Phi_2 \cdot (1-2z)(\mathbf{V}\mathbf{k}).
\end{aligned} \tag{3.56}$$

with helicity components

$$I_{\pm\pm} = 2\{1-2z(1-z)\}(\mathbf{V}_{\pm}^*\mathbf{k})(\mathbf{e}_{\pm}\Phi_1) + (\mathbf{V}_{\pm}^*\mathbf{e}_{\pm})m_f^2\Phi_2, \tag{3.57}$$

$$I_{\pm\mp} = 4z(1-z)(\mathbf{V}_{\pm}^*\mathbf{k})(\mathbf{e}_{\mp}\Phi_1), \tag{3.58}$$

$$I_{L\pm} = \pm\sqrt{2}(1-2z)(\mathbf{e}_{\pm}\Phi_1) \cdot 2z(1-z)M, \tag{3.59}$$

$$I_{\pm L} = \mp 2z(1-z)Q\Phi_2 \cdot \sqrt{2}(1-2z)(\mathbf{V}_{\pm}^*\mathbf{k}). \tag{3.60}$$

Like in the low-mass continuum excitation case, the transverse (anti)quark momentum $k^2 \lesssim R_V^{-2}$ is small, where R_V is the characteristic size of vector meson, coming from the light-cone wave-function ψ_V . The latter also limits the longitudinal momentum z -integration by

$$|1-2z| \lesssim v_M, \tag{3.61}$$

where $v_M^2 = 1 - 4m_f^2/M_V^2$ comes from the energy denominator in (2.62).

In the limit $M_V^2 \sim 4m_f^2 \ll Q^2$, the amplitudes $A_{ij} \equiv A(V_i\gamma_j)$, calculated first in [23], are

proportional to

$$A_{TT} \propto \frac{M_V^2}{Q^4} \overline{G}_{th} \cdot \cos(\psi'), \quad (3.62)$$

$$A'_{TT} \propto \frac{M_V^2}{Q^4} \overline{G}_{th} \cdot \cos(\psi'), \quad (3.63)$$

$$A_{TT'} \propto b\Delta^2 \cdot \frac{M_V^2}{Q^4} \overline{G}_{th} \cdot \{\cos(\psi') - 2\cos(\phi)\cos(\varphi')\}, \quad (3.64)$$

$$A_{LL} \propto \frac{M_V}{Q^3} \overline{G}_{th}, \quad (3.65)$$

$$A_{TL} \propto \frac{\Delta}{Q} \cdot \frac{M_V^2}{Q^4} \overline{G}_{th} \cdot \cos(\varphi'), \quad (3.66)$$

$$A_{LT} \propto \frac{\Delta}{Q} \cdot \frac{M_V}{Q^3} \overline{G}_{th} \cdot \cos(\phi), \quad (3.67)$$

where A_{TT} and A'_{TT} are transverse amplitudes with the same (opposite) intermediate quark helicities. In (3.62-3.67), the azimuthal angle ϕ is between Δ and \mathbf{e} , ψ' between \mathbf{V} and \mathbf{e} and $\varphi' \equiv \psi' - \phi$ between \mathbf{V} and Δ . The direction of vector meson polarization \mathbf{V} corresponds to that of \mathbf{k} in the final $q\bar{q}$ state of continuum excitation and is experimentally observed as the azimuthal angle of the plane of a $\pi^+\pi^-$ pair produced in the vector meson decay [24]. The double-helicity-flip amplitude $A(\gamma_T^* V_{T'})$ receives a leading twist contribution from the soft gluon structure function term $\propto (\Delta^2/\mu_G^2)G(x_{\mathbf{P}}, \mu_G^2)$ in Φ_1 in (3.38).

3.8 Duality

Bloom-Gilman duality [25] establishes the correspondence between scaling and resonance regimes in DIS. The pQCD evaluation [26] of helicity amplitudes at high Q^2 proves that the resonance contribution has the same Q^2 dependence as inelastic electron scattering off the proton. In DDIS, a similar duality relationship between semi-inclusive low-mass continuum excitation and exclusive vector meson production is established for transverse [28] and longitudinal [6] polarizations. Here we extend the duality correspondence to the s -channel helicity breaking DDIS. Using the approximate duality relationship

$$\int_{4m_f^2}^{M_V^2} dM^2 \frac{d\sigma_i^D(\gamma^* X)}{dM^2 d\Delta^2 d\phi d\varphi} = \frac{d\sigma_i^V(\gamma^* V)}{d\Delta^2 d\phi d\varphi} \equiv \partial\sigma_i^V \quad (3.68)$$

and $dM^2 = 4m_f^2 dv^2$ for $M^2 \sim M_V^2 \sim 4m_f^2 \ll Q^2$, in our case of small $v_M^2 = 1 - 4m_f^2/M_V^2$ we get the formulae

$$\partial\sigma_T^V = 32S_f \frac{16m_f^4}{Q^8} v_M^3 \left[(1 - b\Delta^2) + \frac{\Delta^2}{10m_f^2} v_M^2 \right] \cdot \overline{G}_{th}^2, \quad (3.69)$$

$$\partial\sigma_T^{V'} = -32S_f \frac{32m_f^4}{5Q^8} v_M^5 b\Delta^2 \cdot \overline{G}_{th}^2 \cdot \cos(2\varphi), \quad (3.70)$$

$$\partial\sigma_L^V = 32S_f \frac{4m_f^2}{Q^6} v_M^3 (1 - b\Delta^2) \cdot \overline{G}_{th}^2, \quad (3.71)$$

$$\partial\sigma_L^{V'} = 32S_f \frac{64m_f^4}{5Q^8} v_M^5 b\Delta^2 \cdot \overline{G}_{th}^2 \cdot \cos(2\varphi), \quad (3.72)$$

$$\partial\sigma_{LT}^V = -32S_f \frac{\Delta}{Q} \frac{16m_f^2}{5Q^6} v_M^5 \left(1 - \frac{5}{4}b\Delta^2 \right) \cdot \overline{G}_{th}^2 \cdot \cos(\phi), \quad (3.73)$$

$$\partial\sigma_{LT}^{V'} = 32S_f \frac{\Delta}{Q} \frac{256m_f^4}{5Q^8} v_M^7 (1 - b\Delta^2) \cdot \overline{G}_{th}^2 \cdot \cos(\psi) \cos(\varphi), \quad (3.74)$$

$$\partial\sigma_{TT'}^V = 32S_f \frac{32m_f^4}{5Q^8} v_M^5 \left[b\Delta^2 - \frac{\Delta^2}{4m_f^2} \right] \cdot \overline{G}_{th}^2 \cos(2\phi), \quad (3.75)$$

$$\partial\sigma_{TT'}^{V'} = -32S_f \frac{64m_f^4}{5Q^8} v_M^5 (1 - b\Delta^2) \cdot \overline{G}_{th}^2 \cos(2\psi). \quad (3.76)$$

We use the decay angular distribution written in the form (see [24])

$$\begin{aligned} W(\varphi, \phi) = & \frac{1}{4\pi} \left\{ [1 - 2r_{1-1}^{04} \cos(2\varphi)] \right. \\ & - \cos(2\phi) [(r_{00}^1 + 2r_{11}^1) - 2r_{1-1}^1 \cos(2\varphi)] - \sin(2\phi) [2\text{Im}(r_{1-1}^2) \sin(2\varphi)] \\ & \left. + 2\cos(\phi) [(r_{00}^5 + 2r_{11}^5) - 2r_{1-1}^5 \cos(2\varphi)] + 2\sin(\phi) [2\text{Im}(r_{1-1}^6) \sin(2\varphi)] \right\}, \quad (3.77) \end{aligned}$$

to find its matrix elements, expressed through amplitudes (3.62-3.67) and derived from the duality relation cross-sections (3.68-3.76). As shown below, in the leading twist approximation, these expressions have the same Q^2 , x , and Δ dependence

$$A_{LL}^* A_{LL} \propto \partial\sigma_L^V \propto \frac{M_V^2}{Q^6} G_{th}^2, \quad (3.78)$$

$$A_{TT}^* A_{TT} \propto \partial\sigma_T^V \propto \frac{M_V^4}{Q^8} G_{th}^2, \quad (3.79)$$

$$A_{TT'}^* A_{TT'}' \propto \partial\sigma_T^{V'} + \partial\sigma_L^{V'} \propto r_{1-1}^{04} \propto b\Delta^2 \cdot \frac{M_V^4}{Q^8} G_{th}^2, \quad (3.80)$$

$$A_{LT}^* A_{LT} \propto \partial\sigma_{TT'}^V \propto r_{00}^1 + 2r_{11}^1 \propto \frac{\Delta^2}{Q^2} \cdot \frac{M_V^2}{Q^6} G_{th}^2, \quad (3.81)$$

$$A_{TT'}^* A_{TT'}' \propto \partial\sigma_{TT'}^{V'} \propto r_{1-1}^1 \sim -\text{Im}(r_{1-1}^2) \propto \frac{M_V^4}{Q^8} G_{th}^2, \quad (3.82)$$

$$A_{LL}^* A_{LT} \propto \partial\sigma_{LT}^V \propto r_{00}^5 + 2r_{11}^5 \propto \frac{\Delta}{Q} \cdot \frac{M_V^4}{Q^8} G_{th}^2, \quad (3.83)$$

$$A_{TL}^* A_{TT} \propto \partial\sigma_{LT}^{V'} \propto r_{1-1}^5 \sim -\text{Im}(r_{1-1}^6) \propto \frac{\Delta}{Q} \cdot \frac{M_V^4}{Q^8} G_{th}^2. \quad (3.84)$$

By carefully analyzing the amplitudes for both the low-mass continuum and vector meson excitations, one can find that terms in the helicity amplitude $\Phi_{1,2}$ decompositions in (3.37)

and (3.38) match, and eventually this results in the same dependence on kinematical variables Q^2 , x , and Δ . The important question remains: what is the duality mass range? We are reminded here that the vector meson mass M_V^2 sets the upper limit of the integration in (3.68) and gives the scale for longitudinal momentum z -integration in (3.61) through the wave function ψ_V . In both cases, it enters through the velocity variable $v_M^2 = \delta M^2 / M_V^2$, where δM^2 has a meaning of characteristic mass-split in the excitation of the vector meson state, and this v_M^2 dependence is different in both cases and is affected by the parameterization of the vector meson wave function (see [23]).

Angular distributions for both cases are being measured using LPS, and preliminary data [24] confirm a substantial LT asymmetry effect in the excitation of ρ vector mesons.

Also the ordering

$$|r_{00}^5| > |r_{1-1}^1| > |r_{00}^1| > |r_{1-1}^{04}| > |r_{1-1}^5|, \quad (3.85)$$

which one can assume from (3.78-3.84), can be seen in [24], though the experimental errors in the last three matrix elements in (3.85) are of the order of the values themselves. Our numerical calculations of matrix elements r_{ij}^k and numerical tests of duality correspondence and duality range are in progress.

3.9 Impact parameter representation

Another equivalent, but more intuitive approach to calculate the M^2 -integrated diffractive cross-sections is to work in an impact parameter representation (transverse momenta are replaced with transverse sizes) in which the results are cast in quantum mechanical expectation form. See Ref. [4]. One can perform the Fourier transformation from transverse momentum \mathbf{r} to the transverse size of the $q\bar{q}$ pair $\boldsymbol{\rho}$ in (2.64) using the following identities

$$\int d^2\mathbf{r} \psi_i(\mathbf{r} + \mathbf{a}) \psi_i(\mathbf{r} + \mathbf{b}) \equiv \int d^2\boldsymbol{\rho} \varepsilon^{(2-i)^2} K_{2-i}^2(\varepsilon\rho) \cdot \cos \boldsymbol{\rho}(\mathbf{a} - \mathbf{b}), \quad (3.86)$$

$$\int d^2\mathbf{r} \mathbf{e} \psi_1(\mathbf{r} + \mathbf{a}) \cdot \mathbf{e} \psi_1(\mathbf{r} + \mathbf{b}) \equiv \int d^2\boldsymbol{\rho} \varepsilon^2 K_1^2(\varepsilon\rho) \cos^2(\psi) \cdot \cos \boldsymbol{\rho}(\mathbf{a} - \mathbf{b}), \quad (3.87)$$

$$\int d^2\mathbf{r} \mathbf{e} \psi_1(\mathbf{r} + \mathbf{a}) \cdot \psi_2(\mathbf{r} + \mathbf{b}) \equiv \int d^2\boldsymbol{\rho} \varepsilon K_1(\varepsilon\rho) K_0(\varepsilon\rho) \cos(\psi) \cdot \sin \boldsymbol{\rho}(\mathbf{a} - \mathbf{b}), \quad (3.88)$$

where $K_{0,1}$ are Bessel functions of imaginary argument and ψ is the angle between $\boldsymbol{\rho}$ and \mathbf{e} . While performing Fourier transformations (3.86-3.88) we neglected the \mathbf{k} -dependence of the pQCD scale, which is a main condition for the sum-rule discussed in Sec.3.5.

We get the following impact parameter representation of DDIS cross-sections

$$\sigma_j^D = \int dz \int d\boldsymbol{\rho} W_j(z, \boldsymbol{\rho}) \int d\boldsymbol{\Delta} \frac{\sigma^2(\boldsymbol{\rho}, \boldsymbol{\Delta})}{16\pi^2}, \quad j = T, L, TT', \quad (3.89)$$

$$\sigma_{LT}^D = 0. \quad (3.90)$$

When integrated over continuum mass M^2 , the longitudinal-transverse interference cross-section vanishes due to the sine function in (3.88), in compliance with the sum-rule (3.30).

We introduced in (3.89) the $q\bar{q}$ wave functions W_i [4] in the mixed $(z, \boldsymbol{\rho})$ representation

$$W_T(z, \boldsymbol{\rho}) = \frac{6\alpha_{em}}{(2\pi)^2} \sum_f e_f^2 \left\{ [1 - 2z(1-z)] \varepsilon^2 K_1^2(\varepsilon\rho) + m_f^2 K_0^2(\varepsilon\rho) \right\}, \quad (3.91)$$

$$W_L(z, \boldsymbol{\rho}) = \frac{6\alpha_{em}}{(2\pi)^2} \sum_f e_f^2 4z^2(1-z)^2 Q^2 K_0^2(\varepsilon\rho), \quad (3.92)$$

$$W_{TT'}(z, \boldsymbol{\rho}) = -\frac{6\alpha_{em}}{(2\pi)^2} \sum_f e_f^2 2z(1-z) \varepsilon^2 K_1^2(\varepsilon\rho) \cdot \cos(2\psi), \quad (3.93)$$

and the polarization, longitudinal momentum and Q^2 independent color-dipole cross-section

$$\sigma(\boldsymbol{\rho}, \boldsymbol{\Delta}) = \frac{16}{3} \int d\boldsymbol{\kappa} \cdot \alpha_s(\boldsymbol{\kappa}, \boldsymbol{\rho}) [\cos(\boldsymbol{\rho}\boldsymbol{\Delta}/2) - \cos(\boldsymbol{\rho}\boldsymbol{\kappa})] \frac{f(\boldsymbol{\kappa}, \boldsymbol{\Delta})}{\kappa^4}. \quad (3.94)$$

The physical interpretation of (3.89) is very straight-forward. It is the average of the color-dipole cross-section (3.94) over the wave function (3.91-3.93) of the $q\bar{q}$ pair in the mixed $(z, \boldsymbol{\rho})$ representation. This interpretation is possible due to the large life-time of the $q\bar{q}$ fluctuations $\tau \sim 1/(xm_p) > R_p$ at small Bjorken x (R_p is the characteristic size of proton).

In the limit of a small momentum transfer Δ and small dipole size $\rho^2 \ll 1/\mu_G^2$, the color dipole cross-section can be estimated as

$$\sigma(\boldsymbol{\rho}, \boldsymbol{\Delta}) = \frac{\pi^2}{3} \rho^2 \alpha_s(\kappa_\rho^2) G(x, \kappa_\rho^2) \exp\left(-\frac{1}{2} B_{3\mathbb{P}} \Delta^2\right) \cdot [1 - b\Delta^2 \cos^2(\varphi)], \quad (3.95)$$

where φ is the angle between $\boldsymbol{\rho}$ and $\boldsymbol{\Delta}$. The step-function approximation $4[1 - J_0(\kappa\rho)]/(\kappa\rho)^2 \approx \theta(C_0 - \kappa\rho)$ determines the constant $C_0 \approx 10$ in $\kappa_\rho^2 \sim C_0/\rho^2$. See Ref. [20]. The distance $1/\mu_G$ has the meaning of the propagation radius of the color gluon field.

For large-size dipoles $\rho^2 \gtrsim 1/\mu_G^2$ we get a saturation (independence of $\boldsymbol{\rho}$):

$$\sigma(\boldsymbol{\rho}, \boldsymbol{\Delta}) = \frac{4\pi^2}{3} \exp\left(-\frac{1}{2} B_{3\mathbb{P}} \Delta^2\right) \int \frac{d\kappa^2}{\kappa^4} \alpha_s(\kappa^2) \frac{\partial G(x, \kappa^2)}{\partial \log(\kappa^2)} \quad (3.96)$$

Using (3.95), together with relationship $(\varepsilon\rho)^n K_n(\varepsilon\rho) \propto \exp(-\varepsilon\rho)$, $n = 0, 1$, we find that the $d\rho^2$ integration in (3.89) converges at $\rho^2 \sim 1/\varepsilon^2$ and the remaining dz integrals have the form

$$\int dz \frac{[z(1-z)]^n}{\varepsilon^{2m}} G(x, C_0\varepsilon^2), \quad (3.97)$$

where $n = 0, 1, 2$ and $m = 2, 3$. Introduced in (2.52), $\varepsilon^2 = m_f^2 + z(1-z)Q^2$ defines hard scales $\overline{Q}_T^2 \sim C_0 m_f^2$ for asymmetric $z \sim m_f^2/Q^2$ pairs with large transverse size $\rho^2 \sim 1/m_f^2$, and $\overline{Q}_L^2 \sim C_0 Q^2/4$ for symmetric $z \sim 1/2$ pairs with small transverse size $\rho^2 \sim 1/Q^2$. After the dz integrations, which converge either for $z \sim m_f^2/Q^2$ or $z \sim 1/2$, we recover the results of (3.24-3.30). Asymmetric, large transverse size dipoles dominate in the transverse cross-section and produce twist-2 term $\propto \overline{G}_T^2/m_f^2 Q^2$. Symmetric, small transverse size pairs give, for L , \hat{T} and TT' cross-sections, the twist-4 contribution $\propto \overline{G}_L^2/Q^4$.

For the twist-4 component \hat{T} , we use dipole wave functions (3.91) and the symmetric pair $z \sim 1/2$ region of z integration, as opposed to the asymmetric $z \sim m_f^2/Q^2$ leading twist contribution the in transverse cross-section. Again, one can see that the term $\propto \overline{G}_L^2/Q^4$ vanishes due to the factor $[1 - 2z(1-z)]$ in (3.91); and we are left with the next to LLA term $\propto \hat{G}_L^2/Q^4$ (see also Sec.3.4).

For the imaginary parts of the vector meson production amplitudes, using calculations similar to those discussed above, we have the result

$$A(V_i \gamma_j^*) = \int dz \int d\boldsymbol{\rho} W_{ij}^V(z, \boldsymbol{\rho}) \sigma(\boldsymbol{\rho}, \boldsymbol{\Delta}), \quad (3.98)$$

where

$$W_{TT}^V(z, \boldsymbol{\rho}) = \frac{3C_V \sqrt{4\pi\alpha_{em}}}{(2\pi)^2} \cdot \left\{ [1 - 2z(1-z)] \varepsilon K_1(\varepsilon\rho) (-\partial_\rho) + m_f^2 K_0(\varepsilon\rho) \right\} \\ \times \psi_V(z, \boldsymbol{\rho}) \cos(\varphi'), \quad (3.99)$$

$$W_{LL}^V(z, \boldsymbol{\rho}) = \frac{3C_V \sqrt{4\pi\alpha_{em}}}{(2\pi)^2} \cdot 4QMz^2(1-z)^2 K_0(\varepsilon\rho) \\ \times \psi_V(z, \boldsymbol{\rho}), \quad (3.100)$$

$$W_{TT'}^V(z, \boldsymbol{\rho}) = -\frac{3C_V \sqrt{4\pi\alpha_{em}}}{(2\pi)^2} \cdot 2z(1-z) \varepsilon K_1(\varepsilon\rho) (-\partial_\rho) \\ \times \psi_V(z, \boldsymbol{\rho}) \{ \cos(\varphi') - 2 \cos(\psi) \cos(\phi') \}, \quad (3.101)$$

and the azimuthal angles are: φ' - between \mathbf{V} and \mathbf{e} , ψ - between $\boldsymbol{\rho}$ and \mathbf{e} , and ϕ' - between $\boldsymbol{\rho}$ and \mathbf{V} . The amplitudes for LT and TL interferences are zero due to the sine in (3.88) and the odd factor $(1 - 2z)$, which is not surprising in view of the sum-rule in Sec.3.4. After integration over the $\boldsymbol{\rho}$ direction, only the term $\cos(\boldsymbol{\rho}\boldsymbol{\Delta}/2)$ in the dipole cross-section (3.94) contributes and one recovers the result of (3.64) with the soft gluon structure function $G(x_{\mathbf{P}}, \mu_G)$.

Chapter 4

Numerical calculations

In this chapter, the results of the numerical calculations of the diffractive structure functions, azimuthal asymmetries and diffractive slopes, done by the author with the use of gluon structure function parameterizations, are presented. We discuss the agreement with the analytical results of previous chapter and show how these observables can be used to extract information on the structure of the proton.

4.1 Structure functions

It is convenient to define first the Δ and azimuthal angle independent structure functions using

$$\partial\sigma_{f,j}^{D(3)}(\Delta=0) \equiv \frac{4\pi^2\alpha_{em}}{Q^2} F_{f,j}^D, \quad j = T, \hat{T}, L, \quad (4.1)$$

$$\partial\sigma_{f,TT'}^{D'(3)}(\Delta=0) \equiv \frac{4\pi^2\alpha_{em}}{Q^2} F_{f,TT'}^D \cdot \cos(2\psi), \quad (4.2)$$

$$\partial\sigma_{f,LT}^{D(3)}(\Delta=0) \equiv \frac{4\pi^2\alpha_{em}}{Q^2} F_{f,LT}^D \cdot \frac{\Delta}{Q} \cos(\phi). \quad (4.3)$$

We perform numerical calculations for the TT' interference term $\propto \cos(2\psi)$, which is important for higher-twist separation, see below. Using (3.7), (3.10), (3.15) and (3.17), for the structure functions defined above, we find

$$F_{f,T}^D = \frac{e_f^2}{72m_f^2} \beta (1-\beta)^2 (3+4\beta+8\beta^2) \overline{G}_T^2, \quad (4.4)$$

$$F_{f,L}^D = \frac{e_f^2}{3Q^2} \beta^3 (1-2\beta)^2 \overline{G}_L^2, \quad (4.5)$$

$$F_{f,LT}^D = \frac{e_f^2}{3m_f^2} \beta^4 (1-\beta)(2-3\beta) \overline{G}_T^2, \quad (4.6)$$

$$F_{f,j}^D = -\frac{2e_f^2}{3Q^2} \beta^4 (1-\beta) \overline{G}_L^2, \quad j = \hat{T}, TT'. \quad (4.7)$$

For standard dimensionless Δ -dependent structure functions the following expressions can be adopted

$$F_j^{D(4)}(\Delta) = \frac{16\pi}{\sigma_{pp}^{tot}} \sum_f F_{f,j}^D \exp(-B_{f,j}\Delta^2), \quad j = T, L, \hat{T}, TT', \quad (4.8)$$

$$F_{LT}^{D(4)}(\Delta) = \frac{\Delta}{Q} \frac{16\pi}{\sigma_{pp}^{tot}} \sum_f F_{f,LT}^D \exp(-B_{f,LT}\Delta^2). \quad (4.9)$$

For conventional dimensionless Δ -integrated structure functions we have

$$F_j^{D(3)} = \sum_f \frac{F_{f,j}^D}{B_{f,j}}, \quad j = T, L, \hat{T}, TT', \quad (4.10)$$

$$F_{LT}^{D(3)} = \sum_f \frac{\langle \Delta \rangle_{f,LT}}{Q} \frac{F_{f,LT}^D}{B_{f,LT}}, \quad (4.11)$$

where $\langle \Delta \rangle_{f,LT} = \sqrt{\pi/(4B_{f,LT})}$. The diffractive slopes $B_{f,i}$ are explicitly written in Sec.4.3.

The results of numerical calculations are shown in Fig.(4.1)-1÷12. The transverse structure function $F_T^{D(4)}(\Delta = 0)$, as a function of β in Fig.(4.1)-1, reflects all the features of (4.4). It strongly depends on flavor due to the factor $1/m_f^2$, so heavy flavors are suppressed. The falloff for $\beta \rightarrow 1$ is quite strong due to the factor $(1 - \beta)^2$. The Δ -integrated structure function $F_T^{D(3)}$ has basically the same shape, see Fig.(4.1)-2, the only difference is its behavior for large β , which is affected by a nontrivial falloff of the diffractive slope $B_{f,T}$ for dominant light flavors. Separation of the transverse component from its longitudinal counterpart is discussed in Sec.4.2. The Q^2 -dependence of $F_T^{D(3)}$ is shown in Fig.(4.1)-3 for $\beta = 0.95$. It is almost flat, which is due to the absence of Q^2 -dependence in (4.4) for large Q^2 .

The transverse-transverse interference differs from the higher twist component in the transverse cross-section only by the interference factor $\cos(2\psi)$, which allows one to separate it experimentally if orientation of the jet plane \mathbf{k} is reconstructed. The structure function $F_{TT'}^{D(4)}(\Delta = 0) = F_{\hat{T}}^{D(4)}(\Delta = 0)$ is shown in Fig.(4.1)-4. The flavor dependence is weaker than the leading-twist transverse contribution due to the absence of explicit quark mass m_f^2 in (4.7). Still, light flavors dominate due to the broad range of $\log \overline{Q}^2$ integration which

contributes in (2.89) with $n = 1$. The falloff towards large β is almost a straight line due to the presence of the $(1 - \beta)$ factor. As shown in Sec.4.3, the diffractive slope $B_{f,TT'}$ is almost constant (the same is true for $B_{f,\hat{T}} \approx B_{f,TT'}$), and $F_{TT'}^{D(3)} \approx F_{\hat{T}}^{D(3)}$ is shown in Fig.(4.1)-5. The twist-4 factor $1/Q^2$ in TT' and \hat{T} structure functions results in their decrease for large Q^2 , and $F_{TT'}^{D(3)} \approx F_{\hat{T}}^{D(3)}$ is shown in Fig.(4.1)-6 as a function of Q^2 for $\beta = 0.95$. This decrease is slower than $1/Q^2$ due to the growing pQCD factor $\alpha_s^2(\overline{Q}_L^2)G^2(x_{\mathbf{P}}, \overline{Q}_L^2)$, which rises logarithmically with $\overline{Q}_L^2 \sim Q^2/(4\beta)$.

The longitudinal structure functions $F_L^{D(4)}(\Delta = 0)$ and $F_L^{D(3)}$ are shown in Fig.(4.1)-7 and Fig.(4.1)-8, respectively. For both graphs the shape is almost the same due to $B_{f,L}$ being constant away from $\beta \sim 1/2$, where the structure function $F_L^{D(4)}(\Delta = 0)$ is small due to the factor $(1 - 2\beta)^2$ in (4.5). The lack of the factor $(1 - \beta)$ makes the longitudinal cross-section relatively large for large β , and it falls towards the threshold only due to phase-space contraction (see (3.44) and discussion in Sec.3.6). Its flavor dependence is not strong due to the same reasons as in the TT' case. The Q^2 dependence, shown in Fig.(4.1)-9, resembles that of $F_{TT'}^{D(3)}$ due to the same twist-4 factor \overline{G}_L^2/Q^2 .

We show the longitudinal-transverse interference structure function $F_{LT}^{D(4)}(\Delta) \cdot Q/\Delta$ for $\Delta \rightarrow 0$ and the Δ -integrated structure function $F_{LT}^{D(3)}$ in Fig.(4.1)-10, and Fig.(4.1)-11, respectively. Both have a characteristic zero at $\beta \sim 2/3$ due to the factor $(2 - 3\beta)$ in (4.7). Light flavors dominate due to the same reason as in the transverse case. The falloff towards the β threshold is $\propto (1 - \beta)$ with some \log -influence due to the factor $\alpha_s^2(\overline{Q}_T^2)G^2(x_{\mathbf{P}}, \overline{Q}_T^2)$

with $\overline{Q}_T^2 \sim m_f^2/(1-\beta)$. The shape is almost the same for both graphs. The slight difference is due to an increase of the slope $B_{f,LT}$ for $\beta \sim 1/2$. The dependence of $F_{LT}^{D(3)}$ on Q^2 for $\beta = 0.95$ is shown in Fig.(4.1)-12. It has twist-3 falloff $\propto 1/Q$ towards large Q^2 .

The structure functions $F_i^{D(3)}$, $i = T, L, \hat{T}$, which survive azimuthal angle averaging, are shown in Fig.(4.1)-13 and Fig.(4.1)-14 as functions of β and Q^2 , respectively. One can see that for large β the longitudinal contribution dominates, and we will discuss this important result of a large L/T ratio in more detail in the next section. We emphasize the importance of the twist-4 \hat{T} component which was pointed out in Ref. [8]. Here we show two graphs from Ref. [8] which illustrate the twist-4 contribution to the total structure function $F_2^{D(3)} = F_T^{D(3)} + F_L^{D(3)}$. In Fig.(4.1)-15 we show the Q^2 -dependence of various components for $\beta = 0.65$ and $\beta = 0.9$. The twist-4 contributions from transverse and longitudinal structure functions almost cancel each other for $\beta = 0.65$ and this effect is important for comparison with the experimental data from the H1 collaboration [27]. More details on the L/\hat{T} ratio are given in Sec.4.2.

The $x_{\mathbf{P}}$ dependence of $F_2^{D(3)}$ for $\beta = 0.65$ and $\beta = 0.9$, and for different Q^2 is shown in Fig.(4.1)-16 in comparison with H1 experimental data [27] which are reproduced rather well over the whole range of Q^2 and $x_{\mathbf{P}}$. One should keep in mind, though, that $\beta = 0.9$, $Q^2 \lesssim 20 GeV^2$ correspond to continuum mass $M^2 \lesssim 3 GeV^2$, small enough to be influenced by exclusive vector meson excitation.

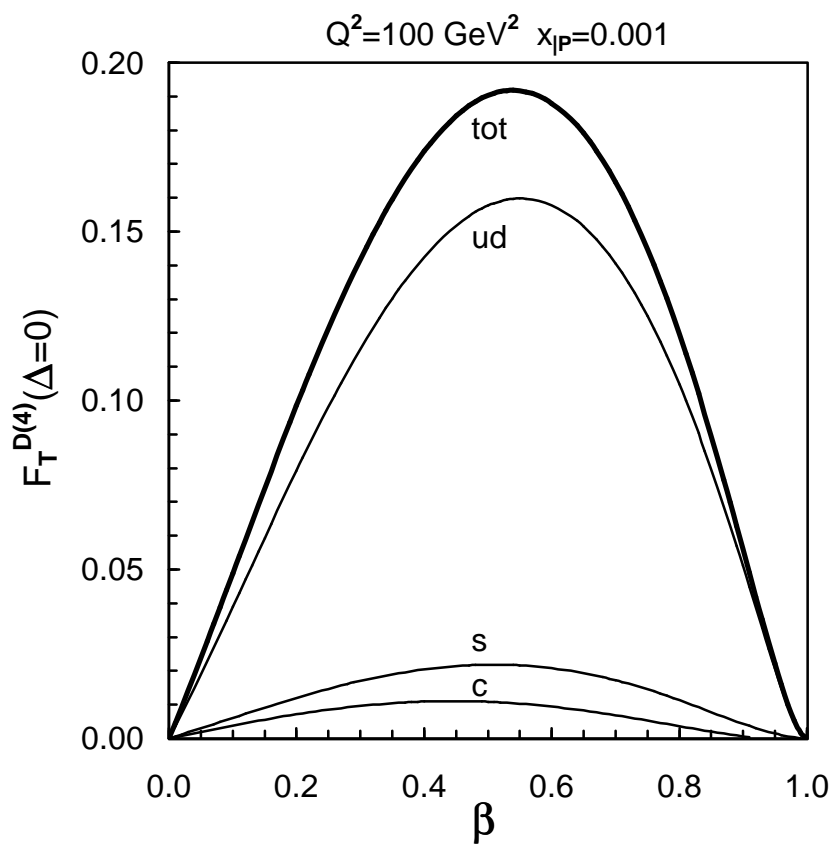


Fig.(4.1)-1

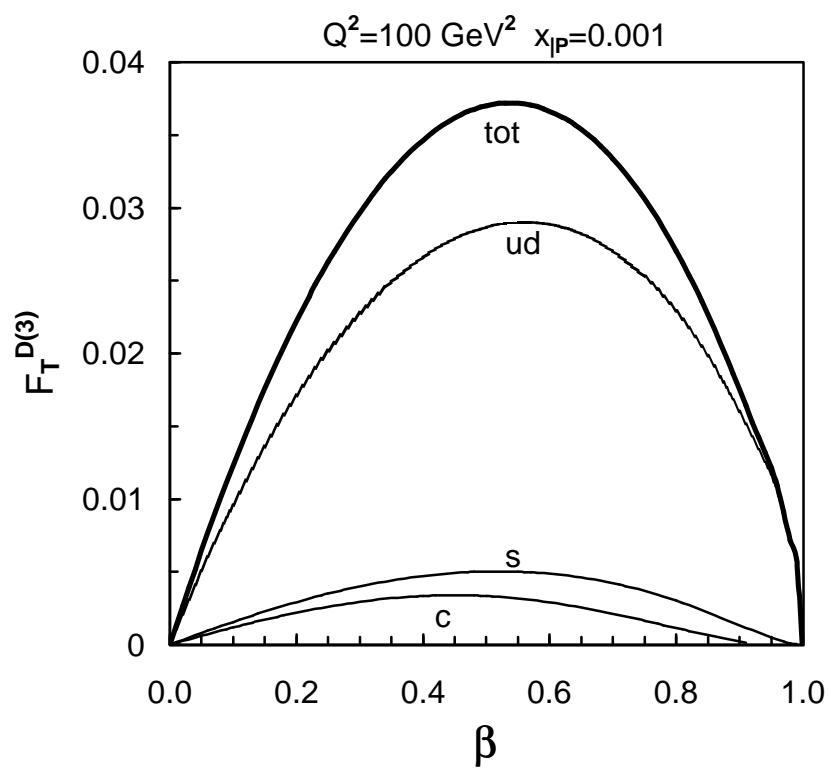


Fig.(4.1)-2

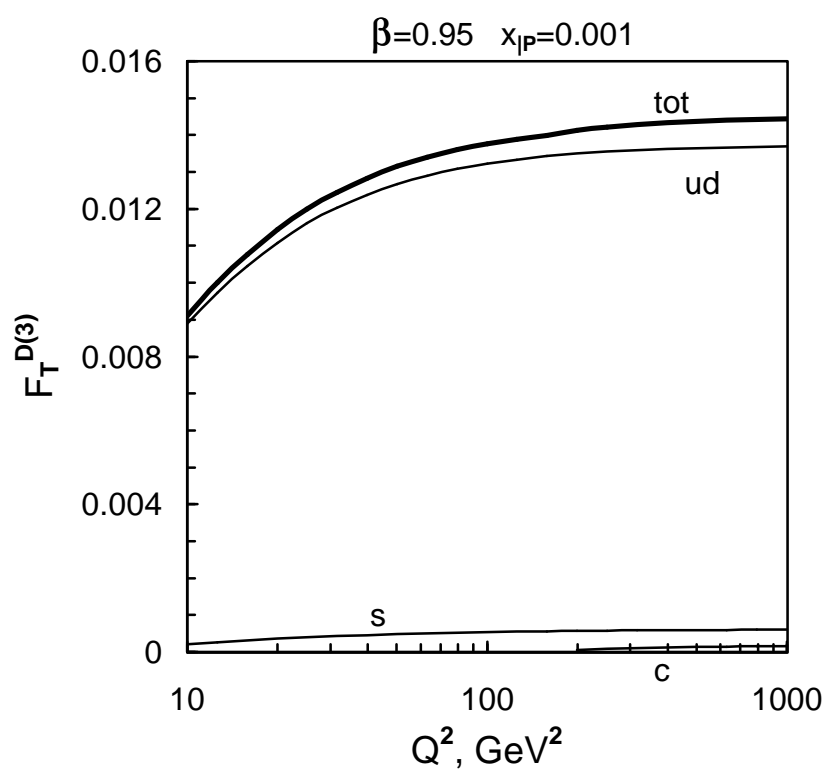


Fig.(4.1)-3

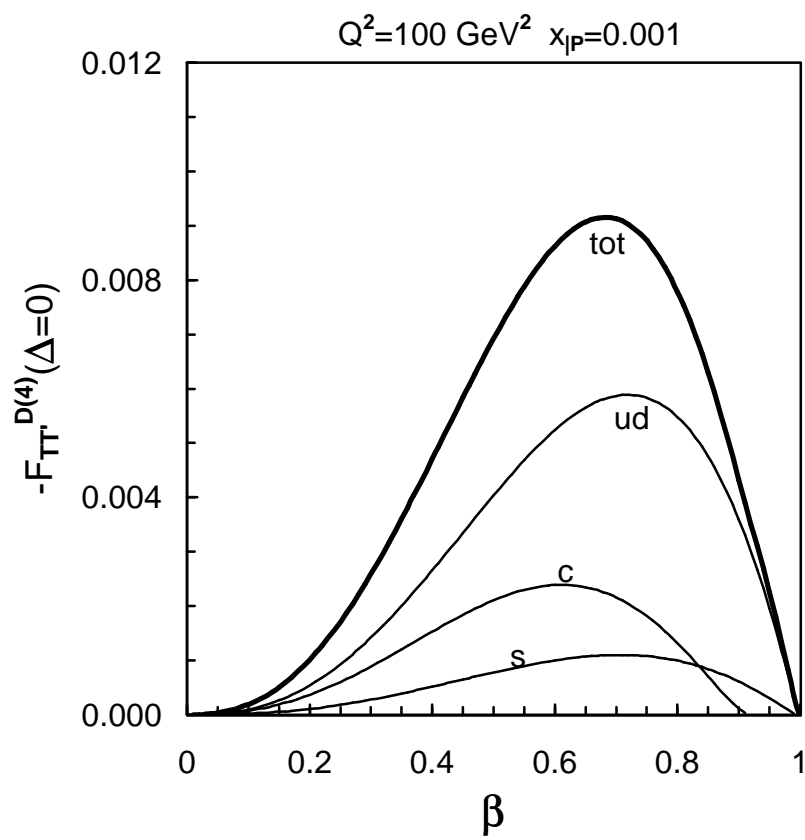


Fig.(4.1)-4

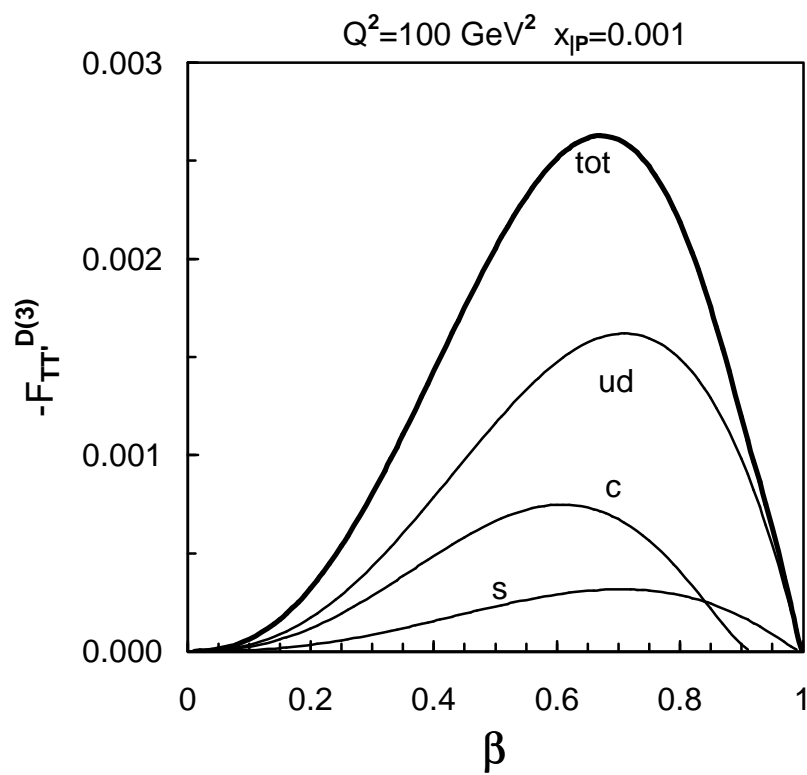


Fig.(4.1)-5

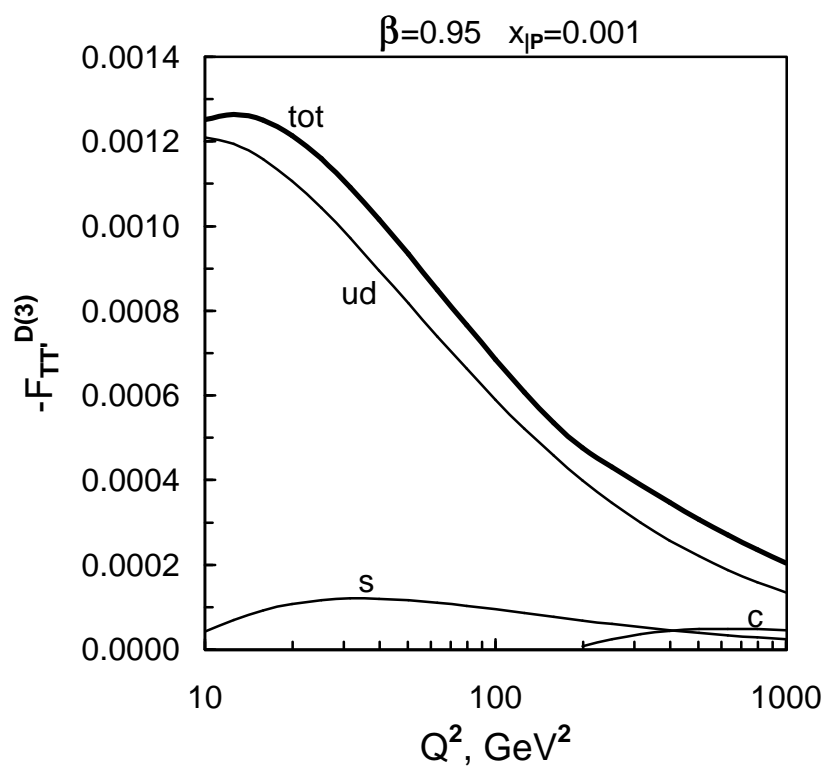


Fig.(4.1)-6

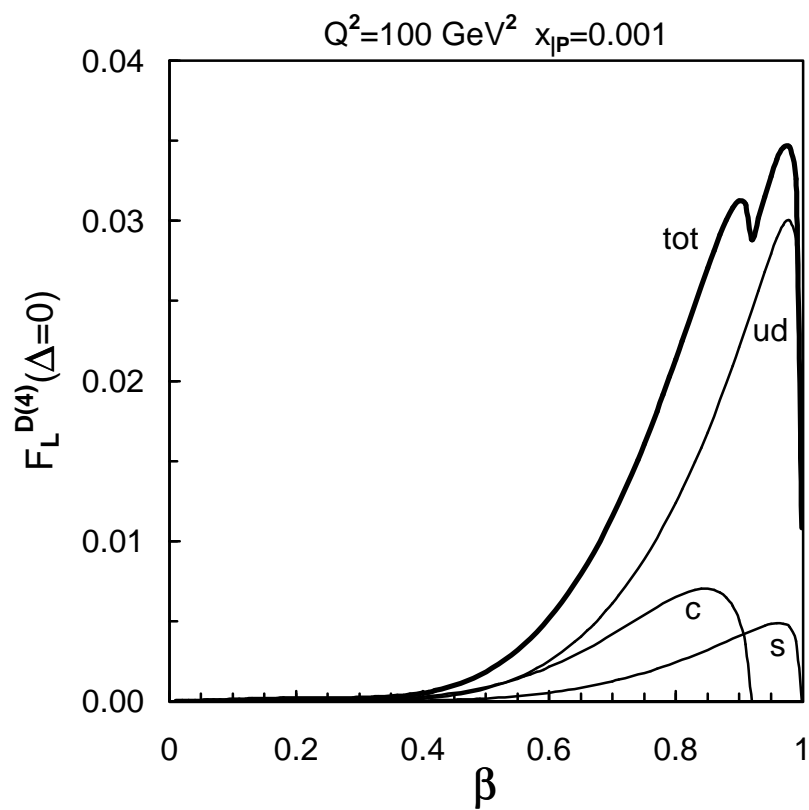


Fig.(4.1)-7

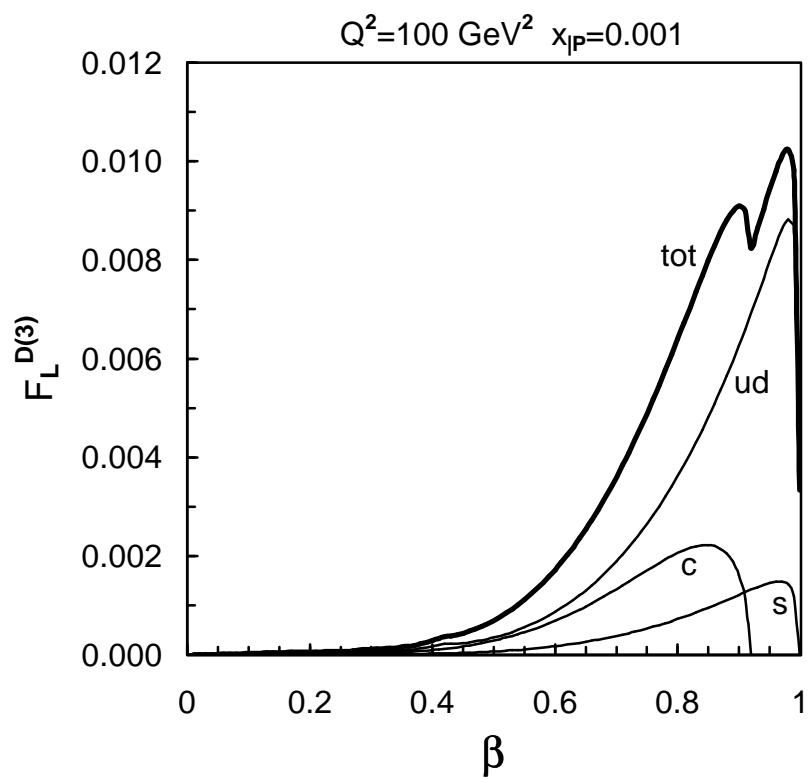


Fig.(4.1)-8

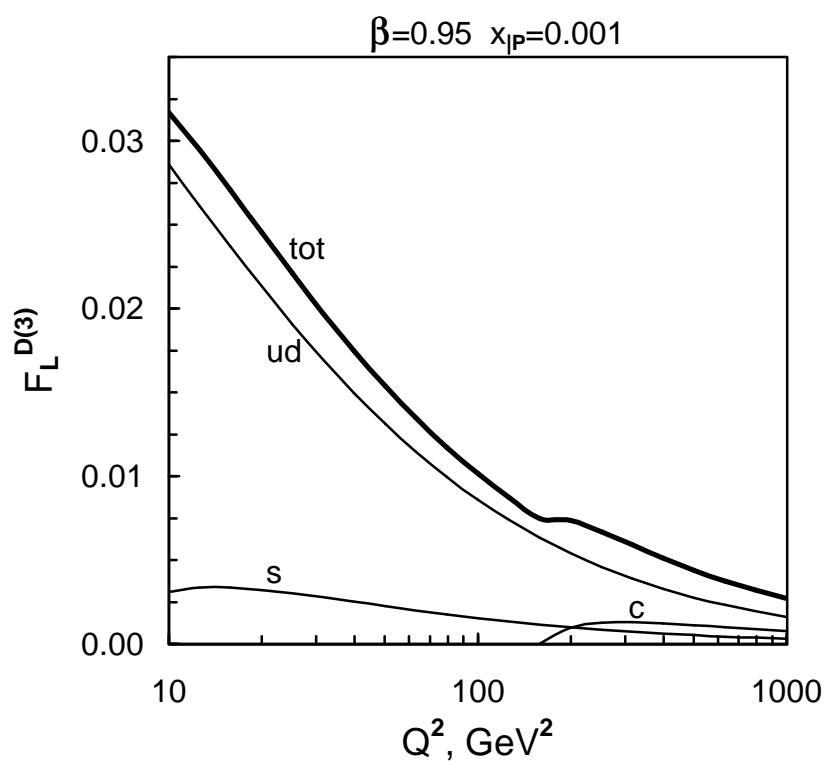


Fig.(4.1)-9

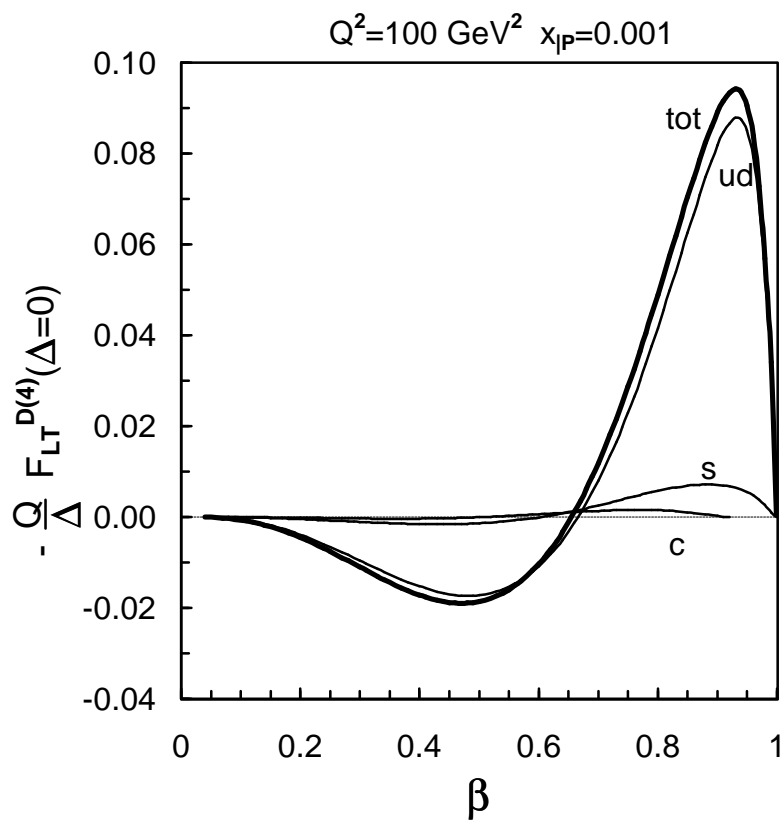


Fig.(4.1)-10

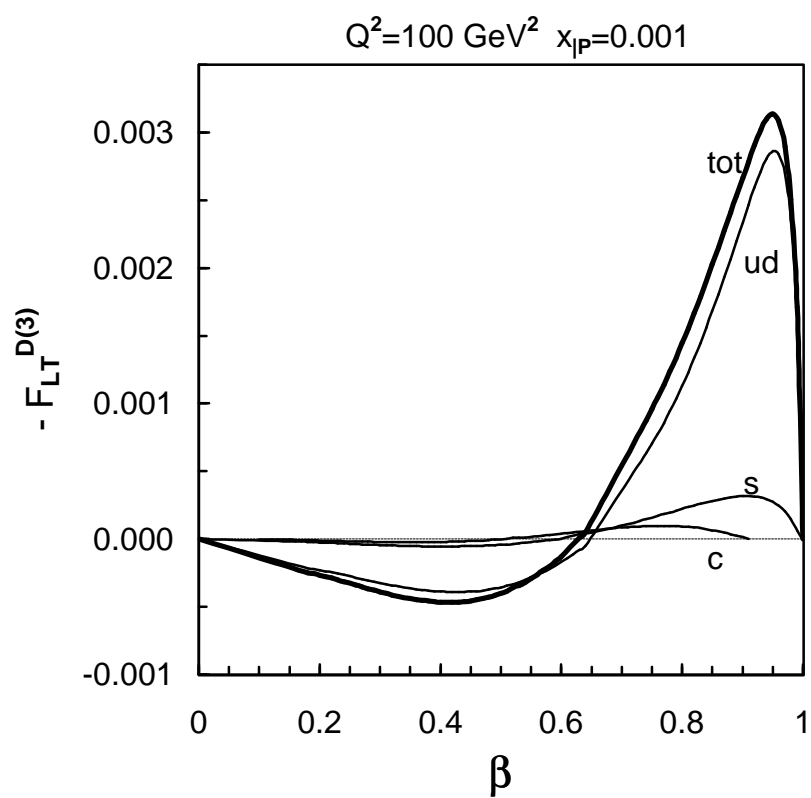


Fig.(4.1)-11

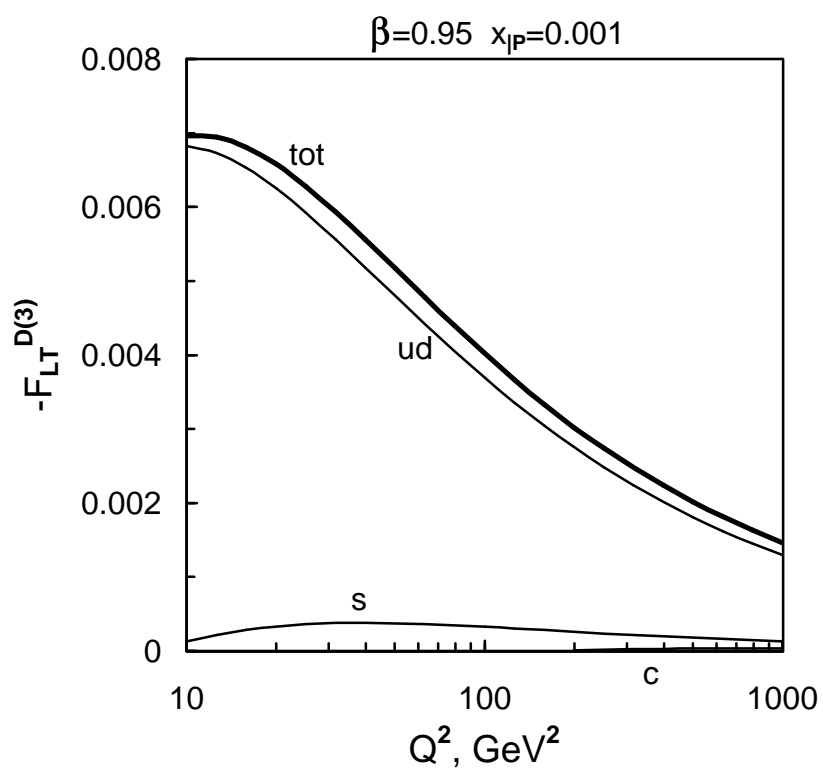


Fig.(4.1)-12

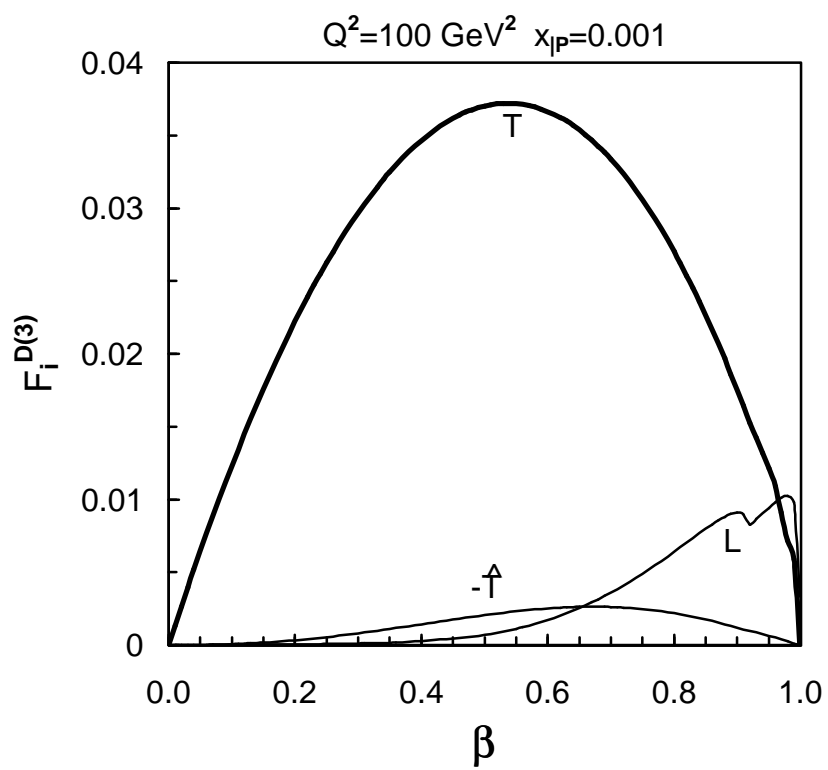


Fig.(4.1)-13

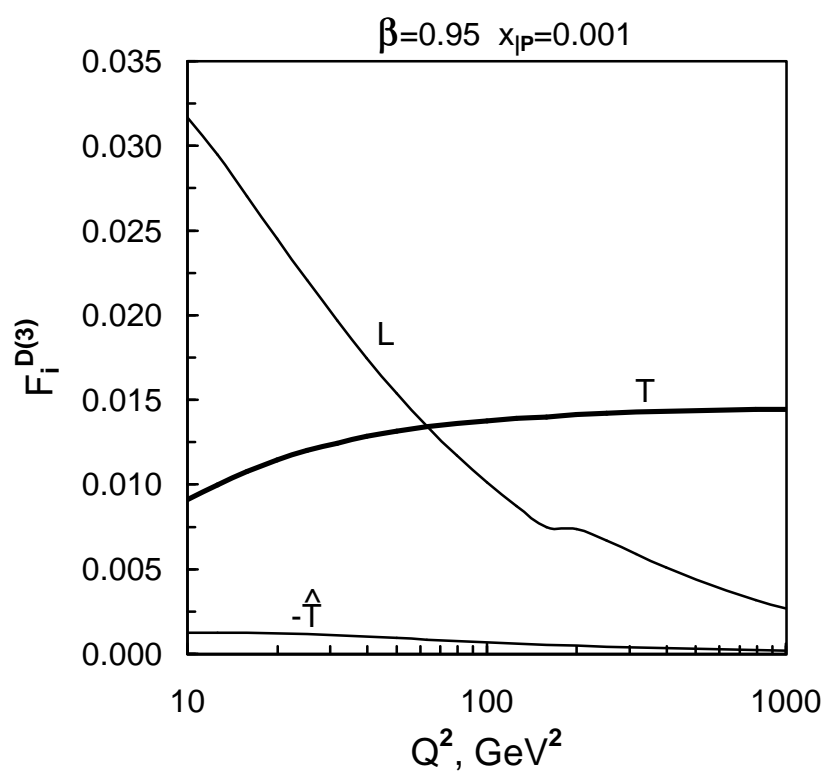


Fig.(4.1)-14

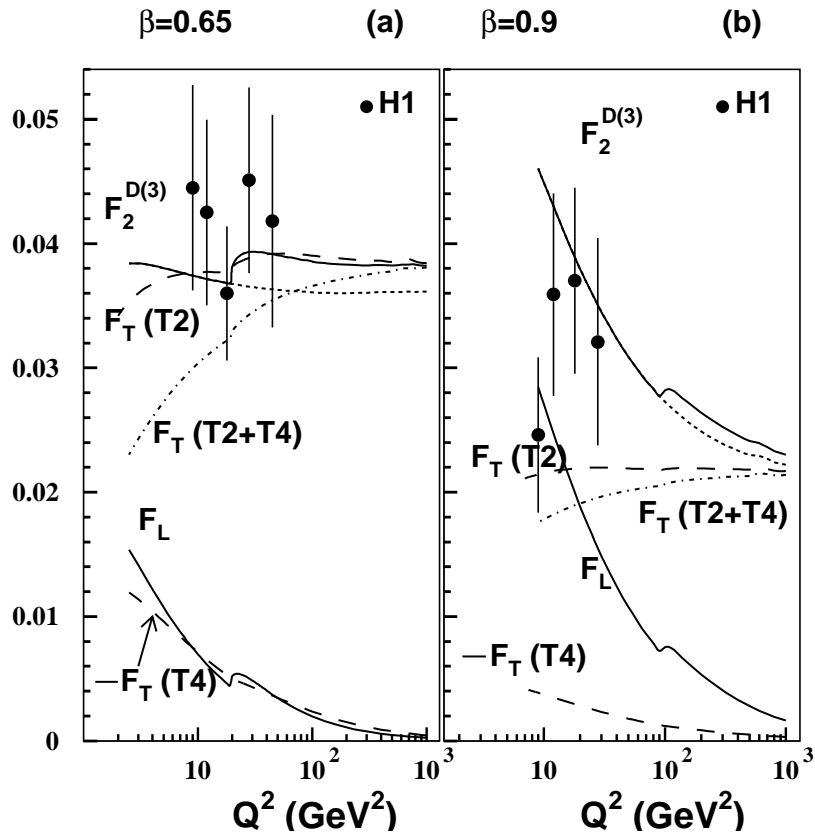


Fig.(4.1)-15

$F_2^{D(3)}$

• H1

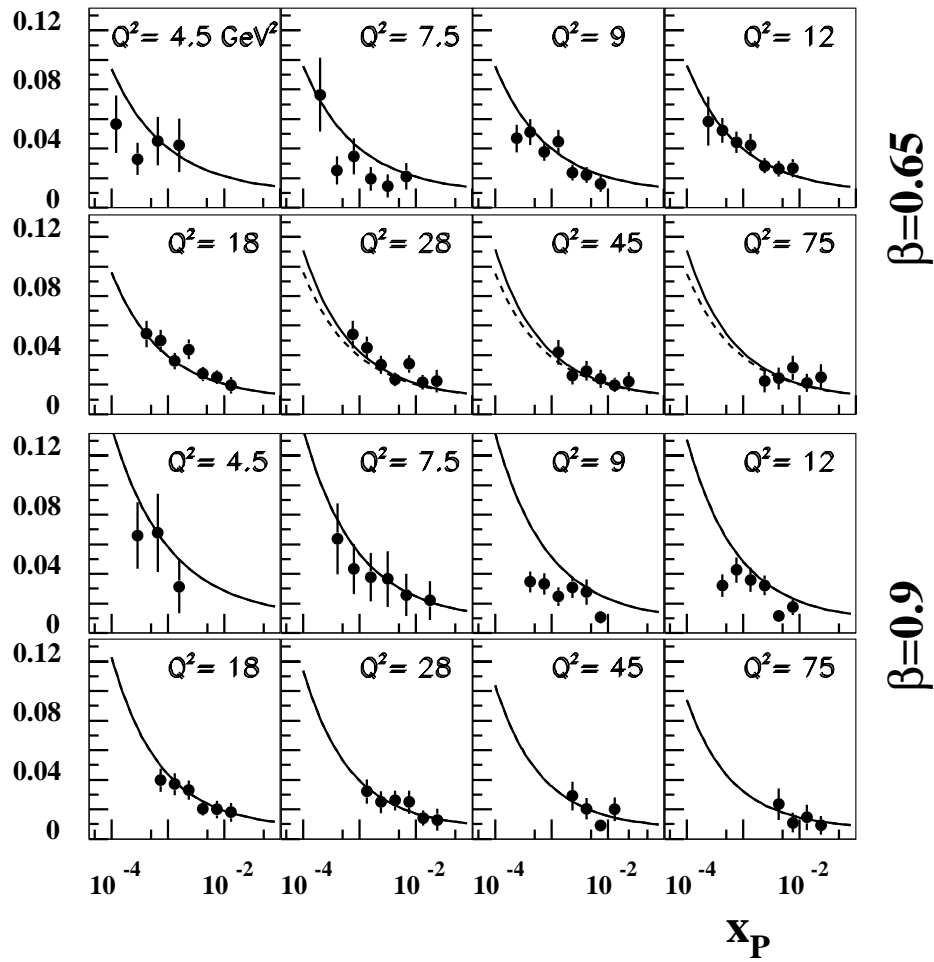


Fig.(4.1)-16

4.2 Azimuthal asymmetries and ratios

The ratio of longitudinal and transverse structure functions, defined as

$$R_{L/T}^{D(3,4)} = \frac{F_L^{D(3,4)}}{F_T^{D(3,4)}}, \quad (4.12)$$

is an important and much discussed test of the pQCD mechanism of DDIS. Following Ref. [6], we notice comparing (4.5) and (4.4) that for large β the longitudinal component dominates over the transverse due to the absence of the small factor $(1 - \beta)^2$ in $F_L^{D(3,4)}$. From (4.5) and (4.4) we explicitly find

$$R_{L/T}^{D(4)} = \frac{24m_f^2}{Q^2} \frac{\beta^2}{(1 - \beta)^2} \frac{(1 - 2\beta)^2}{3 + 4\beta + 8\beta^2}, \frac{\overline{G}_L^2}{\overline{G}_T^2} \quad (4.13)$$

and

$$R_{L/T}^{D(3)} = R_{L/T}^{D(4)} \cdot \frac{B_T}{B_L}. \quad (4.14)$$

Apart from the factor $(1 - \beta)^2$ in the denominator of (4.13) there is an additional increase in these L/T ratios due to the large (for intermediate β) ratio $\overline{G}_L^2/\overline{G}_T^2$ of pQCD factors. Near the threshold region we have, according to (3.39) and (3.44),

$$R_{L/T}^{D(4)} = \frac{Q^2}{4m_f^2}, \quad (4.15)$$

which is large for $Q^2 \gg m_f^2$. In small- x inclusive DIS, the result for the L/T ratio is quite the opposite and theory [29] predicts, in agreement with experiment [30], the small value $R = \sigma_L/\sigma_T \sim 0.2-0.3$. We show the results of the $R_{L/T}^{D(3,4)}$ numerical calculations in Fig.(4.2)-

1. One can indeed see the dramatic increase in the L/T ratio. The difference between $R_{L/T}^{D(3)}$

and $R_{L/T}^{D(4)}$ is due to the falloff of the diffractive slope B_T away from the threshold. See Sec.4.3.

The predictions for the LT and TT' asymmetries,

$$A_{LT}^{D(3)} = \frac{F_{LT}^{D(3)}}{F_T^{D(3)} + F_L^{D(3)}} \quad (4.16)$$

and

$$A_{TT'}^{D(3)} = \frac{F_{TT'}^{D(3)}}{F_T^{D(3)} + F_L^{D(3)}}, \quad (4.17)$$

are shown in Fig.(4.2)-2 and Fig.(4.2)-3, as functions of β and Q^2 , respectively. Spikes on the Q^2 -curves are due to flavor thresholds at $Q_{ih}^2 = 4m_f^2/(1 - \beta)$. Experimentally, the structure function $F_{LT}^{D(3)}$ can be extracted if one measures the difference between the number of events with recoiled proton momentum in the upper and lower planes with respect to the direction \mathbf{e} of the transverse momentum of the recoiled electron. The diffractive structure function $F_{TT'}^{D(3)}$ corresponds to the difference in the number of events in top+bottom and left+right quarters of the $q\bar{q}$ jet plane.

First, we will concentrate on the LT asymmetry. Measurement of this quite large (at maximum $-A_{LT}^{D(3)} \sim 0.16$) observable with LPS is a good method to find the L/T ratio and we show here, following Ref. [11], how the latter can be reconstructed. Experimentally, it is hard to separate the T and L contributions in the total cross-section. One possibility is to use the y -dependent kinematical factors in (2.29), but in HERA the ep center of mass energy squared s is fixed. The only way to change y is to vary Q^2 , $x_{\mathbf{P}}$ or β , but $F_i^{D(3)}$ strongly

depends on these variables. We suggest another method based on the relationship between the T and LT components. In the limit $Q^2 \gg \overline{Q_{th}^2}$ one has the following analytical result for the LT to T ratio in the $\Delta \rightarrow 0$ limit

$$R_{LT/T}^{D(4)} = \frac{F_{LT}^{D(4)}}{F_T^{D(4)}} = \frac{\Delta}{Q} \frac{24\beta^3 (2 - 3\beta)}{(1 - \beta)(3 + 4\beta + 8\beta^2)}. \quad (4.18)$$

Apart from the kinematical factor Δ/Q , it is a model-independent ratio of β -polynomials. In Fig.(4.2)-4 we show the analytical (anl) result of (4.18) in comparison with the direct numerical calculation (num). To obtain the L/T ratio from the LT asymmetry, we use

$$R_{L/T}^{D(4)} = \frac{R_{LT/T}^{D(4)}}{A_{LT}^{D(4)}} - 1. \quad (4.19)$$

See (4.12), (4.16) and (4.18). We test the accuracy of our model-independent extraction by taking the ratio

$$\rho_{L/T}^{D(4)} = \frac{R_{L/T}^{D(4)}(anl)}{R_{L/T}^{D(4)}(num)} \quad (4.20)$$

of numerically calculated with the use of L and T structure functions ratio $R_{L/T}^{D(4)}(num)$, and $R_{L/T}^{D(4)}(anl)$ from (4.19) and (4.18). In Fig.(4.2)-5 we show $\rho_{L/T}^{D(4)}$ for an interesting region of $\beta = 0.9 - 0.97$ for which the L/T ratio is large. Here one can still neglect the contribution from vector meson diffractive production. One can see that the accuracy is adequate for a reliable check of pQCD prediction that the higher twist L component dominates over the leading twist T component.

One can use the TT' asymmetry measurement and the model-independent equality $F_{TT'}^{D(4)} = F_{\hat{T}}^{D(4)}$ for $\Delta = 0$, to extract the twist-4 component \hat{T} of the transverse structure

function. We use (4.5) and (4.7) to find the ratio

$$R_{L/TT'}^{D(4)} = \frac{F_L^{D(4)}}{F_{TT'}^{D(4)}} = \frac{F_L^{D(4)}}{F_{\hat{T}}^{D(4)}} = -\frac{(1-2\beta)^2}{2\beta(1-\beta)}, \quad (4.21)$$

which depends only on β . This L/TT' ratio is shown in Fig.(4.2)-6, calculated numerically (num), directly from the L and TT' structure functions, and with the use of the analytical (anl) formula (4.21). One can see that both curves have similar shapes, but can differ significantly for different β . This can be explained in the same way as the difference in flavor contributions to the L and TT' structure functions: the logarithmic integration in (2.89) for $n = 1$ converges in the whole range of \overline{Q}^2 , so we can not expect more than a *log*-accuracy. Numerical calculation gives cancellation of positive L and negative \hat{T} twist-4 contributions for $\beta = 0.67$, while the analytical result (4.21) shows that cancellation for $\beta = 0.79$. Though the L/TT' ratio (4.21) is less reliable than the LT/T ratio (4.18), it can still be used to test experimentally the dominance of the higher-twist longitudinal structure function with the help of

$$R_{L/T}^{D(4)} = \frac{R_{L/TT'}^{D(4)} A_{TT'}^{D(4)}}{1 - R_{L/TT'}^{D(4)} A_{TT'}^{D(4)}}, \quad (4.22)$$

which is the result of (4.12), (4.17) and (4.21).

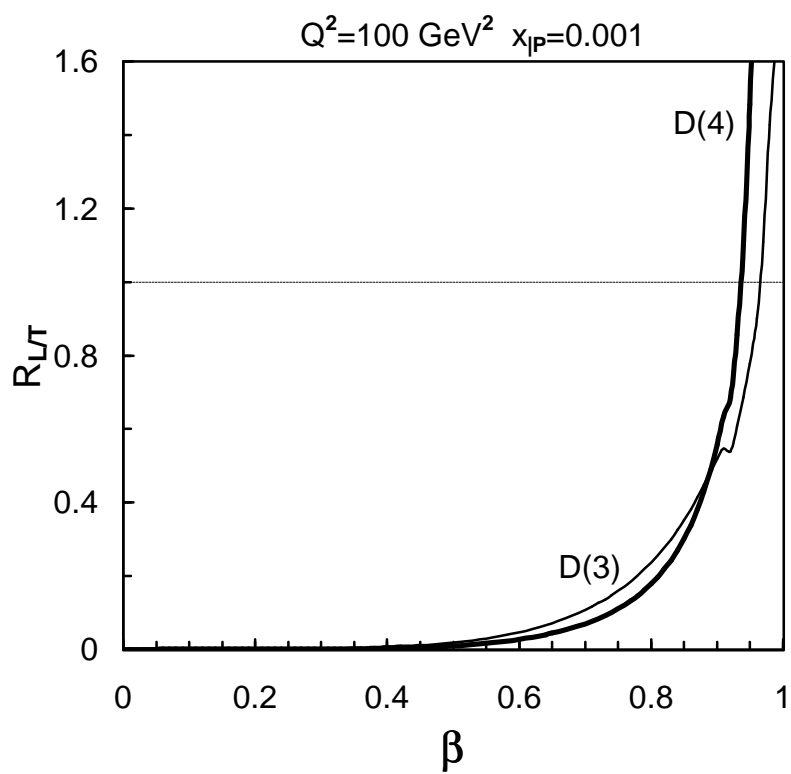


Fig.(4.2)-1

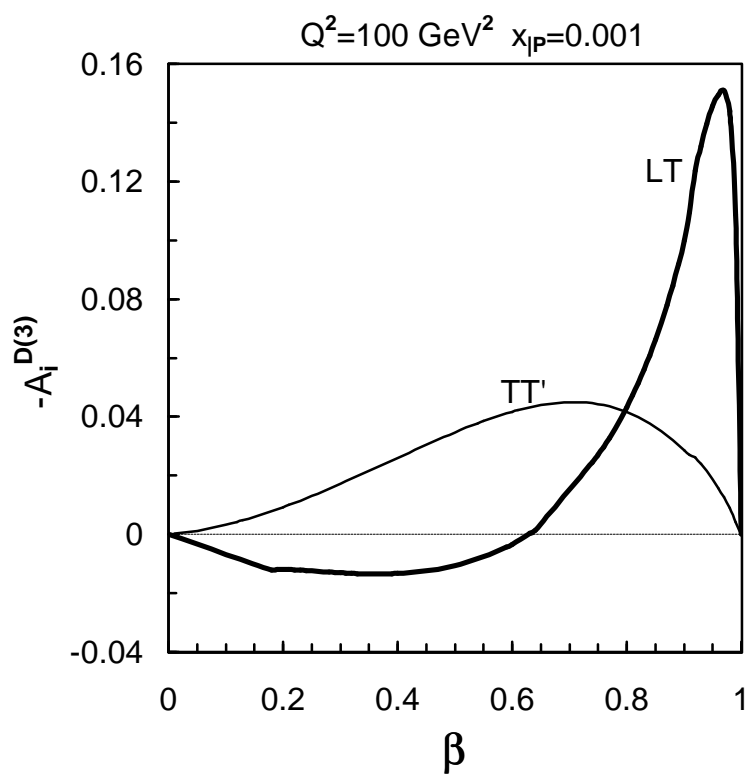


Fig.(4.2)-2

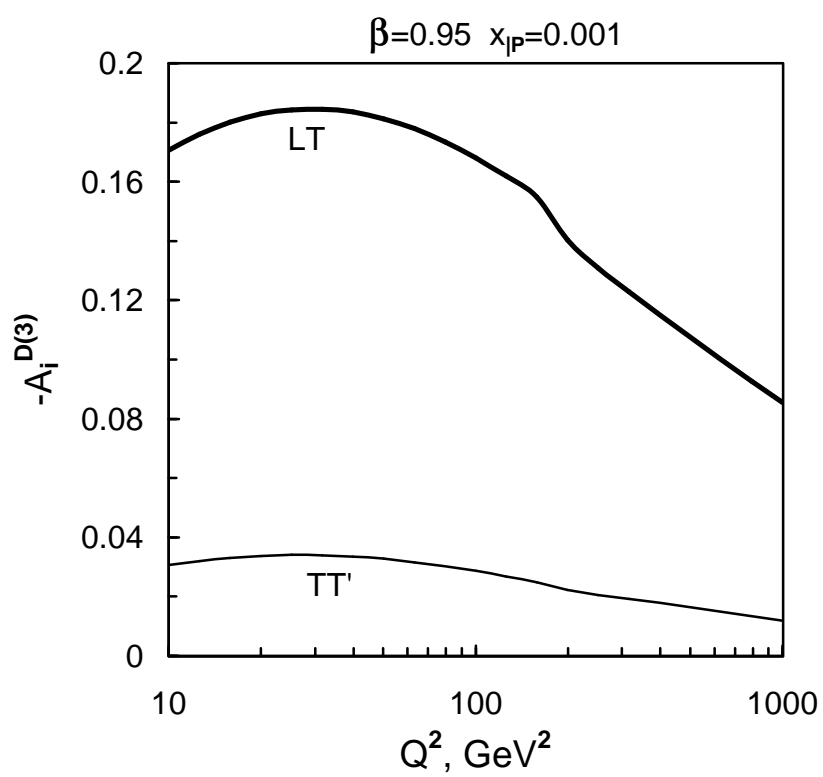


Fig.(4.2)-3

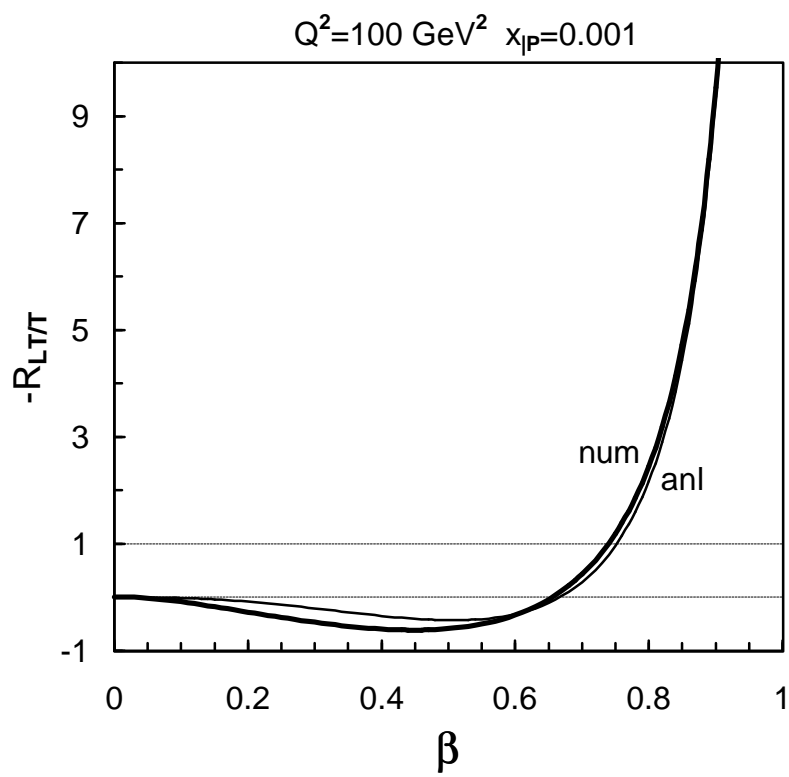


Fig.(4.2)-4

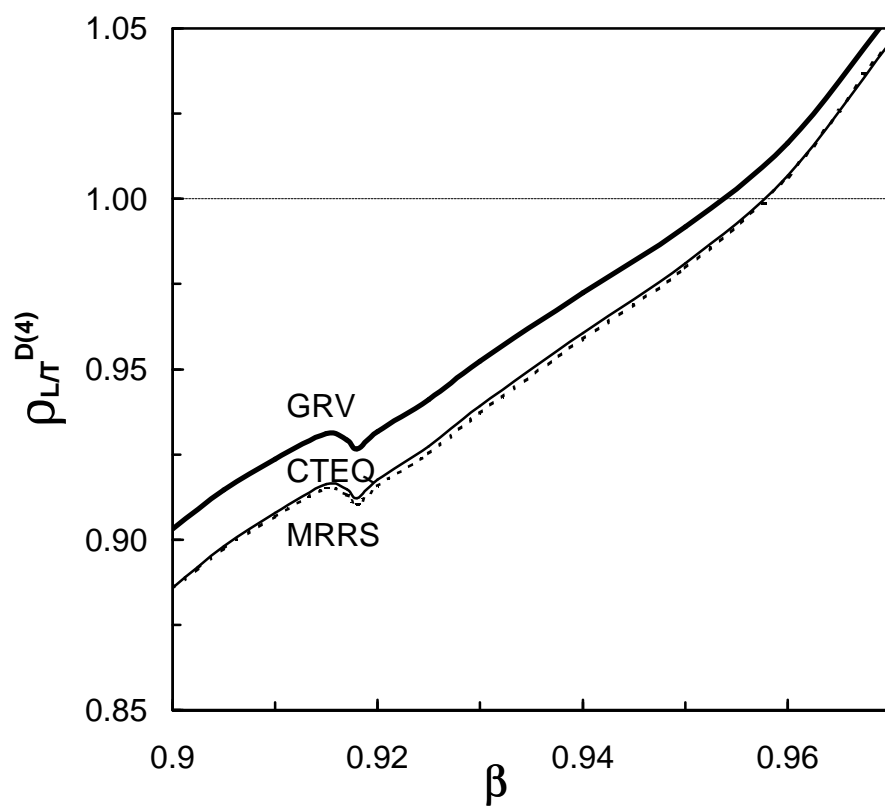


Fig.(4.2)-5

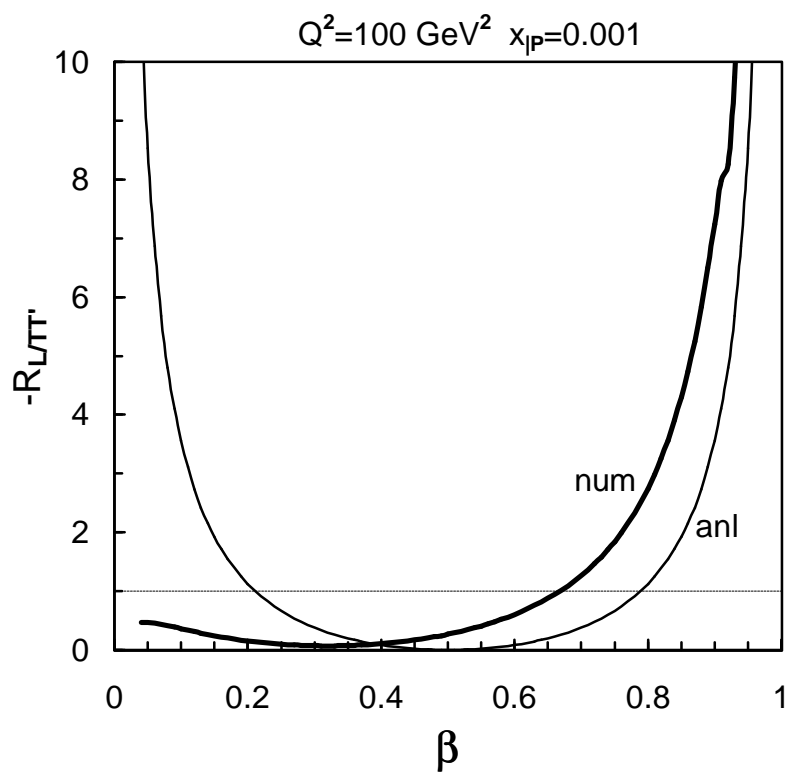


Fig.(4.2)-6

4.3 Diffractive slope

The diffractive slope is one of the principal observables which measures the impact parameter structure of diffractive scattering. The leading proton spectrometer (LPS) of the ZEUS and H1 detectors at HERA [31] measures the transverse momentum transfer Δ , so the diffractive slope $B_D = -\partial \log(d\sigma^D/d\Delta^2)/\partial \Delta^2|_{\Delta=0}$ in DDIS is accessible.

For a complete review on diffraction of hadrons and/or real photons see Ref. [32]. The diffractive slope in any two-body diffractive scattering $ac \rightarrow bd$ can be written as a sum of three impact parameter regions $B_D = B_{ab} + B_{cd} + B_{int}$ (see Fig.(2.1)-1c as an example for $\gamma^*p \rightarrow Xp'$ case), where B_{ij} comes from the size of the ij transition vertex and the relatively small B_{int} comes from the interaction region [32, 33]. The values of B_{ij} depend strongly on the excitation energy in the $i \rightarrow j$ transition, $\Delta M^2 = m_j^2 - m_i^2$. In elastic scattering, $i = j$, one finds $B_{ii} \approx R_i^2/3 \sim 4-6 \text{ GeV}^{-2}$, where R_i^2 is the mean squared hadronic radius, and typically $B_{el} \sim 10 \text{ GeV}^{-2}$. The similar estimate $B_{ij} \approx R_{i,j}^2/3$ holds for diffraction into low-mass continuum states, $\Delta M^2 \lesssim m_N^2$, and both diffraction into low-mass continuum and elastic scattering fall into the broad category of exclusive diffraction for which $B_D \sim B_{el}$. However, for an excitation of high-mass continuum, $\Delta M^2 \gtrsim m_N^2$ (the so-called triple-pomeron (**3IP**) region of diffraction) the size of the diffracting particle no longer contributes to the diffractive slope, and $B_D = B_{\mathbf{3IP}} = B_{pp} + B_{int} \sim B_{el}/2 \approx 6 \text{ GeV}^{-2}$. The above slope $B_{\mathbf{3IP}}$ is almost universal for all diffracting beams and excited states X (see [33]). In real photoproduction

the excitation scale is definitely set by the ground-state vector meson mass M_V , and again, $B_D \sim B_{3\mathbf{IP}}$. In the double high-mass diffraction $hp \rightarrow XY$, where $M_{X,Y} \gg m_N$, one is left with a very small $B_D \sim B_{int} \sim 1.5\text{-}2 \text{ GeV}^{-2}$. See Refs. [32, 34].

Another well-understood diffractive process is the elastic production of vector mesons $\gamma^*p \rightarrow Vp'$. In this case the transverse size of the $\gamma^* \rightarrow V$ transition vertex, the so-called scanning radius $\rho_S \sim \sqrt{4C_0/Q^2}$ (see discussion in Sec.3.9) decreases with Q^2 . This is the basis of the prediction [21] that $B_{\gamma^*V} \propto \rho_S^2$ and of the decrease of the diffractive slope B_V down to $B_V \approx B_{3\mathbf{IP}}$ at very large Q^2 , which is in good agreement with experiment [35].

We present predictions for the Q^2, M^2 and flavor dependence of the diffractive slope for semi-inclusive DDIS, which is nontrivial due to the presence of multiple scales: M^2, Q^2 and m_f^2 . For very large excitation masses, $M^2 \gg Q^2$ or $\beta \ll 1$, though, we recover the inclusive regime of small B_{γ^*X} and $B_D \sim B_{3\mathbf{IP}}$. This triple-pomeron limit of $\beta \ll 1$ is in fact dominated by the excitation of $q\bar{q}g$ and higher Fock states of the photon, which is a genuine inclusive process and again one can argue [16] that $B_D \approx B_{3\mathbf{IP}}$, which was recently confirmed by experiment [31].

Using the impact-parameter language, one can write the diffractive slope of diffractive excitation of intermediate continuum masses $M^2 \lesssim Q^2$ as a sum of components $B_{f,i} = B_{3\mathbf{IP}} + B_{\gamma^*X}$, $B_{\gamma^*X} = b_{T,L} + \bar{B}_{f,i}$, where $\bar{B}_{f,i} \propto 1/m_f^2$ and $b_{T,L}$ come from the γ^*X vertex.

From (3.7), (3.10), (3.15) and (3.17) we have

$$\bar{B}_{f,T} = -\frac{1}{m_f^2} \frac{(5 - 16\beta - 7\beta^2 - 78\beta^3 + 126\beta^4)}{10(3 + 4\beta + 8\beta^2)}, \quad (4.23)$$

$$\bar{B}_{f,L} = -\frac{(1 - \beta)}{m_f^2} \frac{\bar{Q}_T^2}{\bar{Q}_L^2} \frac{(1 - 7\beta + 23\beta^2 - 21\beta^3)}{2(1 - 2\beta)^2}, \quad (4.24)$$

$$\bar{B}_{f,LT} = -\frac{(1 - \beta)}{m_f^2} \frac{(2 + 7\beta + 12\beta^2 - 483\beta^3 + 672\beta^4)}{240\beta^2(2 - 3\beta)}, \quad (4.25)$$

$$\bar{B}_{f,TT'} = \frac{(1 - \beta)}{m_f^2} \frac{\bar{Q}_T^2}{\bar{Q}_L^2} \frac{(1 + 2\beta + 3\beta^2 + 84\beta^3)}{40\beta^2}. \quad (4.26)$$

Contribution to diffractive slope b_T , coming from a soft gluon momentum scale, is relatively small. Indeed, according to (2.93), $b_T \lesssim 1/(2\mu_G^2) \sim 1 \text{ GeV}^{-2}$ and it slowly decreases due to logarithmic, scaling violating increase of the gluon structure function in the denominator of (2.93) with $\bar{Q}_T^2 \sim m_f^2/(1 - \beta)$. The slope parameter b_L can be safely neglected due to the small ratio $G(x_{\mathbf{IP}}, \mu_G^2)/G(x_{\mathbf{IP}}, \bar{Q}_L^2)$ for large $\bar{Q}_L^2 \sim Q^2/4$. From (4.23-4.26) one can see that for heavy flavors all the slopes are close to the universal $B_{3\mathbf{IP}}$ for all values of β due to the small factor $1/m_f^2$ in $\bar{B}_{f,i}$. For light flavors, there exist some nontrivial variations.

For the transverse polarization, one can see, according to (4.23), that the slope is large, as $\bar{B}_{f,T}(\beta \sim 1/2) \sim 1/(10m_f^2)$ for intermediate $\beta \sim 1/2$, and drops towards large β below $B_{3\mathbf{IP}}$ as $\bar{B}_{f,T}(\beta \sim 1) \sim -1/(5m_f^2)$, but close to the threshold, one has according to (3.39),

$$\bar{B}_{f,T} = -\frac{v^2}{6m_f^2}, \quad (4.27)$$

and $\bar{B}_{f,T}(\beta \rightarrow \beta_{th}) \propto (\beta - \beta_{th}) \rightarrow 0$, and transverse slope restores to the universal value of $B_{3\mathbf{IP}}$. All these features can be traced in Fig.(4.3)-1 and Fig.(4.3)-2. The effective dipole

size $\rho^2 \sim 1/\overline{Q}_T^2 \sim (1 - \beta)/m_f^2$ of the $\gamma^* \rightarrow X$ vertex decreases with $\beta \rightarrow 1$, which explains the decrease of B_T towards large β . The decrease of the slope away from the threshold $\propto (\beta - \beta_{th})$ is interesting from the point of view of the exclusive-inclusive duality [6] and nicely correlates with the prediction of a small diffractive slope of vector meson production $B_D(\gamma^* \rightarrow V)$ for which the scanning radius ρ_S is small [21].

For L and TT' one can see from (4.24) and (4.26) the suppression of $\bar{B}_{f;L,TT'}$ due to a small factor $(1 - \beta)\overline{G}_T^2/\overline{G}_L^2$ in the whole range of β . Fig.(4.3)-3 and Fig.(4.3)-4 reveal an uneventful $\bar{B}_{f;L,TT'}$ with the exception of the region $\beta \sim 1/2$, where the L slope is ill-defined due to the factor $(1 - 2\beta)^2$ in the L structure function (4.5).

For intermediate β , the behavior of the LT slope is similar to that for the T slope as $\bar{B}_{f,LT}(\beta \sim 1/2) \sim 1/(6m_f^2)$, but there is a rapid decrease $\bar{B}_{f,LT}(\beta \sim 1) \propto 1 - \beta$ towards large β . One can see in Fig.(4.3)-5 that indeed the LT slope has maximum for $\beta \sim 1/2$ and returns to $B_{3\mathbf{P}}$ towards the threshold. There are regions (shown as dashed line) around $\beta \sim 0, 2/3$ where LT slope is ill-defined due to the factor $\beta^2(2 - 3\beta)$ in the LT structure function (4.5).

It is difficult to test the large β behavior of the T slope because the contribution of the L structure function is dominant.

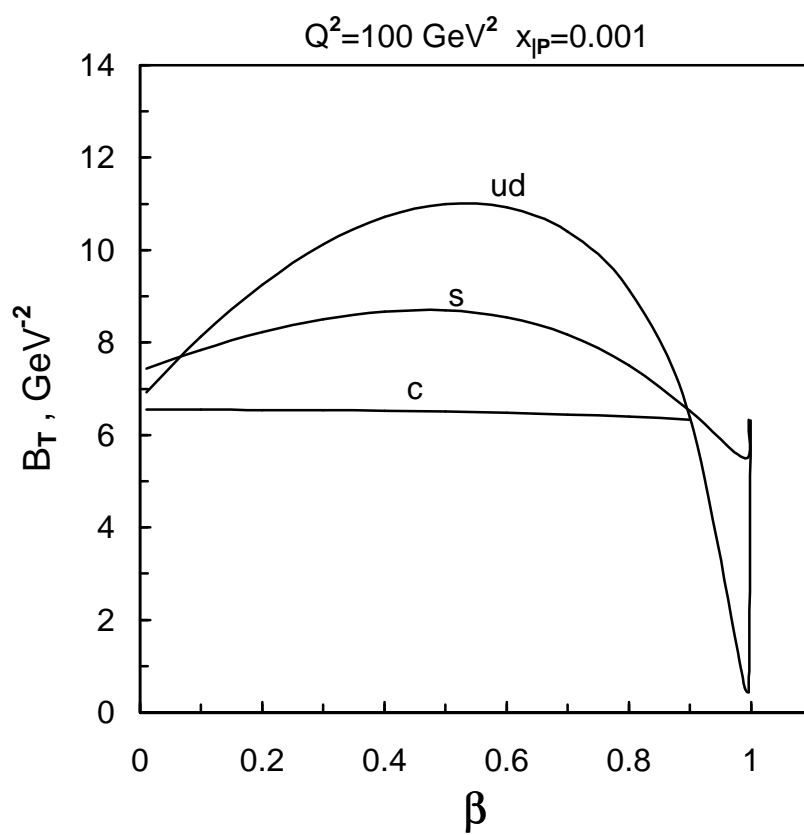


Fig.(4.3)-1

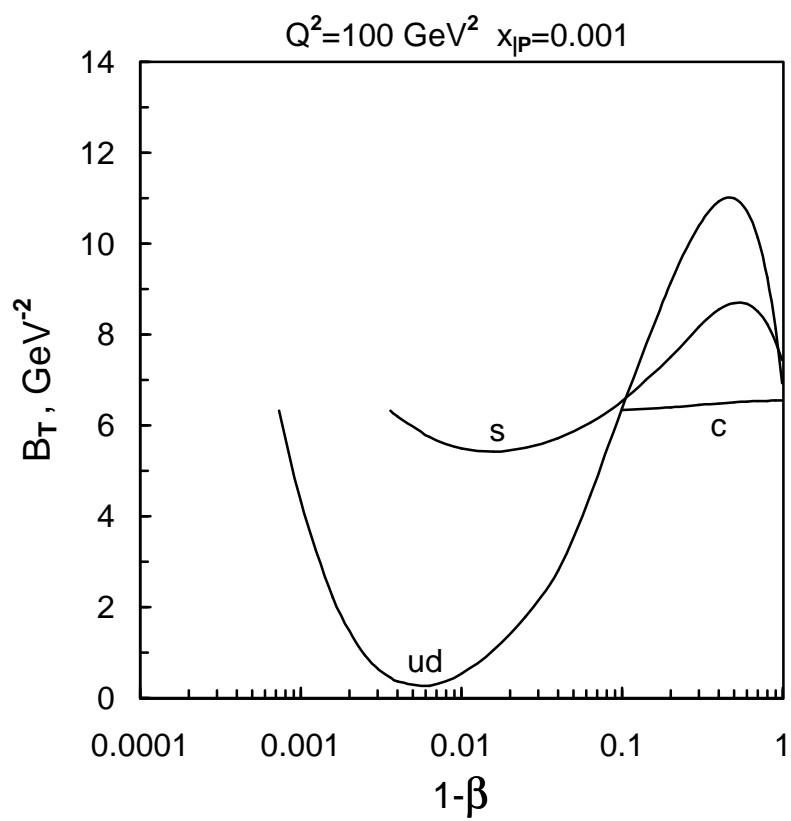


Fig.(4.3)-2

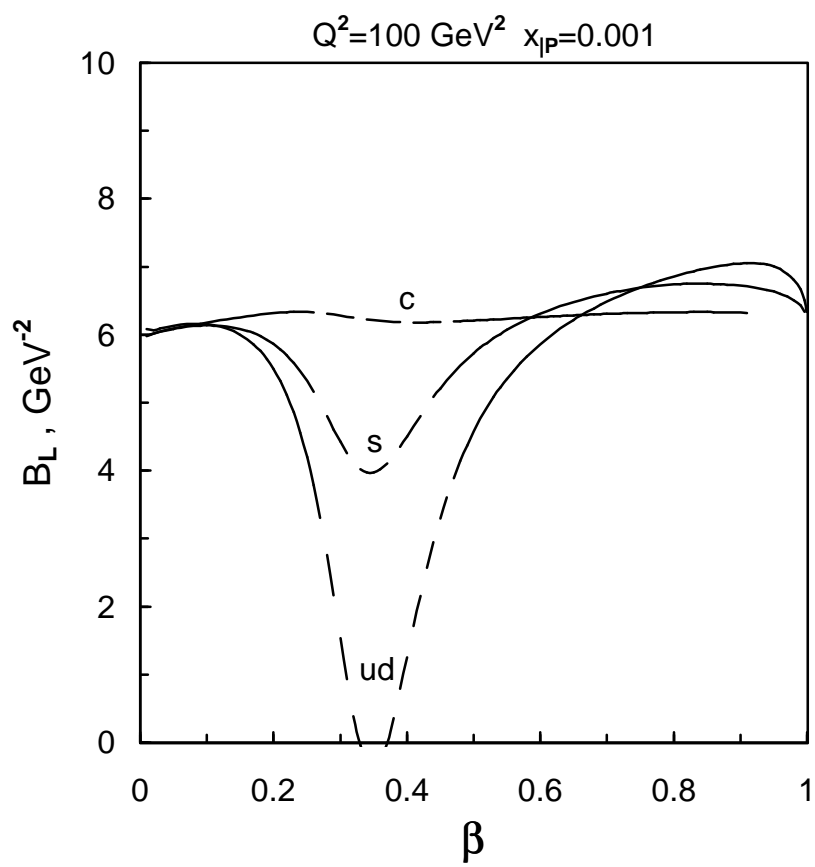


Fig.(4.3)-3

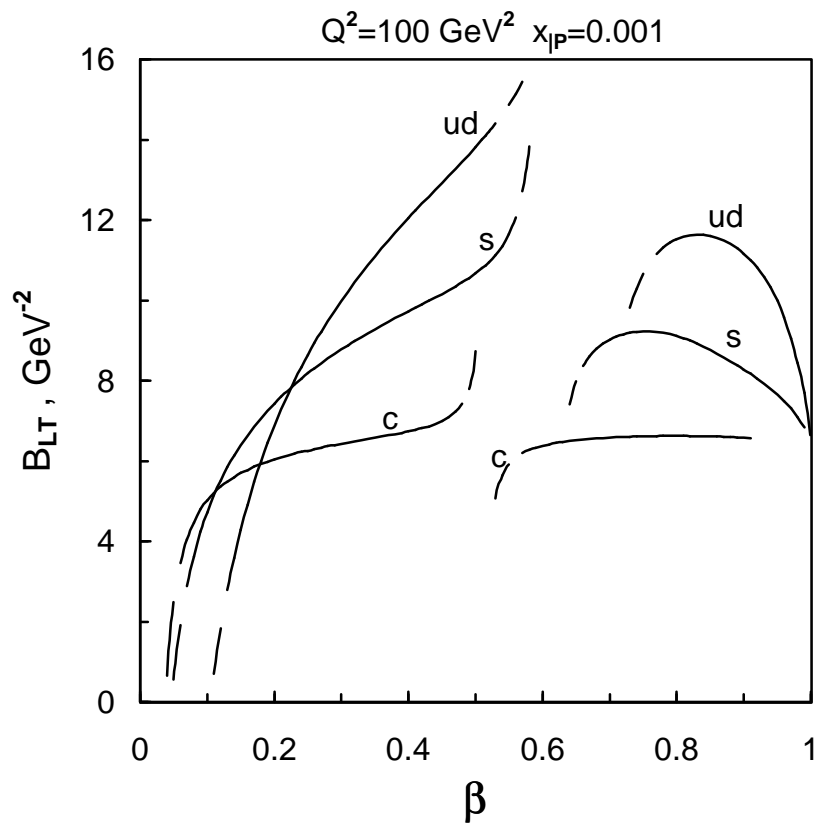


Fig.(4.3)-4

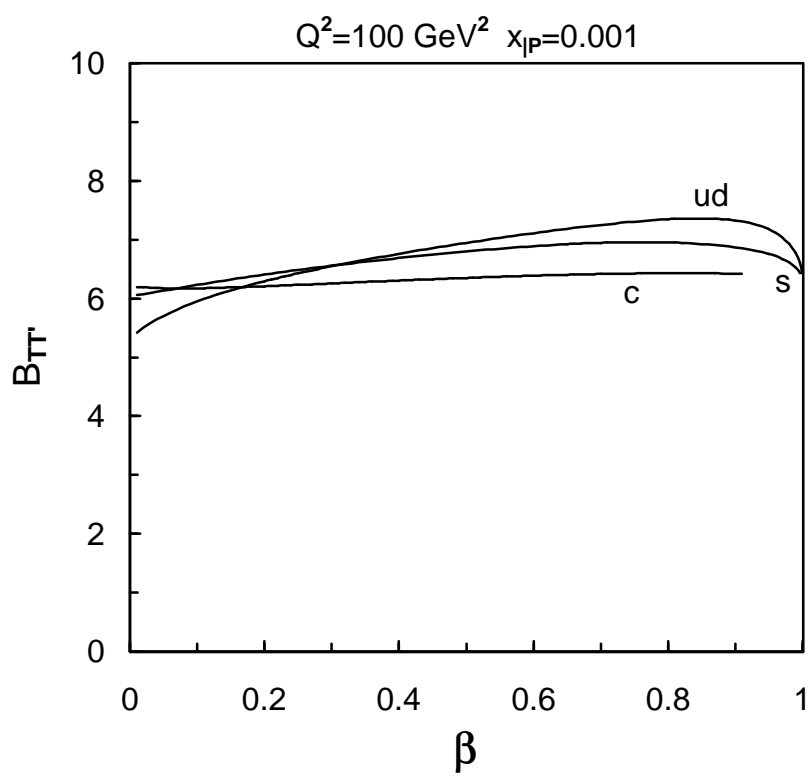


Fig.(4.3)-5

4.4 Gluon structure function interpolation

We performed numerical calculations of the diffractive structure function components and the diffractive slopes using (2.64-2.74). In principle, one needs to know the unintegrated gluon structure functions for the full range of gluon transverse momentum squared κ^2 in (2.54). The dominant contribution comes from the pQCD scales \bar{Q}^2 in the soft-to-hard transition region, spanning from the soft gluon momentum scale $\mu_G^2 \sim 0.5 \text{ GeV}^2$, to the semi-hard $\bar{Q}_T^2 \sim m_f^2/(1 - \beta)$ scale (which depends on flavor and β), and, eventually, to the flavor-independent hard scale $\bar{Q}_T^2 \sim Q^2/4\beta$. For light flavors and intermediate β , the scale $\bar{Q}_T^2 \sim m_f^2/(1 - \beta)$, entering the calculations of the leading twist transverse and LT interference structure functions, is replaced by a range of rapid variation of the gluon structure function μ_G^2 . See (2.81). The existing perturbative gluon structure function parameterizations, by Gluck-Reya-Vogt (GRV) [36], Martin-Roberts-Ryskin-Stirling (MRRS) [37], and Coordinated Theoretical-Experimental Project on QCD (CTEQ) [38], give the structure functions only for gluons with $\bar{Q}^2 \geq \bar{Q}_P^2$, where $\bar{Q}_{GRV}^2 = 0.4 \text{ GeV}^2$, $\bar{Q}_{CTEQ}^2 = 0.49 \text{ GeV}^2$, and $\bar{Q}_{MRRS}^2 = 1.25 \text{ GeV}^2$. The numerical results for gluon structure functions in three different parameterizations are shown in Fig.(4.4)-1, in comparison with the Born approximation to the gluon structure functions defined below.

The unintegrated gluon Born structure function $f_B(\mu_G, \boldsymbol{\kappa}, \boldsymbol{\Delta})$ with an infrared cutoff

parameter μ_G reads

$$\frac{f_B(\boldsymbol{\kappa}, \Delta)}{\kappa^4} = \frac{4\alpha_s(\boldsymbol{\kappa}, \Delta)}{\pi} \frac{V(\kappa^2, \Delta^2)}{\left[(\Delta/2 + \boldsymbol{\kappa})^2 + \mu_G^2\right] \left[(\Delta/2 - \boldsymbol{\kappa})^2 + \mu_G^2\right]}, \quad (4.28)$$

where $V(\kappa^2, \Delta^2)$ is a vertex function defined as

$$V(\kappa^2, \Delta^2) = G_{em}(\Delta^2) - G_{em}(3\kappa^2) G_{em}(\Delta^2/3). \quad (4.29)$$

We used a dipole formula for the electromagnetic form-factor of the proton,

$$G_{em}(\Delta^2) = \frac{1}{(1 + \Delta^2/\Lambda^2)^2} \quad (4.30)$$

with $\Lambda^2 = 0.71 \text{ GeV}^2$, and the running strong coupling constant

$$\alpha_s(k_i) = \frac{4\pi}{9 \log(k_{max}^2/\Lambda_{QCD}^2)}, \quad (4.31)$$

where $k_{max} = \max\{k_i, 0.7 \text{ GeV}\}$ and $\Lambda_{QCD} = 0.2 \text{ GeV}$.

For soft \bar{Q}^2 , we use the interpolation procedure, developed in Refs. [8] and [11], to test the soft-to-hard transition effects in our model. We impose the gauge invariance driven cancellation of soft gluon radiation by colorless protons $f(x_{\mathbf{P}}, \bar{Q}^2 = 0) = 0$, and extrapolate the perturbative gluon density $f_P(x_{\mathbf{P}}, \bar{Q}^2)$, $P = \text{GRV, CTEQ, MRRS}$ by (4.28), using

$$f_P(x_{\mathbf{P}}, \bar{Q}^2) = \theta(\bar{Q}^2 - \bar{Q}_P^2) \frac{\partial G_P(x_{\mathbf{P}}, \bar{Q}^2)}{\partial \log \bar{Q}^2} + \theta(\bar{Q}_P^2 - \bar{Q}^2) \frac{f_B(\mu_G, \bar{Q}^2)}{f_B(\mu_G, \bar{Q}_P^2)} \frac{\partial G_P(x_{\mathbf{P}}, \bar{Q}^2)}{\partial \log \bar{Q}^2} \Bigg|_{\bar{Q}^2 = \bar{Q}_P^2} \quad (4.32)$$

with $\mu_G = 0.75 \text{ GeV}$. Finally, we fix the interpolation parameters in

$$f(x_{\mathbf{P}}, \bar{Q}^2) = C_P \frac{\bar{Q}^2}{\bar{Q}^2 + \bar{Q}_0^2} f_B(\mu_0, \bar{Q}^2) + \frac{\bar{Q}_0^2}{\bar{Q}^2 + \bar{Q}_0^2} f_P(x_{\mathbf{P}}, \bar{Q}^2) \quad (4.33)$$

with $C_{GRV} = 1.7$, $C_{CTEQ} = 1.86$, $C_{MRRS} = 1.7$, $\mu_0 = 0.15 \text{ GeV}$ and $\overline{Q}_0^2 = 3 \text{ GeV}^2$.

The dipole cross-section (3.94), calculated with the gluon structure function in this form, is in good agreement with the one from the gBFKL equation calculations of Ref. [17]. We also get satisfactory agreement for the total structure functions $F_2^{D(3)}$, measured for different β , Q^2 and $x_{\mathbf{P}}$ at HERA [27]. See Sec.4.1.

We estimate the average values of the running pQCD scale (3.20), which enter the calculations of transverse and longitudinal-transverse interference components of cross-sections (3.7) and (3.17). Numerical results for $\langle \overline{Q}_T^2 \rangle$ and $\langle \overline{Q}_{LT}^2 \rangle$, shown in Fig.(4.4)-2 for light flavors u and d , are comfortably large for large β . The dotted curve is given by the formal theoretical estimate $\overline{Q}_T^2 = m_f^2/(1 - \beta)$. One can see the influence of the soft scale μ_G^2 for intermediate and small β . The slight discrepancy between the T and LT curves is caused by different β -polynomials, contributing with different $n \geq 2$ integrals in (2.89). This results in an additional β -polynomial contribution in (3.21) and (3.22) and this relative variation can be seen in Fig.(4.4)-2. The regions (shown by dashed line) with ill-defined, small LT interference contribution for $\beta \sim 0, 2/3$ (see the corresponding factor $\beta^2(2 - 3\beta)$ in denominator in (3.22)), result in variation of LT which is purely an artifact of the averaging procedure. We conclude that the pQCD scale for all cross-section components is at least semi-hard and becomes harder for large β and thus our pQCD calculations are justified even for light flavors.

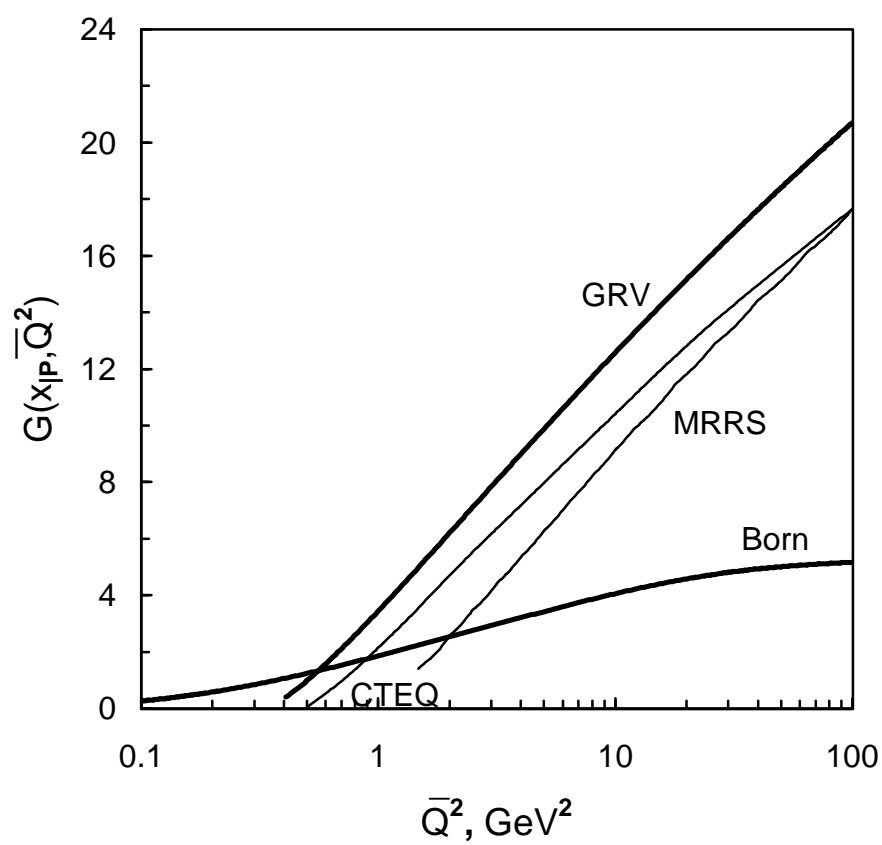


Fig.(4.4)-1

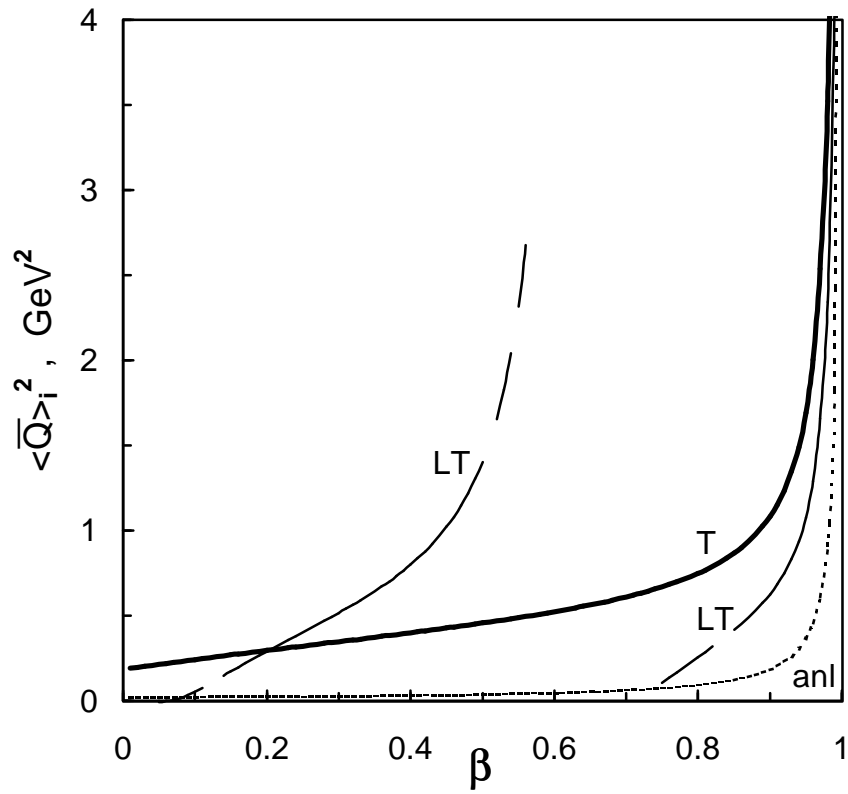


Fig.(4.4)-2

Chapter 5

Nucleon wave function

In this chapter we focus on the proton sector of the interaction. The evaluation of the spin-flip vertex function of proton, done by the author with the use of the relativistic constituent quark model, is presented. The author performed analytical and numerical evaluation of important at small x diffractive contribution to the spin structure function $g_{LT} = g_1 + g_2$. We show that a rapid small- x increase of the diffractive contribution to g_{LT} invalidates superconvergence assumptions behind the Burkhardt-Cottingham sum-rule and the Wandzura-Wilczek relation.

5.1 Nucleon spin flip and conserve

For convenience, we choose in this chapter the z -axis to be oriented in the direction of the initial proton momentum. We will also use $\sqrt{s} = 1$ without loss of generality (s can be easily restored by dimensional analysis where needed and is absent from vertex functions and cross-sections). The four-momentum of proton is then

$$p = (1, m_p^2, \mathbf{0}), \quad (5.1)$$

with helicity $\lambda = \pm 1/2$. The momenta of its three constituent quarks are

$$p_i = \left(x_i, \frac{\mathbf{p}_i^2 + m_q^2}{x_i}, \mathbf{p}_i \right), \quad (5.2)$$

with helicities $\lambda_i = \pm 1/2$ and momentum conservation conditions

$$\sum_i x_i = 1, \quad \sum_i \mathbf{p}_i = 0. \quad (5.3)$$

We calculate the light-cone wave function of the nucleon, following Ref. [40], defined as

$$\psi_\lambda(x_i, \mathbf{p}_i, \lambda_i) = [\Psi_\lambda(\hat{1}, \hat{3}, \hat{2}) - \Psi_\lambda(\hat{3}, \hat{2}, \hat{1})] \Phi(x_i, \mathbf{p}_i), \quad (5.4)$$

where $\hat{i} \equiv (x_i, \mathbf{p}_i, \lambda_i)$ is a collective index of i -th quark, $\Psi_\lambda(\hat{i}, \hat{j}, \hat{k})$ is the spin part of the light-cone wave function, defined as

$$\Psi_\lambda(\hat{i}, \hat{j}, \hat{k}) = \frac{\bar{u}(\hat{i})}{\sqrt{x_i}} \{m_N + p_\mu \gamma^\mu\} \gamma^5 \frac{v(\hat{j})}{\sqrt{x_j}} \cdot \frac{\bar{u}(\hat{k})}{\sqrt{x_k}} u_\lambda(p). \quad (5.5)$$

Using the explicit formulae for spinors u and v in the light-cone momentum frame (A.4), (A.5), we get the following result for the spin part

$$\Psi_\lambda(\hat{i}, \hat{j}, \hat{k}) = \frac{1}{x_i x_j x_k} \left(D_{-, \lambda_i}^i D_{+, \lambda_j}^j - D_{+, \lambda_i}^i D_{-, \lambda_j}^j \right) D_{\lambda, \lambda_k}^k, \quad (5.6)$$

where $D_{\pm, \pm}^i = m_N x_i + m_q$, $D_{\pm, \mp}^i = \pm p_i^x + i p_i^y$ is the analog of the Melosh matrix. See [39]. In the non-relativistic limit $m_q \gg \alpha_q$, $x_i = 1/3$ we have $D_{\lambda, \bar{\lambda}}^i = 2m \delta_{\lambda \bar{\lambda}}$ and we recover nonrelativistic wave functions. In the inequality above, α_q characterizes quark mean square momenta, which enters the space part of the light-cone wave function $\Phi(x_i, \mathbf{p}_i)$ in the gaussian form

$$\Phi(x_i, \mathbf{p}_i) = C_N \exp \left\{ - \sum \frac{\mathbf{p}_i^2 + m_q^2}{x_i} \frac{1}{6\alpha_q^2} \right\}. \quad (5.7)$$

Formula (5.4) is derived by the procedure described in Ref. [40], and is the relativistic generalization of the nonrelativistic constituent-quark-model wave function

$$\psi_\lambda(\mathbf{p}_i, \lambda_i) = C_N \cdot \exp \left\{ - \sum \mathbf{p}_i^2 \frac{1}{2\alpha_q^2} \right\} \cdot \phi_{\lambda_1}^\dagger \sigma_y \phi_{\lambda_2} \phi_{\lambda_3}^\dagger \phi_\lambda. \quad (5.8)$$

Here we only mention that the light-cone wave-function (5.4) is invariant under all kinematical Poincare transformations and satisfies the conventional parity, flavor and color assignments.

We use light-cone wave-functions, described above, to calculate the nucleon vertex functions. The two-gluon vertex function in our light-cone approach with Lorentz-invariant

nucleon wave functions reads

$$V_{f,c} = V_{1f,c} - V_{2f,c} = \sum_{\lambda_i, n_1, n_2} C_{n_1 n_2} \int [dx_i] [d\mathbf{p}_i] \psi'_{\mp}{}^\dagger(x_i, \mathbf{p}'_i, \lambda_i) \psi_+(x_i, \mathbf{p}_i, \lambda_i) \quad (5.9)$$

with the normalization condition

$$\sum_{\lambda_i} \int [dx_i] [d\mathbf{p}_i] \psi_+{}^\dagger(x_i, \mathbf{p}_i, \lambda_i) \psi_+(x_i, \mathbf{p}_i, \lambda_i) = 1. \quad (5.10)$$

In (5.9) and (5.10) we have the integration over

$$[dx_i] \equiv \delta\left(1 - \sum x_i\right) \prod dx_i, \quad [d\mathbf{p}_i] \equiv \delta\left(\sum \mathbf{p}_i\right) \prod d\mathbf{p}_i. \quad (5.11)$$

Summation is performed over all possible spin states λ_i of the constituent quarks and over graphs with gluons attached to different quarks. $n_{1,2}$ is the index of quark to which gluon 1, 2 have transferred momentum $\mathbf{\Delta}_{1,2} = \mathbf{\Delta}/2 \pm \boldsymbol{\kappa}$. The coefficient $C_{n_1 n_2} = 2\delta_{n_1 n_2} - 1$ is the sign of the graph, $C_{n_1 n_2} = \pm 1$ corresponds to vertices $V_{1f,c}$ (gluons attached to a single quark) and $V_{2f,c}$ (gluons attached to two different quarks) in (5.9). In the case of the electromagnetic vertex $\Gamma_{f,c}^{p,n}$, we should replace $C_{n_1 n_2}$ with the charge of quark Q_{n_1} in the proton(neutron), to which the photon transferred momentum $\mathbf{\Delta}$:

$$\Gamma_{f,c}^{p,n} = \sum_{\lambda_i, n_1} Q_{n_1} \int [dx_i] [d\mathbf{p}_i] \psi'_{\mp}{}^\dagger(x_i, \mathbf{p}'_i, \lambda_i) \psi_+(x_i, \mathbf{p}_i, \lambda_i). \quad (5.12)$$

The generic relationship between two-gluon and electromagnetic vertices in our constituent-quark model is $V_{1f,c} = \Gamma_{f,c}^p + \Gamma_{f,c}^n$.

We used for the $q(x_i, \mathbf{p}_i, \lambda_i) g q(x_i, \mathbf{p}'_i, \lambda'_i)$ vertex

$$G_{g(+)}^{\lambda_i, \lambda'_i} = \frac{\bar{u}_{\lambda_i}(x_i, p_i)}{\sqrt{x_i}} \gamma^+ \frac{u_{\lambda'_i}(x_i, p'_i)}{\sqrt{x_i}} = 2\delta_{\lambda_i \bar{\lambda}_i}, \quad (5.13)$$

which, using (A.4) and (A.5), is the only survivor, so quark helicity is conserved for each vertex in our infinite-momentum frame (see also 2.41).

The wave function of the final nucleon $\psi'_\lambda(x_i, \mathbf{p}'_i, \lambda_i)$ is given by (5.4), with the final quark transverse momenta

$$\mathbf{p}'_i = \mathbf{p}_i + (\delta_{n_1 i} - x_i) \mathbf{\Delta}_1 + (\delta_{n_2 i} - x_i) \mathbf{\Delta}_2. \quad (5.14)$$

In the case of single photon exchange, we have a similar expression

$$\mathbf{p}'_i = \mathbf{p}_i + (\delta_{n i} - x_i) \mathbf{\Delta}. \quad (5.15)$$

To simplify calculations, we choose the total momentum transfer $\mathbf{\Delta}$ to be directed along the x -axis, $\mathbf{\Delta} = (\Delta, 0)$, so the spin-flip vertices become real and proportional to Δ . The helicity-conserving quark interaction generates helicity flip of the nucleon due to relativistic effects in the nucleon light-cone wave function in which the sum of the quark helicities may not coincide with the total spin of the nucleon.

It seems impossible to perform analytical calculations using the full six-dimensional integration in (5.9). We calculate integrals analytically, in the $x_i = 1/3$ approximation, where we neglect differences of constituent quark longitudinal momenta. By comparing analytical and numerical results we can evaluate the validity of this approximation. After lengthy but simple calculations of consecutive gaussian integrals over two independent transverse quark

momenta we obtain for the two-gluon nucleon spin-flip vertex

$$\begin{aligned}
V_f = & \frac{5}{24C_0} \frac{\Delta}{6m_q} \left[\frac{\Delta^2}{3m_q^2} G_1 \left\{ 1 - \frac{1}{240} \frac{\Delta^2}{3m_q^2} \right\} \right. \\
& - G_2 \left\{ \frac{1}{2} \left(3 \frac{\kappa^2}{m_q^2} - \frac{\Delta^2}{12m_q^2} \right) - \frac{1}{480} \left(3 \frac{\kappa^4}{m_q^4} + 2 \frac{\kappa^2 \Delta^2}{12m_q^4} - \frac{\Delta^4}{144m_q^4} \right) \right. \\
& \left. \left. - \sin^2(\theta) \frac{\kappa^2}{m_q^2} \left(1 - \frac{1}{120} \frac{\Delta^2}{12m_q^2} \right) \right\} \right], \tag{5.16}
\end{aligned}$$

where θ is the angle between $\boldsymbol{\kappa}$ and Δ . There is a notable absence of a factor $\propto \Delta$ in the nucleon spin-flip vertex, which is the result of an additional longitudinal direction symmetry in our $x_i = 1/3$ approximation. Numerical results, to be discussed in Sec.5.2, give relatively small, but non-zero $\propto \Delta$ contribution. We introduced standard one(two)-boson form-factors

$$G_1 = \exp \left\{ -\frac{\Delta^2}{2} \frac{1}{3\alpha_q^2} \right\}, \tag{5.17}$$

$$G_2 = \exp \left\{ -\left(\kappa^2 + \frac{\Delta^2}{12} \right) \frac{1}{2\alpha_q^2} \right\}. \tag{5.18}$$

For conserved spin we have

$$V_c = V_c^{(0)} - \bar{V}_c, \tag{5.19}$$

where the nonrelativistic constituent quark model contribution is

$$V_c^{(0)} = G_1 - G_2. \tag{5.20}$$

The relativistic correction gives

$$\bar{V}_c = \frac{5}{24C_0} \left[\frac{\Delta^2}{3m_q^2} G_1 \left\{ C_1 - \frac{3C_2}{160} \frac{\Delta^2}{3m_q^2} + \frac{1}{5760} \frac{\Delta^4}{9m_q^4} \right\} \right]$$

$$\begin{aligned}
& -G_2 \left\{ C_1 \left(\frac{\kappa^2}{m_q^2} + \frac{\Delta^2}{12m_q^2} \right) - \frac{3C_2}{160} \left(\frac{\kappa^2}{m_q^2} + \frac{\Delta^2}{12m_q^2} \right)^2 + \frac{1}{5760} \left(3\frac{\kappa^2}{m_q^2} - \frac{\Delta^2}{12m_q^2} \right)^2 \frac{\Delta^2}{12m_q^2} \right. \\
& \left. - \frac{1}{480} \sin^2(\theta) \frac{\kappa^2 \Delta^2}{12m_q^4} \left(4(C_2 + 10) - \frac{\Delta^2}{12m_q^2} \right) \right\}. \tag{5.21}
\end{aligned}$$

We used only two parameters in our calculations: universal scale $\alpha_q = 0.24\text{GeV}$, and constituent quark mass $m_q = m_N/3 = 0.32\text{GeV}$. In (5.21) the factors $C_0 = 1 + a/2 + 5a^2/48 + a^3/144$, $C_1 = 1 + a/4 + 7a^2/360$ and $C_2 = 1 + a/6$ are all between 1 and 2 as $a = \alpha_q^2/m_q^2 = 0.56$ is a not-so-small relativistic parameter in this problem. As required by gauge invariance, even if one of the gluon momenta is zero, the vertex function vanishes due to sign the factor $C_{n_1 n_2}$ in (5.9), and relationship $V_{c,f}(\boldsymbol{\kappa} = \pm\boldsymbol{\Delta}/2) = 0$ is indeed satisfied.

The leading contribution to the diffractive slope of the DDIS comes from the V_{1c} vertex [21] and consists of two parts:

$$B_N^{(0)} = \frac{1}{3\alpha_q^2} = 5.8\text{GeV}^{-2} \tag{5.22}$$

from $V_{1c}^{(0)}$ in (5.17), and

$$\bar{B}_N = \frac{5C_1}{12C_0} \frac{1}{3m_q^2} = 1.2\text{GeV}^{-2} \tag{5.23}$$

from \bar{V}_{1c} vertex $\propto \Delta^2$. See (5.21). Together they combine to $B_N = B_N^{(0)} + \bar{B}_N = 7.0\text{GeV}^{-2}$, which is close to the experimental value $B_{3\mathbf{P}} = 7.2\text{GeV}^{-2}$.

Spin-flip electromagnetic vertex functions of the proton and the neutron are

$$\Gamma_f^p = \frac{2}{C_0} \frac{\Delta}{6m_q} G_1 \left[C_1^f + \frac{C_2^{pf}}{24} \frac{\Delta^2}{3m_q^2} + \frac{1}{2304} \frac{\Delta^4}{9m_q^4} \right], \tag{5.24}$$

$$\Gamma_f^n = -\frac{2}{C_0} \frac{\Delta}{6m_q} G_1 \left[C_1^f - \frac{C_2^{nf}}{16} \frac{\Delta^2}{3m_q^2} + \frac{1}{1152} \frac{\Delta^4}{9m_q^4} \right], \quad (5.25)$$

where the factors $C_1^f = 1 + a/3 + 5a^2/144$, $C_2^{pf} = 1 - a/4$, $C_2^{nf} = 1 + a/6$ are also close to 1. From vertex functions, one can find that the anomalous magnetic moments of the proton and the neutron differ only by sign and are equal to $\kappa_p = -\kappa_n = 2C_1^f/C_0 = 1.82$ ($\kappa_p^{exp} = 1.79$, $\kappa_n^{exp} = -1.91$), and Pauli form-factors of the proton and the neutron are (we neglected $O(\text{momentum}^4)$ terms)

$$F_2^p = G_1 \left[1 + \frac{1}{24} \frac{\Delta^2}{3m_q^2} \right], \quad (5.26)$$

$$F_2^n = G_1 \left[1 - \frac{1}{16} \frac{\Delta^2}{3m_q^2} \right]. \quad (5.27)$$

The spin-conserving electromagnetic vertex functions of the proton and the neutron are

$$\Gamma_c^p = \Gamma_c^{p(0)} - \bar{\Gamma}_c^p, \quad (5.28)$$

where nonrelativistic approximation result is

$$\Gamma_c^{p(0)} = G_1, \quad (5.29)$$

and

$$\bar{\Gamma}_c^p = \frac{1}{24C_0} \frac{\Delta^2}{3m_q^2} G_1 \left[C_1^{pc} + \frac{7C_2^{pc}}{96} \frac{\Delta^2}{3m_q^2} + \frac{1}{1152} \frac{\Delta^4}{9m_q^4} \right], \quad (5.30)$$

$$\Gamma_c^n = -\frac{1}{6C_0} \frac{\Delta^2}{3m_q^2} G_1 \left[C_1^{nc} - \frac{C_2^{nc}}{24} \frac{\Delta^2}{3m_q^2} \right], \quad (5.31)$$

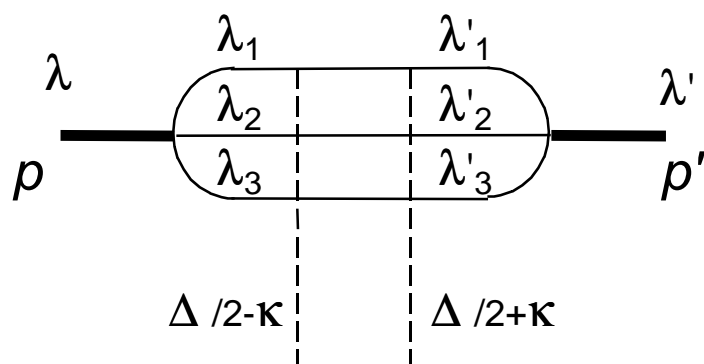
where $C_1^{pc} = 1 + 3a/4 + a^2/9$, $C_1^{nc} = 1 + a/8 - a^2/288$, $C_2^{pc} = 1 - 13a/42$ and $C_2^{nc} = 1 - a/24$ is the set of constants close to 1. One can deduce the charge radii of the proton and the

neutron from

$$r_p^2 = \frac{1}{\alpha_q^2} + \frac{C_1^{pc}}{4C_0} \frac{1}{3m_q^2}, \quad r_n^2 = -\frac{C_1^{nc}}{C_0} \frac{1}{3m_q^2} \quad (5.32)$$

and obtain $r_p = 0.84fm$, $r_n = -0.32fm$ ($r_p^{exp} = 0.84fm$, $r_n^{exp} = -0.34fm$). The universal hadronic scale α_q was fixed in our calculations using the experimental value of the proton charge radius. In the non-relativistic limit of $a \ll 1$, we reproduce the standard results of the non-relativistic constituent quark model: $\kappa_p = -\kappa_n = 2$, $r_p = 1/\alpha_q = 0.82fm$, $r_n = 0$.

a)



b)

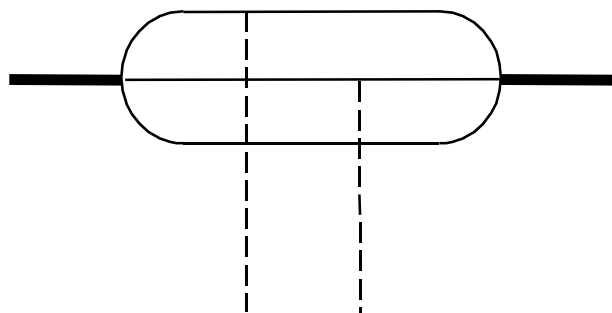


Fig.(5.1)-1

5.2 Spin structure function of proton

For an interesting case of proton spin flip with two gluons attached to the same quark, numerical calculations give

$$V_{1f} = r_5 \frac{\Delta}{m_p} \left\{ 1 - \left(B_5 + \frac{1}{2} B_N^{(0)} \right) \Delta^2 \right\} \quad (5.33)$$

with $r_5 = 0.027$ and $B_5 = -4.1 \text{ GeV}^{-2}$. The parameter r_5 was introduced in Ref. [41] and

$$r_5 \Delta \exp(-B_5 \Delta^2) / m_p$$

serves as a rough estimate of the ratio of the spin-flip and spin-conserving gluon structure functions [12]. One can see that B_5 is indeed quite large and the analytical $x_i = 1/3$ calculations at least qualitatively reflect the numerical results for the case of proton spin flip.

The longitudinal-transverse interference cross-section, accompanied by a spin-flip of the proton, is related to the sum of the conventional spin structure functions

$$g_{LT}(x, Q^2) = g_1(x, Q^2) + g_2(x, Q^2) \quad (5.34)$$

by (see review [41] for a detailed discussion of spin structure functions)

$$\sigma_{LT}^{flip} \equiv \frac{4\pi^2 \alpha_{em} 4m_p}{Q^2} x^2 g_{LT}(x, Q^2). \quad (5.35)$$

Using unitarity and following Ref. [12], we calculate the diffractive contribution to σ_{LT}^{flip} as the imaginary part of forward Compton amplitude (see Fig.(2.3)-1) for the process $\gamma_L^* p_{-\frac{1}{2}} \rightarrow \gamma_1^* p_{\frac{1}{2}}$

(note that we work with helicities of particles moving in opposite directions). The proton helicity flip results in a factor $r_5(\pm\Delta_x + i\Delta_y) \exp(-B_5\Delta^2)/m_p$ in one of the amplitudes in Fig.(2.3)-1a, which combines with the LT interference term $(\mathbf{e}^\pm \mathbf{\Delta}) \exp(-B_{f,LT}\Delta^2)/Q$. After $\mathbf{\Delta}$ integration, we get for the diffractive contribution to the spin structure function

$$g_{LT}^D(x, Q^2) = \frac{1}{x^2} \frac{r_5}{8m_p^2} \sum_f \int_x^1 \frac{d\beta}{\beta} \frac{F_{f,LT}^D(x\mathbf{P}, \beta, Q^2)}{(B_5 + B_{f,LT})^2}. \quad (5.36)$$

See also (4.6). To evaluate g_{LT}^D analytically, we consider a constant diffractive slope $B_{LT} = 10\text{GeV}^{-2}$, and for the gluon structure function at the hard scale $\overline{Q}_T^2 \sim m_f^2/(1-\beta)$, use the approximation

$$G^2(x, \overline{Q}_T^2) \sim \frac{G^2(x, \overline{Q}^2 \sim Cm_f^2)}{C(1-\beta)}, \quad (5.37)$$

where $C \sim 10$ is a constant arising from the β -integration. The squared gluon structure function rise $\propto 1/(1-\beta)$ gives a non-zero β integral for the longitudinal-transverse interference structure function and to $\log \overline{Q}^2$ accuracy the scaling expression

$$g_{LT}^D(x, Q^2) = \frac{1}{x^2} \frac{r_5}{30C(B_5 + B_{LT})^2} \sum_f \frac{e_f^2}{8m_p^2 m_f^2} \alpha_s^2(\overline{Q}^2) G^2(x, \overline{Q}^2), \quad (5.38)$$

where $\overline{Q}^2 \sim Cm_f^2$ is a moderate pQCD scale for heavy flavors. For light flavors one should rather use the semi-hard scale $\overline{Q}^2 \sim \mu_G^2$ as mentioned in Sec.3.2 and Sec.4.4.

One can see a steep rise of diffractive spin structure function

$$g_{LT}^D(x, Q^2) \propto \left(\frac{1}{x}\right)^{2(1+\delta_g)} \quad (5.39)$$

towards small x , where δ_g is a rate of small- x rise of gluon structure function $G(x, \overline{Q}^2) \propto (1/x)^{\delta_g}$ at moderately hard scale \overline{Q}^2 .

The Wandzura-Wilczek result [42],

$$g_{LT}^{WW}(x, Q^2) = \int_x^1 \frac{dy}{y} g_1(y, Q^2), \quad (5.40)$$

together with QCD ladder estimate [43] $g_1(x, Q^2) \propto (1/x)^{\delta_1}$ gives a non-diffractive contribution to the spin structure function $g_{LT}^{WW}(x, Q^2) \propto (1/x)^{\delta_1}$ with $\delta_1 \sim 0 - 0.5$. See [12] for more details. We compare both contributions in Fig.(5.2)-1 and see that our diffractive mechanism takes over at $x \lesssim 10^{-3}$ for the described above choice of parameters.

Without our diffractive contribution, the studies of $g_1(x, Q^2)$ and $g_2(x, Q^2)$ spin structure functions in two-parton ladder approximation (see [43] and references therein) showed that the corresponding A_1 and A_2 spin asymmetries vanish in the small x limit. Burkhardt and Cottingham [44] derived the sum-rule

$$\int dx g_2(x, Q^2) = 0 \quad (5.41)$$

assuming that the double-gluon ladder (Pomeron) exchange does not contribute. Indeed if there was only two-gluon exchange in the forward Compton scattering amplitude, as shown in Fig.(2.3)-1b (with vector meson replaced by virtual photon), we would have a vanishing contribution due to overall factor $\Delta^2 = 0$ (see corresponding amplitude $A_{LT} \propto \Delta$ for the vector meson production case). The unitarity-driven diffractive amplitude in Fig.(2.3)-1a gives nonvanishing contribution rapidly rising at small x which invalidates the assumption of $x^2 g_{LT}(x, Q^2)$ superconvergence behind the Burkhardt-Cottingham and Wandzura-Wilczek results.

We can not exclude even one order in magnitude inaccuracy for $g_{LT}^D(x, Q^2)$ since our result strongly depends on the pattern of scaling violations in the unpolarized gluon structure function $G(x, Q^2)$. Still, the main conclusion of this chapter is that the diffraction driven spin effects persist in the high energy, small x limit, contrary to common wisdom, and need to be studied further.

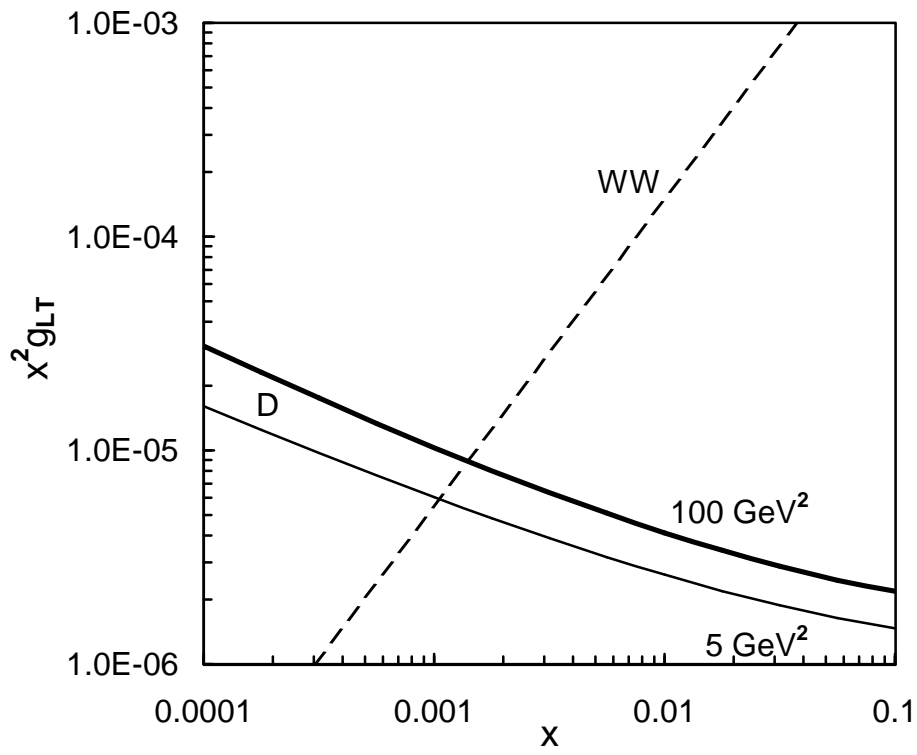


Fig.(5.2)-1

Chapter 6

Summary and outlook

We performed microscopic QCD calculations in DDIS. Light-cone perturbation theory was used to evaluate the observables in diffractive excitation of continuum for different polarization and azimuthal angle dependence. We have proved the validity of our pQCD approach and successfully used it to reproduce the existing experimental data on diffractive structure functions of the proton. We made predictions for azimuthal asymmetries and diffractive slopes which can be tested experimentally at HERA. New methods were developed to separate the leading twist transverse component from higher twist contributions and the longitudinal structure function. Duality correspondence was established for the s-channel helicity non-conserving amplitudes of vector meson production and diffractive cross-sections of low-mass continuum excitation. We derived the diffractive contribution to the spin structure

functions of the proton.

We plan to continue our efforts to better understand the diffractive processes in QCD and are currently working on the numerical calculations of the vector meson production polarization and azimuthal angle components. This will allow us to establish the duality mass range for the corresponding low-mass continuum excitation. More work will be done in the evaluation of the diffractive contribution to the spin structure functions. We will analyze the effects of the proton excitations in the intermediate states and work on improving of our understanding of the proton spin-flip process. With the improvement of existing data on total diffractive structure functions and with the new data on azimuthal asymmetries and diffractive slopes coming forth, we will test more thoroughly the gluon density in the proton.

Appendix A

Light-cone momenta and spinors

For a general four-momentum p^μ , $\mu = 0, 1, 2, 3$, we define, following [15], the light-cone components $p^\pm = p^0 \pm p^3$, so p^μ can be parameterized as

$$p = (p^+, p^-, \mathbf{p}_\perp) = \left(p^+, \frac{\mathbf{p}_\perp^2 + m^2}{p^+}, \mathbf{p}_\perp\right), \quad (\text{A.1})$$

where we used $p^2 = p^+p^- - \mathbf{p}_\perp^2 = m^2$. In general, we have four-momentum multiplication rule

$$p \cdot q = \frac{1}{2}(p^+q^- + p^-q^+) - \mathbf{p}_\perp \mathbf{q}_\perp \quad (\text{A.2})$$

(bold vector variables will represent 2-dimensional transverse components and we will skip the subscript \perp hereafter). In the light-cone quantization, or its equivalent, time-ordered perturbation theory in the infinite momentum frame with $p^+ \rightarrow \infty$, outlined in [15], only components p^+ and \mathbf{p} are conserved at each vertex, and all intermediate particles are considered

on the mass shell, as in (A.1). The integration over intermediate particle four-momentum is substituted by

$$\frac{1}{(2\pi)^4} \int d^4p \theta(p_0) \delta(p^2 - m^2) \rightarrow \frac{1}{16\pi^3} \int dp^+ \theta(p^+) \int d^2\mathbf{p}. \quad (\text{A.3})$$

Light-cone helicity spinors (see [15]) are

$$u_\lambda(p) = \frac{1}{\sqrt{p^+}} [p^+ + \gamma_0 \{m + (\boldsymbol{\gamma}\mathbf{p})\}] \chi_\lambda, \quad (\text{A.4})$$

$$v_\lambda(p) = \frac{1}{\sqrt{p^+}} [p^+ + \gamma_0 \{-m + (\boldsymbol{\gamma}\mathbf{p})\}] \chi_{-\lambda} \quad (\text{A.5})$$

for the quark and anti-quark respectively. The spinors (A.4) and (A.5) are expressed through eigenstates χ_\pm of spin projection operators $\Lambda_\pm = \gamma_0 \gamma_\pm / 2$. The standard relationships for eigenstates and projection operators are satisfied: $\Lambda_\pm \chi_\pm = \chi_\pm$ and $\Lambda_\pm^2 = \Lambda_\pm$, $\Lambda_\pm \Lambda_\mp = 0$. In the Weil representation of the γ matrices one has explicitly $\chi_+ = (1, 0, 0, 0)$ and $\chi_- = (0, 0, 0, 1)$.

Bibliography

- [1] A.H. Mueller, Deep Inelastic Scattering and QCD - DIS'98. Proceedings of 6th International Workshop, Brussels, Belgium, 4-8 April 1998, editors Gh, Corenmans and R.Roosen, World Scientific, pp. 3-19.
- [2] A. Mueller and B. Patel, *Nucl. Phys.***B415**, 373(1994); A. Mueller, *Nucl. Phys.***B425**, 471(1994).
- [3] N.N. Nikolaev and B.G. Zakharov, *Phys. Lett.* **B332**, 177 (1994); *Z. Phys.* **C53**, 331 (1992).
- [4] N.N. Nikolaev and B.G. Zakharov, *Z. Phys.* **C49**, 607 (1991).
- [5] M. Genovese, N. Nikolaev and B. Zakharov, *Phys. Lett.* **B378**, 347 (1996).
- [6] M. Genovese , N. Nikolaev and B. Zakharov, *Phys.Lett.* **B380**, 213 (1996).
- [7] A.V. Pronyaev and B.G.Zakharov (1992), unpublished; A.V. Pronyaev, Diploma Thesis, Moscow Engineering Physics Institute (1993) (in Russian).

- [8] M. Bertini, M. Genovese, N.N. Nikolaev, A.V. Pronyaev and B.G. Zakharov, *Phys. Lett.* **B422**, 238 (1998), hep-ph/9710547.
- [9] A.V. Pronyaev, , Deep Inelastic Scattering and QCD - DIS'98. Proceedings of 6th International Workshop, Brussels, Belgium, 4-8 April 1998, editors Gh, Corenmans and R.Roosen, World Scientific, pp. 358-365, hep-ph/9808432.
- [10] N.N. Nikolaev, A.V. Pronyaev and B.G. Zakharov, *JETP. Lett.* **B68**, 634 (1998), hep-ph/9809444.
- [11] N.N. Nikolaev, A.V. Pronyaev and B.G. Zakharov, *Phys. Rev.* **D59**, 091501 (1999), hep-ph/9812212.
- [12] I.P. Ivanov, N.N. Nikolaev, A.V. Pronyaev and W. Shaefer, to be published in *Phys. Lett.* **B**, hep-ph/9903228.
- [13] N.N. Nikolaev and A.V. Pronyaev, paper in preparation.
- [14] Particle Data Group, *Review of particle properties*, *Phys. Lett.* **B239** (1990).
- [15] G.P. Lepage and S.J. Brodsky, *Phys. Rev.* **D22**, 2157 (1980)
- [16] N.N. Nikolaev and B.G. Zakharov, *J. Exp. Th. Phys.* **78**, 598 (1994); *Z. Phys.* **C64**, 631 (1994).
- [17] J. Nemchik, N.N. Nikolaev and B.G. Zakharov *Phys. Lett.* **B341** 228 (1994).

- [18] W. Schäfer, Deep Inelastic Scattering and QCD - DIS'98. Proceedings of 6th International Workshop, Brussels, Belgium, 4-8 April 1998, editors Gh, Corenmans and R. Roosen, World Scientific, pp. 404-407.
- [19] I.P. Ivanov and N.N. Nikolaev, *JETP Letters* **69**, 268 (1999)
- [20] J. Nemchik, N.N. Nikolaev, E. Predazzi and B.G. Zakharov, *Z.Phys.* **C75** (1997) 71.
- [21] J. Nemchik, N.N. Nikolaev, E. Predazzi, B.G. Zakharov and V.R. Zoller, *J. Exp. Theor. Phys.* **86**, 1054 (1998).
- [22] L.N. Lipatov, *Sov. Phys. JETP* **63** (1986) 904; L.N. Lipatov, in: *Perturbative Quantum Chromodynamics*, ed. by A.H. Mueller, World Scientific (1989); E.A. Kuraev, L.N. Lipatov and S.V. Fadin, *Sov. Phys. JETP* **44** (1976) 443; *Sov. Phys. JETP* **45** (1977) 199.
- [23] E.V. Kuraev, N.N. Nikolaev and B.G. Zakharov, *JETP Lett.* **68**, 667 (1998).
- [24] H1 collab. report at 29th International Conference on High Energy Physics (ICHEP-98), 23-29 July 1998, Vancouver, Canada, <http://www-h1.desy.de/h1/www/psfiles/confpap/vancouver98/abstracts/564-marage-paper.ps>
- [25] E.D. Bloom and F.J. Gilman, *Phys. Rev. Lett.* **25**, 1140 (1970); *Phys. Rev.* **D4**, 2901 (1971).
- [26] C.E. Carlson and N.C. Mukhopadhyay, *Phys. Rev.* **D41**, 2343 (1989).

- [27] H1 Collab., P. Newman, DIS'96: Deep Inelastic Scattering and Related Phenomena, Editors G.D' Agostini and A. Nigro, World Scientific, Singapore, pp.331-339; M. Ahmed et al. **DESY-97-158** (1997)
- [28] B.Z. Kopeliovich, J. Nemchik, N.N. Nikolaev and B.G. Zakharov, *Phys. Lett.* **B324** 469 (1994).
- [29] N.N. Nikolaev and B.G. Zakharov, *Phys. Lett.* **B327**, 149 (1994); **B327**, 157 (1994).
- [30] H1 Collab., C. Adloff, S. Aid, M. Anderson, V. Andreev, B. Andrieu et al., *Phys. Lett.* **B393**, 452 (1997); E140X Collab., L.H. Tao, L. Andivahis, P. Anthony, R. Arnold et al. *Z. Phys.* **C70** 387 (1996); E143 Collab., K. Abe, T. Akagi, P.L. Anthony, R. Antonov et al., **SLAC-PUB-7927**, Aug 1998, hep-ex/9808028.
- [31] ZEUS Collab. J. Breitweg, M. Derrick, D. Krakauer et al. *Eur. Phys. J.* **C1**, 109 (1998).
- [32] H. Holtmann, N.N. Nikolaev, J. Speth, A. Szczurek and B.G. Zakharov, *Z. Phys.* **C69**, 297 (1996).
- [33] G. Alberi and G. Goggi, *Phys. Rep.* **74**, 1 (1981); T.J. Chapin , R.L. Cool, K. Goulios et al., *Phys. Rev.* **D31**, 17 (1985).
- [34] C. Conta , M. Fraternali, F. Gigli-Berzolari et al., *Nucl. Phys.* **B175**, 97 (1980).
- [35] ZEUS Collab., J. Breitweg, S. Chekanov, M. Derrick et al., DESY-98-107, hep-ex/9808020.

- [36] M. Gluck, E. Reya and A. Vogt, *Z. Phys.* **C67**, 433 (1995).
- [37] A.D. Martin, R.G. Roberts, M. Ryskin and W.J. Stirling, *Eur. Phys. J.* **C2**, 287 (1998).
- [38] H.L. Lai, J. Huston, S. Kuhlmann, F. Olness et al., *Phys. Rev.* **D55**, 1280 (1997).
- [39] V.B. Berestetskii and M.V. Terent'ev. *Yad. Fiz.* **24**, 1044, (1976) [*Sov. J. Nucl. Phys.* **24**, 547 (1976)]; I.G. Aznauryan, A.S. Bagdasaryan and N.L. Ter-Isaakyan, *Phys. Lett.* **B122**, 393 (1982)
- [40] Z. Dziembowski, *Phys. Rev.* **D37**, 778 (1988);
- [41] N.H. Buttimore et al., e-Print Archive: hep-ph/9901339.
- [42] S. Wandzura and F. Wilczek, *Phys. Lett.* **B72**, 195 (1977)
- [43] J. Bartels, B.I. Ermolaev and M.G. Ryskin, *Z. Phys.* **C70**, 273 (1996)
- [44] H. Burkhardt and W.N. Cottingham, *Ann. of Phys. (USA)* **56**, 453 (1970)

Vita

Andrey Pronyaev was born in 1970 in Obninsk, Russia. He studied at Moscow Engineering Physics Institute in 1987-1993 and graduated in 1993 with Diploma with honors in theoretical nuclear physics. In 1993-1994 he worked as junior researcher at Obninsk Institute of Physics and Power Engineering and in 1995 entered Ph.D. program at Physics Department of Virginia Polytechnic Institute and State University.

Journal publications

On the preequilibrium emission of clusters, V.P. Lunev, V.S. Masterov, A.V. Pronyaev, Yu.N. Shubin, In Proceedings of International Conference on Nuclear Data for Science and Technology, Gatlinburg, Tennessee, May 9-13, 1994, Vol. 1, p.502-504.

Pomeron in the pQCD, A.V. Pronyaev, In Proceedings of the Hampton University Graduate Studies summer school (HUGS) at the Thomas Jefferson National Accelerator Facility (TJNAF), 1996.

Twist-4 effects and Q^2 dependence of diffractive DIS, M. Bertini, M. Genovese, N.N. Nikolaev, A.V. Pronyaev and B.G. Zakharov, *Phys. Lett.* **B422**, 238 (1998).

The Forward Cone and L/T Separation in Diffractive DIS, A.V. Pronyaev, In Proceedings of 6th International Workshop on Deep Inelastic Scattering and QCD (DIS98), Brussels, Belgium, 1998, edited by Gh. Goremans and R. Roosen (World Scientific, Singapore, 1998),

pp. 358-365.

Azimuthal asymmetry as a new handle on σ_L/σ_T in diffractive DIS, N.N. Nikolaev, A.V. Pronyaev and B.G. Zakharov, *JETP. Lett.* **B68**, 634 (1998).

Duality correspondence between diffraction into vector mesons and continuum, N.N. Nikolaev, A.V. Pronyaev and B.G. Zakharov, *Phys. Rev.* **D59**, 091501 (1999).

Diffraction driven steep rise of spin structure function $g_{LT} = g_1 + g_2$ at small x and DIS sum rules, I.P. Ivanov, N.N. Nikolaev, A.V. Pronyaev and W. Shaefer, to be published in *Phys. Lett.* **B**.